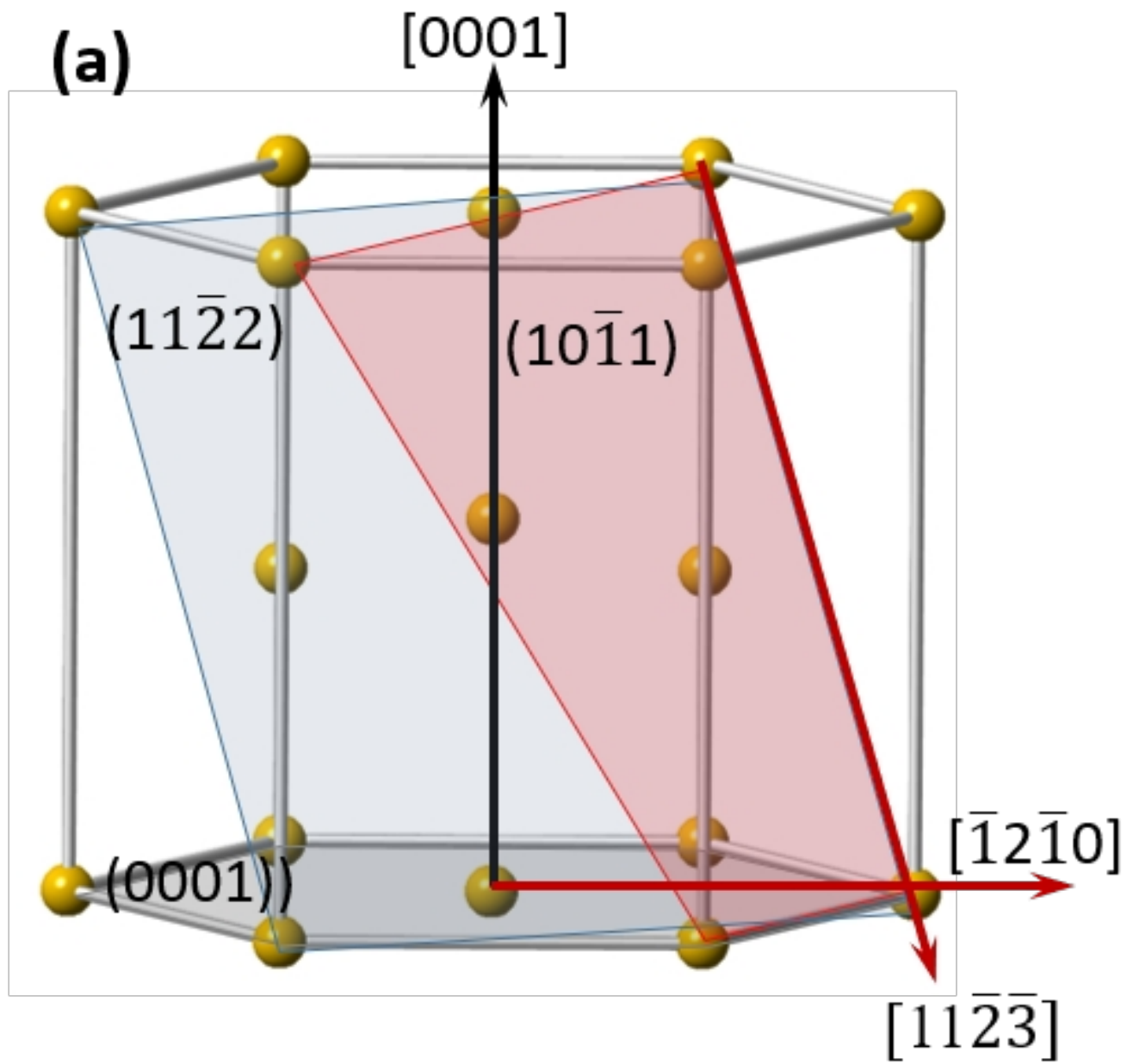
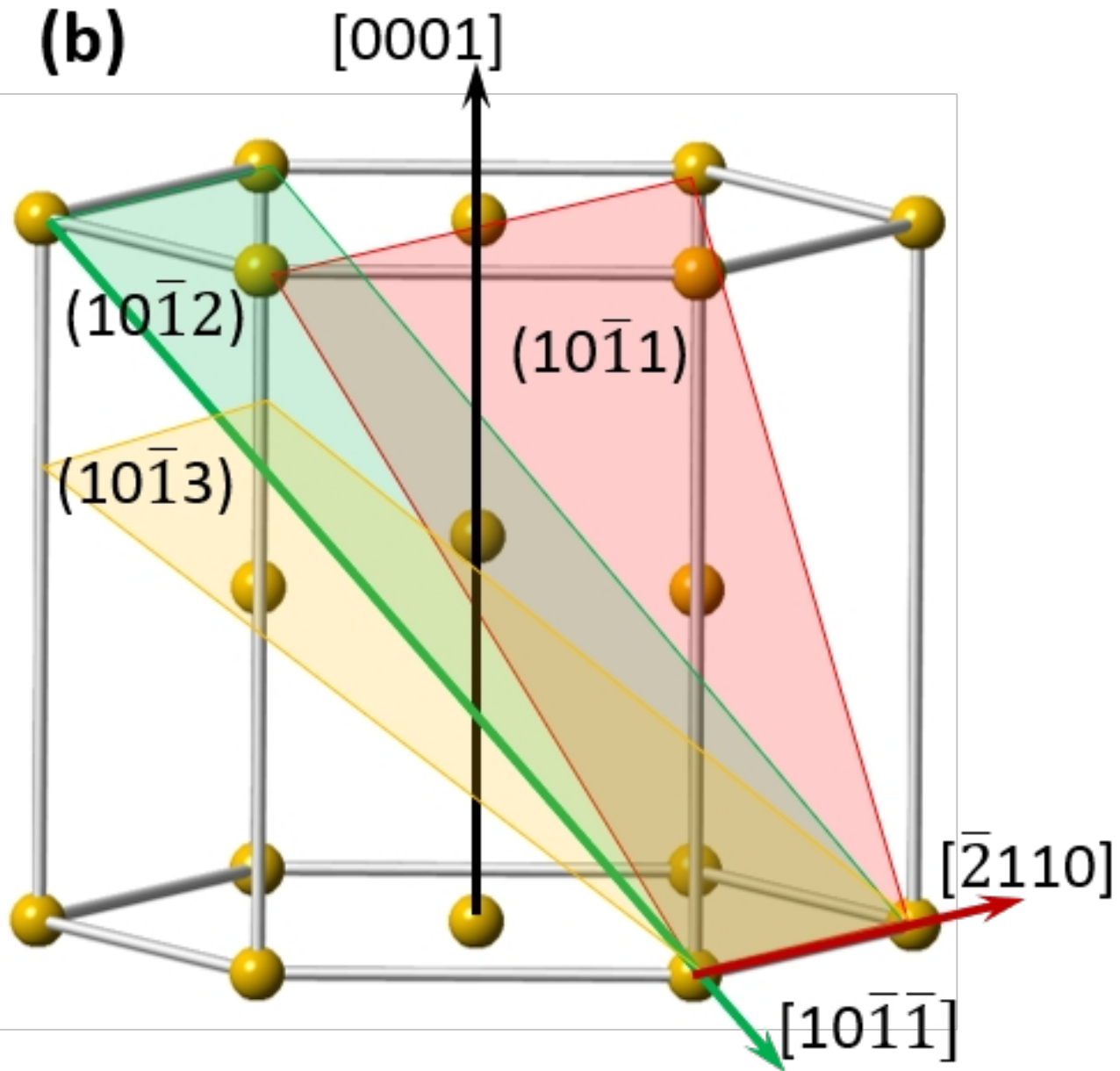


(a)



**(b)**



# Crystallographic and experimental disproof of pyramidal $\langle c+a \rangle$ slip in magnesium

Yan Huang<sup>1\*</sup>, Xinliang Yang<sup>2</sup>, Jun Jiang<sup>3</sup>

<sup>1</sup>BCAST, Brunel University London, Kingston Lane, Uxbridge UB8 3PH, UK.

<sup>2</sup>WMG, University of Warwick, Coventry CV4 7AL, UK.

<sup>3</sup> Department of Mechanical Engineering, Imperial College London, Exhibition Road, SW7 2AZ, UK.

\*Corresponding author email: yan.huang@brunel.ac.uk

## Abstract

The activation of non-basal pyramidal  $\langle c+a \rangle$  slip has been perceived as key to enhance the ductility of magnesium and its alloys. However, there has never been convincing evidence to show the physical existence of  $\langle c+a \rangle$  dislocations and their involvement in deformation has been a core issue in magnesium research. In the present work, the impossibility of  $\langle c+a \rangle$  slip is analyzed based on fundamental concepts of dislocation and atomic interactions. The atomic configurations and crystallographic features in association with  $\langle c+a \rangle$  dislocations are unambiguously revealed for the first time, demonstrating that any possible  $\langle c+a \rangle$  dislocation core structures would involve too many atoms on multiple lattice planes and are physically impossible. Experiments of magnesium single crystal compression along its c-axis were conducted at temperatures from 20°C to 500°C and the results showed no evidence of the involvement of  $\langle c+a \rangle$  dislocations in any form as a mechanism of deformation during either plastic flow or fracture. von Mises criterion for compatible deformation, which drives the pursuit of pyramidal  $\langle c+a \rangle$  slip, is critically discussed.

## Key words

Magnesium, pyramidal  $\langle c+a \rangle$  slip, dislocation structure, compression test.

### 1. Introduction

The commercial use of Mg alloys as lightweight structural material has been much below expectations. One of the limiting factors is the poor formability at room temperature. This is explained by the lack of sufficient amount of easy slip systems and strong anisotropy of deformation [1, 2]. At room temperature, only basal slip  $\langle 11\bar{2}0 \rangle \{0001\}$  operates with 2 independent slip systems, which are considered incapable of accommodating arbitrary strains. Prismatic  $\langle 11\bar{2}0 \rangle \{1\bar{1}00\}$  and pyramidal  $\langle 11\bar{2}0 \rangle \{1\bar{1}01\}$  slips do not contribute to plastic deformation along the c-axis  $\langle 0001 \rangle$ . The additional mechanisms which can supply the missing degree of freedom are pyramidal slips with a non-basal Burgers vector  $1/3\langle 11\bar{2}3 \rangle$  (or  $\langle c+a \rangle$ ). Pyramidal  $\langle c+a \rangle$  dislocations require a substantially higher critical resolved shear stress to operate than for a basal dislocation at room temperature and are believed to take place more easily at high temperatures, where the gap in critical resolved shear stress requirement diminishes (there is no theoretical justification and convincing experimental evidence though), resulting in good ductility and formability [1, 3]. Mg exhibits a strong propensity for mechanical twinning, in addition to dislocation slip, especially  $\{10\text{-}12\}$  tension twin [4, 5]. However, twinning involves only simple shear in one direction with limited accommodation capability as a polar deformation mechanism. It is therefore generally accepted that only pyramidal  $\langle c+a \rangle$  slip can accommodate deformation along the c-axis, completing the requirement for five independent slip modes for homogeneous, generalized ductility of a polycrystalline aggregate and their activation at low temperatures is key to



achieve high ductility [1, 6]. The pursuit of pyramidal  $\langle c+a \rangle$  slip has been a strategic approach in the development of new Mg alloys and one of the hottest topics in Mg research.

Initial studies of non-basal slip can be tracked back to late 1950s to early 1970s [7-11] but extensive research has been conducted in the last 10 years [6, 12-21]. Attempts to observe  $\langle c+a \rangle$  dislocation activities have been done during constraint deformation of Mg single crystals using either bulk samples or micropillar [6, 7-17] and computer simulation [2, 18-21]. Unfortunately, there has been no convincing evidence in the literature to prove  $\langle c+a \rangle$  slip. Simple, clear and unambiguous distributed slip traces due to  $\langle c+a \rangle$  slip have never been observed on the surface of either bulk single crystals or micro-pillars. The  $\langle c+a \rangle$  slip lines reported by Obara et al [11] exhibit curvy and rough features with randomly varied line width. They are simply artificial scratches existed prior to the deformation as all the diagonal “ $\langle c+a \rangle$  slip lines” have been cut through by the straight basal slip lines (see Fig. 3 in [11]).  $\langle c+a \rangle$  slip lines are also claimed in [17] but again they are artificial scratches as these lines are random in shape and direction, yet cutting through by straight horizontal lines, which could be basal slip lines. The authors [17] claimed that  $\langle c+a \rangle$  slip traces are faint and difficult to observe and reveal, which is unfounded as  $\langle c+a \rangle$  Burgers vector is significantly larger than  $\langle a \rangle$  Burgers vector and the slip lines of  $\langle c+a \rangle$  dislocations should be more striking and easily observed than basal dislocations. The  $\langle c+a \rangle$  slip traces presented in ref [12] and [13] are actually fractures. Evidence of  $\langle c+a \rangle$  slips was claimed from micropillar experiments but the prevalent slip planes were not identified in these studies and the flow patterns showed that only basal slips occurred [15, 16]. Most reported  $\langle c+a \rangle$  activities have been based on TEM examinations [6, 10, 11, 14, 22]. All TEM images of  $\langle c+a \rangle$  dislocations have been taken under beam conditions along a direction in the basal plane such as  $\mathbf{g} = (0002)$ ,  $(11\bar{2}0)$  and  $(01\bar{1}0)$  [6, 10, 11]. These beam conditions cannot confirm the presence of

a  $\langle c+a \rangle$  dislocation because under these beam conditions, dislocation images could simply come from screw  $\langle a \rangle$  dislocations, of which the lattice distortion is not limited to the basal plane. Till now, no evidence has been presented to confirm the  $\langle c+a \rangle$  dislocation Burgers vector under the invisible beam condition, which is the only uncompromised condition for giving unambiguous TEM evidence. All computer simulations have failed to construct an initial atomic configuration to represent the core structure of a non-basal dislocation. The best effort was to construct two  $\langle c+a \rangle$  partial dislocations on the plane of slip, of which the dislocation line is normal [2]. However, this work did not define the extra half atomic plane and dislocation line direction and the associated crystallographic features and atomic configurations were incorrect. Some studies applied an extremely high load to a perfect Mg single crystal [18], effectively simulating the generation of  $\langle c+a \rangle$  dislocations while others introduce an artificial defect [23]. The core structure of a  $\langle c+a \rangle$  dislocation has never been defined and observed, neither extended dislocation nodes, partial dislocations and resultant stacking faults.

In fact, early studies on the plastic properties of Mg single crystals have shown that Mg crystals deform essentially by the glide of basal dislocations with the Burgers vector  $\langle a \rangle = 1/3\langle 11\bar{2}0 \rangle$  within  $\{0001\}$  basal plane, and by twinning and prismatic slip under certain loading conditions over a wide range of temperatures [7-9, 24]. Recent investigations on the deformation mechanisms of Mg single crystals under plane strain compression [25] and indentation [26] confirmed the above findings. However, these studies failed to make an explicit conclusion that non-basal  $\langle c+a \rangle$  slips do not exist, due to limited experimental conditions and lack of in-depth crystallographic analysis.

The clarification and rectification of the current misleading theory and practice for the deformation mechanisms of Mg and its alloys would have the greatest relevance to the research, development and engineering applications. In the present work, the physical and crystallographic nature of pyramidal  $\langle c+a \rangle$  dislocations is analyzed and their possible core structures are revealed for the first time, which, together with the results of constraint c-axis compression tests of Mg single crystals, provides both crystallographic and experimental evidence that pyramidal  $\langle c+a \rangle$  slips are not possible in magnesium.

## 2. Impossibility of $\langle c+a \rangle$ dislocations

Fig. 1 shows the commonly recognized slip systems (Fig. 1a), basic twinning systems (Fig. 1b) and the atomic environment in association with the  $\langle c+a \rangle$  slip (Fig. 1c) in the hexagonal close packed (hcp) Mg crystal. A fundamental problem with non-basal  $\langle c+a \rangle$  dislocations is that both the slip direction  $\langle 11\bar{2}3 \rangle$  and slip plane, either  $\{11\bar{2}2\}$  or  $\{10\bar{1}1\}$  are not close packed and the atoms in the slip direction and on the slip planes, are not the nearest neighbors. Burgers vector  $\langle c+a \rangle$  has a value of  $b_{\langle c+a \rangle} = 1.907a$ , nearly two times of the basal lattice constant  $a$ , which is the value of the basal dislocation Burgers vector  $\langle a \rangle$ . Such dislocations, if exist, carry a line energy nearly four times of that for a basal dislocation, since the unit length dislocation line energy is proportional to the square of its Burgers vector. Mg atom has a diameter of 0.321nm, equal to the lattice constant  $a$ , the distance of two nearest neighbor atoms and a von der Waals diameter of 0.346nm [27]. The distance between two neighbor atoms along a  $\langle c+a \rangle \langle 11\bar{2}3 \rangle$  direction is 0.612nm (1.9 times of the distance of the nearest atoms) and they are substantially outside of each other's van der Waal diameter. They do not share electrons and any interactions between them would be non-covalent, involving dispersed variations of electromagnetic force, which scale with their distance  $R$  as  $1/R^6$  [28].

This suggests that the interaction potential between neighbor atoms along the  $\langle c+a \rangle$  direction is only about one forty ninth ( $1.9^6=49$ ) of the potential between an atom and one of its 12 coordination atoms. It is unlikely that atoms along the  $\langle c+a \rangle$  direction can act as a physical entity in response to either mechanical or energetic impact. Physically, lattice translation via  $\langle c+a \rangle$  slip means that an atom has to break up the bonds with its 12 nearest coordination atoms before attaining the next lattice position, which may occur for an individual atom by thermally activated diffusion but is impossible in a collective action such as dislocation slip during deformation as the energy required is too high. The latent heat of fusion, which represents the energy required for melting, is 8.48kJ/mol for Mg [29], which is close to its gaseous diatomic bond energy of 8.55 kJ/mol [30]. The bond energy of an Mg atom with its 12 coordination atoms in the solid state, although unknown due to the delocalization nature of the metallic bond, should be significantly higher than that for a pair of Mg atoms in the gaseous state. Therefore, it is estimated that the energy required to break an Mg atom from its 12 coordination atoms is higher than the energy required for melting. On the other hand, the spacing between pyramidal slip planes is either too small, 0.137nm for  $\{11\bar{2}2\}$  plane, which is less than half of the atomic diameter (0.321nm) or contains double layers of atoms for  $\{10\bar{1}1\}$  planes (with a motif plane). This means, from a viewpoint of hard sphere atomic model, that atoms would block each other physically if there is any relative movement on these planes. It is arguable from quantum mechanics that quantum tunneling may allow a rendered path for atomic transition to occur and overcome space limit [31]. The quantum effect, however, has been reported to be dominant only when the deformation temperature is close to absolute zero and has limited impact on deformation behavior at ambient temperature and above [32]. Even if the relative movement of atoms is possible via quantum tunneling between these narrowly spaced lattice planes, it represents a difficult and high energy path as it is unavoidable for regions of high electron densities to overlap and interfere where they

encounter. Stacking fault energies are more direct measurements of energies associated with the formation and decomposition of dislocations. Crystal chemistry suggests that stacking faults are related to bond features, and atoms of non-direct interactions are not influential to stacking sequence [33]. Stacking faults as planar defects are essentially observed in close-packed fcc and hcp crystals and associated with the close-packed planes; in the non-closed packed bcc metals, no stacking faults are expected and dislocations are barely extended because of the absence of low energy stacking faults [34]. This is believed the major reason why dislocations, in particular screw dislocations, in bcc metals are much less mobile than those in fcc metals [35]. In the hcp structure, both the intrinsic ( $I_1$ ,  $I_2$ ) and extrinsic (E) stacking faults are defined by the disordering features of the close-packed basal planes [34]. There have been interests in stacking faults on non-close packed pyramidal planes in Mg, particularly as  $\langle c+a \rangle$  dislocations are concerned. Recently, B. Yin, Z. Wu and W. A. Curtin [36] carried out a comprehensive study based on density functional theory guided by crystal symmetry analysis, to calculate all stacking faults in typical hcp metals including Mg. In their first principles calculations, the relevant stable stacking fault energy, position, and structure on the basal ( $\{0001\}$ ), prism I  $\{10\bar{1}0\}$  and II ( $\{11\bar{2}0\}$ ) and pyramidal I ( $\{10\bar{1}1\}$ ) and II ( $\{11\bar{2}2\}$ ) planes were determined using all-periodic supercells with full atomic relaxation. Their calculations show that the stacking faults for pyramidal I and II planes are in the range of 161-203 mJ/m<sup>2</sup> (depending on the type of stacking faults), substantially higher than the range of 18-54 mJ/m<sup>2</sup> for the basal plane, which are generally in agreement with the calculations from other work [37, 38]. They found that stacking fault position and structure were dictated by crystal symmetry, whereas the associated stacking fault energies are governed by the atomic bonding. The stacking faults on all the slip planes except the basal plane show substantial out-of-plane displacements while stacking faults on the Prism II, Pyramidal I and II planes show additional in-plane displacements, all extending to multiple atom layers. Based on the

stacking fault analysis, they suggested that pyramidal zonal dislocations are unlikely. Atoms in a crystal can be treated as a collection of atoms on a particular set of lattice plane, for example,  $\{0001\}$  or  $\{11\bar{2}2\}$  or any other lattice plane. But atoms themselves do not know lattice planes and, in response to an applied external force, they simply follow a pathway that minimizes the free energy of the system. Although based on virtual simulations, the findings of high stacking fault energies in association with pyramidal planes are critically important to understand the impossibility of  $\langle c+a \rangle$  slip in terms of energy requirements. Taking into account of the crystallography, atomic bonding and interaction potential and stacking fault energies discussed above, it should not be too difficult to see that the pathway of atomic movement during  $\langle c+a \rangle$  slip is against the symmetry principle that atoms arrange towards the highest possible symmetry to obtain equal environment with a minimized free energy [33].

### 3. Possible core structures of $\langle c+a \rangle$ dislocations

To obtain an ultimate understanding of  $\langle c+a \rangle$  dislocations and show their inapplicability as a deformation mechanism, it is necessary to reveal their possible core structures, which, to the best of our knowledge, has unfortunately never been done. A dislocation is defined by its Burgers vector and the slip plane and so is its core structure, including the direction of dislocation line and the extra half atomic plane above the dislocation line in the case of an edge dislocation. The atomic configurations in association with  $\langle 11\bar{2}3 \rangle \{11\bar{2}2\}$  and  $\langle 11\bar{2}3 \rangle \{10\bar{1}1\}$  dislocations are reconstructed with the help of commercial crystal structure visualization software CrystalMaker© and free software VESTA. The illustrations in Fig. 2 and 3 are produced with CrystalMaker©.

Fig. 2 shows the reconstruction of an edge  $\langle 11\bar{2}3 \rangle \{11\bar{2}2\}$  dislocation using an Mg supercell presented by both “Ball & Stick” (Fig. 2a,) and “Full Space” (Fig. 2b-h) models, based on the standard CIF crystal structure and lattice constants, i.e.,  $a = 3.203\text{\AA}$ ,  $c = 5.127\text{\AA}$ . The Mg supercell has a span of 32 unit cells in x ( $a_1$ ) and y ( $a_2$ ) directions and 16 unit cells in z ( $c$ ) direction, containing 32768 lattice sites. Fig. 2a shows the atomic arrangement on the cross-section of the dislocation by the “Ball & Stick” model, viewing along the dislocation line direction  $[1\bar{1}00]$  and with the slip plane  $(11\bar{2}2)$  being horizontal and the Burgers vector direction  $[11\bar{2}3]$  horizontal in the paper plane. A plane parallel to the paper plane, i.e.,  $(\bar{1}100)$ , is defined as the plane of slip and the atoms on the front plane of slip (the paper plane) are highlighted in green. Taking  $(11\bar{2}2)$  plane AC as a slip plane in consideration,  $\overline{AC} = 1/3[11\bar{2}3]$  is then the Burgers vector. The vertical red lines depict atomic planes perpendicular to both the Burgers vector and slip plane, and are determined to be  $(33\bar{6}1\bar{6})$ .  $(33\bar{6}1\bar{6})$  planes have an interplanar spacing of only 0.0278 nm and Burgers vector  $\langle c+a \rangle = 1/3[11\bar{2}3]$  has a length of 0.612 nm (Note: all characteristic lattice planes are determined with the help of CrystalMaker and VESTA software. Inter-planar spacing and angles between characteristic lattice planes are calculated using the standard equations for hcp crystals [39]). Therefore, there are totally 23  $(33\bar{6}1\bar{6})$  planes over the  $\langle c+a \rangle$  Burgers vector  $\overline{AC}$ , although only 8 are shown for clarity. Fig. 2a includes all crystallographic elements required to describe the possible core structures for an edge  $\langle 11\bar{2}3 \rangle \{11\bar{2}2\}$  dislocation and such an atomic configuration is reconstructed for the first time. However, Fig. 2a does not provide clear spatial visibility of 3D atomic arrangements as all atoms are projected on the paper plane. In Fig. 2b-h, the Mg supercell in the “Full Space” model is used to replicate the crystal structure based on the “hard sphere” atomic model. In order to display possible core structures for an edge  $\langle 11\bar{2}3 \rangle \{11\bar{2}2\}$ , the Mg supercell is cut into a rectangular parallelepiped, with  $(11\bar{2}2)$ ,  $(\bar{1}100)$  and  $(33\bar{6}1\bar{6})$  being parallel to horizontal, front (the paper plane) and side surfaces respectively as shown in Fig.

2b and c (Note: the cutting is performed by “select” and “delete” functions with the CrystalMaker software; unit cell transformation to form an orthorhombic unit cell was not possible with the selected planes and directions). This re-surfaced supercell contains 3831 lattice sites with 42 (11-22) planes, 22 (-1100) planes and 186 ( $\overline{33616}$ ) planes. Fig. 2b shows a possible structure of an edge  $\langle 11\bar{2}3 \rangle \{11\bar{2}2\}$  dislocation, formed by removing atoms from a single ( $\overline{33616}$ ) plane AB from atom A and downwards. The extra half atomic plane is the plane BA' above the dislocation core A on the slip plane AC. Fig. 2c shows the dislocation line along the  $[1\bar{1}00]$  direction, in which the white balls represent vacant lattice sites where atoms are removed. The core structure of this dislocation will be discussed later together with other possible dislocation structures. It needs to be pointed out, however, that lattice plane  $\{\overline{33616}\}$  has a stacking sequence of ...ABC.....TUVAB... along the Burgers vector direction  $\langle 11\bar{2}3 \rangle$  and the removal of a single  $\{\overline{33616}\}$  plane would have effectively left a stacking fault in the crystal below the dislocation line. This is against the nature of a dislocation as a line defect and hence the formation of an edge  $\langle 11\bar{2}3 \rangle \{11\bar{2}2\}$  dislocation by removing a single  $\{\overline{33616}\}$  plane is invalid. In order to maintain the stacking sequence, 22  $\{\overline{33616}\}$  planes have to be removed to form an edge  $\langle 11\bar{2}3 \rangle \{11\bar{2}2\}$  dislocation. Fig. 2d shows the rectangular parallelepiped Mg supercell after removing 22  $\{\overline{33616}\}$  planes from the slip plane AC and below (by performing the “select” and “delete” functions), leaving 22  $\{\overline{33616}\}$  extra half atomic planes above the slip plane AC and an empty space below. A full atomic relaxation or simply in-plane relaxation of the supercell with a sizeable empty space as shown in Fig. 2d can be difficult and the resultant atomic configurations will be largely dependent on the approaches adopted, which are not the concern of the present work. The present work aims to establish possible core structures of  $\langle c+a \rangle$  dislocations with the least crystallographic distortions and therefore possible minimum energies. The justification of their inapplicability as a mechanism for plastic deformation will then lead to convincing



disproof of the  $\langle c+a \rangle$  slip. Therefore, two rigid fixation operations are performed to form two more dislocation structures, in addition to the one shown in Fig. 2b and c. Fig. 2e and f show a dislocation core structure, formed after the empty space below the slip plane AC is completely filled by moving all atoms on both sides horizontally and equally towards the center of the empty space until a complete match is obtained (using the “move selection” function). The dislocation core structure obtained is comprised of two parallel lines of vacancies on the slip plane AC. One line of vacancies is along the  $[1\bar{1}00]$  direction from site A, which is identical to the single dislocation line in Fig. 2c and the other can be either along line-S1 (as shown) or line-S2. The  $(3\bar{3}\bar{6}\bar{1}\bar{6})$  plane in coincidence with line-S1 is the starting plane of the stacking sequence (an arbitrary selection to position the plane AA' in the middle so that it is consistent with the definition of Burgers vector  $\overline{AC}$  in the illustrations) and the  $\{3\bar{3}\bar{6}\bar{1}\bar{6}\}$  plane on line-S2 is the start of another round of stacking sequence. Fig. 2g and h show a possible dislocation core structure obtained under the same operation as for Fig. 2 e and f but leaving the vacancies on the  $(11\bar{2}2)$  plane immediately below the slip plane AC unfilled. The dislocation core now has four lines of vacancies on two lattice planes. Further fixations are not performed as they would generate dislocations with a core structure of more vacancies, being effectively a three-dimensional defect.

Fig. 3a shows the atomic configuration, using the “Ball & Stick” model, on the cross-section of an edge  $\langle 11\bar{2}3 \rangle \{10\bar{1}1\}$  dislocation, which has been claimed to be as important as the  $\langle 11\bar{2}3 \rangle \{11\bar{2}2\}$  slip system. In the figure, slip plane  $(10\bar{1}1)$  is horizontally arranged and Burgers vector  $AC = 1/3[11\bar{2}\bar{3}]$  is horizontal in the paper plane. The interplanar spacing of slip plane  $\{10\bar{1}1\}$  is 0.245nm, which is close to that for basal plane. However, each  $(10\bar{1}1)$  plane consists of two atomic layers, i.e., the lattice plane plus a motif plane, which is a crystallographic translation equivalent to the lattice plane. The atomic plane perpendicular to

both the slip plane  $(10\bar{1}1)$  and Burgers vector is  $(3\bar{3}6\bar{1}6)$ , which is the same as for an edge  $\langle 11\bar{2}3 \rangle \{11\bar{2}2\}$  dislocation because they have the same Burgers vector. Similar to the  $\langle 11\bar{2}3 \rangle \{11\bar{2}2\}$  slip system, there are 23  $(3\bar{3}6\bar{1}6)$  planes over the length of the  $\langle c+a \rangle$  Burgers vector. The plane of slip has a high Miller index of  $\{2\bar{5}41\bar{1}616\}$ , with an interplanar spacing of only 0.0076 nm, which makes this slip system far more complicated. Fig. 3b-d show related crystallographic configurations using the “Full Space” model but the atomic diameter is halved to avoid severe overlapping. Fig. 3b shows that there are 23 inter-planar spacings of  $(10\bar{1}1)$  plane between the slip plane AC and its identical repeat, A’C’ plane, with a total of 48 atomic planes from atomic plane AC to A’C’, including 24  $(10\bar{1}1)$  lattice planes and 24 motif planes. Atom A’ is the nearest neighbor of atom A in the lattice plane  $(3\bar{3}6\bar{1}6)$  AA’ above the slip plane AC. It is profoundly important to have this information because it tells that atoms on a  $(3\bar{3}6\bar{1}6)$  plane are too far apart and cannot act collectively and coordinatively. In the field of view in Fig. 3b, all atoms in the front plane of slip (the paper plane) are either on the AC plane or A’C’ and are highlighted in green and red, and the rest are not on the paper plane. This is shown more clearly in Fig. 3c, which is viewed along the Burgers vector direction  $\langle 11\bar{2}3 \rangle$ , displaying the atomic configuration on  $(3\bar{3}6\bar{1}6)$  planes. Atoms on the paper plane in Fig. 3c are all highlighted in red. It can be seen that, along the potential dislocation line direction  $\langle 25\bar{4}1\bar{1}616 \rangle$ , the nearest neighbor atom of the atom A is not included in the field of view, suggesting that the atomic density along  $\langle 25\bar{4}1\bar{1}616 \rangle$  direction line is extremely low. It is not difficult to realize that it is impossible to have a dislocation line along such a lattice direction. Fig. 3d is a view of the slip plane  $(10\bar{1}1)$ , in which the front plane of slip  $(25\bar{4}1\bar{1}616)$  (the paper plane in Fig. 3b) is shown with all atoms highlighted in green. Its next identical plane is too far apart and cannot be included in the field of view. It can be seen from Fig. 3c and d that the potential dislocation line, extra half atomic plane and the plane of slip for an edge  $\langle 11\bar{2}3 \rangle \{10\bar{1}1\}$  dislocation all have high

indices and are irrational. Due to the involvement of irrational planes and directions, to construct possible core structures for an edge  $\langle 11\bar{2}3 \rangle \{10\bar{1}1\}$  dislocation requires an amount of atoms that is too big and beyond the capacity of the software in use and therefore is not performed.

#### 4. Compression of Mg single crystals

##### 4.1. Experimental details

##### 4.1.1. Material and sample preparation

A piece of cylindrical shaped high purity magnesium (99.99%) single crystal with (0001) orientation along its axis was produced by the Bridgman method and supplied by MaTeck Material Technologie & Kristalle GmbH, Germany. Cylindrical samples were used because all dislocation slip planes and twinning planes would intersect with the cylindrical surface at a fixed angle everywhere, which helps identify the origin of surface traces. The as-received single crystal was 5 mm in diameter and 55mm in length. The single crystal was then cut into 8 pieces, each of 6mm in length for compression test, with an extra piece for characterization. The cutting was performed on a Struers Accutom-10 machine at a very low feeding speed of 0.01mm/s and rotation speed of 2000rpm so that bending was minimized. The cylindrical surface was polished with a P2400 abrasive grinding paper and the (0001) orientation error was within  $2^\circ$  (manufacturing error). The end surface perpendicularity error relative to the cylindrical axis for all samples was measured to be within  $\pm 0.2^\circ$ . The samples were heat treated at  $300^\circ\text{C}$  for 30 min, buried in graphite powder to avoid oxidation, in order to release possible residual stresses due to solidification during single crystal growth. EBSD was carried to confirm the orientation information provided by the supplier.

#### 4.1.2. c-axis compression

The single crystal samples were compressed along their axial  $\langle 0001 \rangle$  direction at room temperature (20°C), 200°C, 300°C, 400°C and 500°C, respectively and at a constant strain rate of 0.001/s, to a strain at which failure occurred or visible cracks appeared. The testing temperature from 20°C to 500°C was selected as it represents essentially the full range of deformation temperature for magnesium in both research and industrial practice. One sample tested at 20°C and 200°C and two at 300°C, 400°C and 500°C. The uniaxial compression test was carried out at Imperial College London on a Gleeble 3800 test machine, which is a fully integrated digital closed loop thermal and mechanical testing system. A 0.25mm graphite disk, cutting from GRAFOIL© Flexible 0.25mm graphite roll sheet, was inserted between the sample and the grip block on either side and used as a lubricant. A Gasoil© Thred Gard graphite containing nickel-based compound was applied to both sides of the graphite disks to provide a protection against seizing, welding and corrosion. The sample was pre-held at a load of 0.2KN (~10MPa) to achieve a good contact between the compression platen and the crystal, and then heated at a rate of 1°C/s and held for 2 minutes at the testing temperature before deformation. The temperature was maintained constant with an error of less than 0.5°C during deformation. After deformation the samples were cooled in air and then removed from the machine. Compression load/stress was recorded as a function of time and stroke (compression displacement). The engineering strain stress curves were obtained from the recorded stroke-load data. The engineering strain was given as the ratio of compression displacement (stroke) over the exact initial height of individual single crystal samples. The engineering stress was given as the compression force divided by the initial cross-section area, which was assumed to be the same for all samples. Since the total strain associated with all samples was less than 8%, these approximations should have limited effect on data accuracy.

#### 4.1.3. Characterization of the deformed samples

Photographs were taken from the as-deformed Mg single crystal samples to show their general appearance and surface features. The as-deformed samples were then sectioned through their longitudinal plane, which was selected to be approximately perpendicular to the major fracture surface of a particular sample, or cross-section for microstructural characterization. The samples were sectioned under the same conditions as those for initial single crystal cutting. A sectioned surface was firstly ground using silicon carbide grinding papers, 2400 and P4000 respectively and then polished with silicon oxide suspensions, followed by ultra-sonic vibration for 5 min immediately after polishing. For EBSD analysis the polished surfaces were further processed by broadband ion milling, using a Hitachi IM4000Plus Ion milling system, in order to remove surface scratches and strain layer that could be generated during grinding and polishing. Optical microscopy was conducted on a Carl Zeiss AxioScope A1 optical microscope. Secondary electron imaging was performed on a Carl Zeiss Supra 35 field emission gun scanning electron microscope (FEGSEM) and electron backscatter diffraction (EBSD) was carried out on either the Carl Zeiss Supra 35 FEGSEM equipped with an EDAX EBSD system or a JEOL JSM7800F FEGSEM equipped with an Oxford Instruments Symmetry® EBSD detector. All EBSD data presented in the paper are original data without any cleaning and processing, and analyzed with EDAX OIM software.

## 4.2. Results

### 4.2.1. Mechanical response

Fig. 4 shows typical engineering strain-stress curves obtained from the c-axis compression, as a function of deformation temperature from 20°C to 500°C. It can be seen from the figure

that stress increases with strain and reaches a maximum at all temperatures. Both the ultimate strength and the corresponding strain decreased rapidly with increasing temperature, from 355 MPa and about 8% at 20°C to 18 MPa and 0.6% at 500°C, respectively. Failure occurred at the ultimate strength at 20°C, whereas at elevated temperatures all crystals continued to deform as the maximum load passed, straining under failing stress. In Fig. 4b, the measured ultimate strength is plotted against temperature in comparison to data obtained under similar conditions in literature, showing that the mechanical performance in the present experiment is in a good agreement with previous work.

#### 4.2.2. Deformation mechanisms

The stress to strain ratio over the near linear portion of stress-strain curves (Fig. 4), prior to the ultimate strength, was ~3.9 GPa at 20°C and gradually down to 2.8 GPa at 500°C. These values are substantially lower than the elastic modulus for Mg (44 GPa), suggesting that the deformation was plastic, although there was no apparent yielding which is typical of Mg deformation [8, 12, 24]. Apparent bulk deformation was not observed and samples exhibited a straight cylindrical surface in the middle or a concave shape after compression (Fig. 5), instead of bulging, which normally takes place due to friction effect. As shown in Fig. 5, material flow essentially occurred in the end regions and parallel to sample end surfaces. Only basal slip can be inferred from these features as any  $\langle c+a \rangle$  slips would have produced bulk deformation and slip traces aligned at an angle of ~58° for  $\langle 11\bar{2}3 \rangle \{10\bar{1}1\}$  slip and ~62° for  $\langle 11\bar{2}3 \rangle \{11\bar{2}2\}$  slip to the sample end surfaces. Horizontal basal slip traces, the intersections of basal planes with sample cylindrical surface, were observed on the sample deformed at 20°C (Fig. 5a). It has been shown that basal slip on  $\{0001\}$  can be caused by misalignment of as little as 0.15° [24, 40], owing to the low critical resolved shear stress of ~0.5 MPa at room temperature [1]. The misalignment of ~2° in the present work would give

a Schmid factor  $m$  of  $\sim 0.035$  for basal slip. Hence the resolved shear stress should be higher than 0.5 MPa when the applied stress was 15 MPa or above, which was reached at all temperatures. This deformation largely concentrated in the end regions and was probably due to friction induced changes in stress state favorable for basal slip, causing apparent material side flow near the end surfaces (Fig. 5). At elevated temperatures, total strains were limited and slip traces were not detectable.

Two types of double twinning were observed (Fig. 6) and considered to have contributed to deformation. One was  $\{10\bar{1}1\}$ - $\{10\bar{1}2\}$  double twin (DT1) and the other  $\{10\bar{1}3\}$ - $\{10\bar{1}2\}$  (DT2). These are typical contraction twins in Mg single crystal in c-axis compression [8, 25]. DT1 bands were mainly found in the end regions and mostly consumed by recrystallized grains, which has been observed in previous studies [24, 40]. DT1 bands are highlighted in green color in the EBSD maps in Fig. 6a and c, along with bands of the recrystallized grain, and their poles are shown in the same color in the corresponding pole figures in Fig. 6b and d. The black spots in the pole figures represent the poles of the recrystallized grains. It can be seen that recrystallized grains at 20°C exhibit substantially a single orientation, indicating that the recrystallization happened after deformation, while at 300°C and 500°C the orientation spread in the recrystallized grains suggests a dynamic recrystallization. At 20°C, a large amount of DT2 bands were observed in the bulk of the crystal. Shear occurred within the DT2 bands and resulted in static recrystallization during storage (Fig. 6a). The recrystallized grains were in a coarse band along a direction close to the maximum resolved shear stress. Only DT1 bands were detected at 300°C (Fig. 6c and d) but there was no evidence of contraction twins at 500°C (Fig. 6e and f). The above twinning relationships were confirmed by the misorientation distribution function analysis of the EBSD data, which gives both misorientation angle and rotation axis simultaneously for any misorientation pair

over the full orientation space. Fig. 7 shows misorientation distribution for the sample deformed at 20°C, by presenting rotation axis in the standard unit stereographic projection triangle as a function of misorientation with a series of sections from 6° to 95° at an interval of 10°. It was found that both misorientation angle and rotation axis were close to the ideal crystallographic relationships for all twins with a range of errors of up to  $\pm 8^\circ$ , most likely due to deformation in the matrix or within the twin bands.

Although  $\{10\bar{1}2\}$  twinning causes expansion along the c-axis [41], many  $\{10\bar{1}2\}$  extension twins (ETs) were found throughout all crystals. The density of  $\{10\bar{1}2\}$  twins decreased with increasing temperature and at 500°C they were only observed in the end regions (Fig. 6e). Previous work [14, 42] suggested that  $\{10\bar{1}2\}$  could occur during unloading upon fracture due to residual stress from heterogeneous straining.

#### 4.2.3. Fracture behavior

Small cracks appeared randomly on the edges of the deformed crystals (Fig. 5), largely due to excessive basal slip in the sample end regions. Distinctive cracking lines (Fig. 6a, c) were found to be associated with DT1 bands at 20°C and 300°C but recrystallization made it difficult to determine the accurate orientation of associated fracture planes. The sample deformed at 200°C showed some better-defined features. Although cleavage-like in general appearance, the fracture surface exhibited ductile features. As shown in Fig. 8a, ridges, valleys and kinks due to deformation are identifiable by a naked eye. At a finer scale, ductile cups, cones and fine ridges can be seen (Fig. 8b) together with areas of wave-like patterns (Fig. 8c). These features suggest that plastic deformation occurred prior to complete failure. A coarse EBSD mapping was performed on the fracture surface to characterize the orientation distribution as shown in the pole figure in Fig. 8d. There is a spread of basal plane poles from the initial position,  $P_O$ ,  $\sim 43^\circ$  of the fracture surface, to the pole center,  $P_C$ , where



the basal plane becomes parallel to the fracture surface. This represents an orientation rotation to develop a basal texture on the fracture surface due to basal slip in the fracture process. The fracture split the crystal into nearly two equal parts (Fig. 5b) through a plane inclined at an angle of  $\sim 43^\circ$  to the basal plane, which is similar to the inclination angle for  $\{10\bar{1}2\}$  ETs. As shown in Fig. 8e, on the longitudinal section perpendicular to the fracture surface, the fracture surface appears to be parallel to  $\{10\bar{1}2\}$  twins. Viewing from the c-axis direction (Fig. 8f), however, the fracture plane was revealed to align with a plane in-between two sets of  $\{10\bar{1}2\}$  bands and perpendicular to the third variant of  $\{10\bar{1}2\}$  twins. This suggests that the fracture was irrelevant to  $\{10\bar{1}2\}$  twinning and most likely occurred in response to the maximum resolved shear stress, which is about  $45^\circ$  to the compression axis. Fig. 10 shows EBSD data obtained from a longitudinal plane approximately perpendicular to the through-sample fracture plane in the sample deformed at  $400^\circ\text{C}$  (Fig. 5d). It can be seen that the fracture plane is coincided with a band that was within  $56\pm 10^\circ$  to the matrix as highlighted in blue on both the EBSD map and (0001) pole figure. Since a  $\{10\bar{1}1\}$  twin has a misorientation of  $56^\circ$  to the matrix and a  $\{10\bar{1}1\}$  twinning plane inclines at about  $62^\circ$  to the basal plane, it is reasonable to assume that the fracture was initiated from a  $\{10\bar{1}1\}$  twin. The band at the top of the fracture was bent away from the ideal  $\{10\bar{1}1\}$  twin orientation, probably due to the severe material side flow there.

## 5. Discussion

### 5.1. Crystallographic disproof of $\langle c+a \rangle$ slip

The core structures for an edge  $\langle 11\bar{2}3 \rangle \{11\bar{2}2\}$  dislocation reconstructed in Section 3 are considered to have the least possible energies as the related lattice distortions are minimal.

The dislocation structure formed by removing atoms from a single half atomic plane as

shown in Fig. 2b and c has the very least energy than other possible structures. However, there are a few issues with this dislocation structure, in addition to the generation of a stacking fault below the dislocation line as pointed out earlier. Firstly, the density of atoms on the  $(3\bar{3}6\bar{1}6)$  plane is so low that the removal of a single plane (AB) results in the formation of only two strings of vacancies at site A and site B within the field of view. These vacancy strings are rather isolated features as they are 11  $(11\bar{2}2)$  planes apart and there seems to be no differences between the vacancy string at site A and B, although the string at site A is supposed to be the dislocation line. Secondly, on the extra half atomic plane BA', atom A' (in red) is the nearest neighbor of atom A in the front plane of slip (the paper plane) and is on the 24th  $(11\bar{2}2)$  plane counting from the slip plane AC. Such an atomic plane cannot behave collectively and coordinatively during deformation. Thirdly, individual vacant sites along the dislocation line are separated by three  $(1\bar{1}00)$  planes as shown in Fig. 2c and are not connected as a line defect as for a normal dislocation line. Clearly, this dislocation core structure does not possess the physical properties of a normal dislocation. It is essential to understand that the dislocation vector must be a translation vector and dislocation slip, via either a complete dislocation or partial dislocations, must occur in a way that it completes the lattice translation so that the crystal periodicity is restored. therefore, it is a prerequisite to remove or add 22  $\{3\bar{3}6\bar{1}6\}$  planes in the formation of an edge  $\langle 11\bar{2}3 \rangle \{11\bar{2}2\}$  dislocation so that the stacking sequence outside of the dislocation core is maintained. The dislocation formed by removing 22  $\{3\bar{3}6\bar{1}6\}$  planes shown in Fig. 2e and f thus satisfies requirement, although it is still difficult to define this structure as a proper line defect. The structure is more like a string of vacancy pairs, in each pair the vacancies are closely connected (with a distance of lattice constant a) along a  $\langle 20\bar{2}3 \rangle$  direction. However, there are two  $(1\bar{1}00)$  planes between each pair of vacancies and the defects are not integrated into a single physical entity as a line defect. The dislocation structure described in Fig. 2h and g has got the

physical features as a line defect. This dislocation core structure is associated with every plane of slip as each  $(1\bar{1}00)$  plane has one atom removed and bears one vacant site. Thus all vacant sites are connected, forming a spring-like continuous line with its axis in the  $[1\bar{1}00]$  dislocation line direction as shown in Fig. 2h. Importantly, only one atom is removed from each  $(1\bar{1}00)$  plane and as a result, the dislocation Burgers vector remains unchanged along the dislocation line. This spring-like dislocation core structure, however, is not a simple one-dimensional line defect anymore as it involves a space of four atomic lines on two lattice planes and, if existed, would involve high energies for formation and movement.

Dislocations as line defects are introduced to explain the discrepancy between the theoretical shear strength of a perfect crystal and the experimentally measured yield strength and the work-hardening phenomenon [43]. There are many theoretical approaches to account for the stress required for dislocation slip and the Peierls-Nabarro model has been widely accepted [44]. Fig. 10a shows the cross-section of an edge dislocation in a simple cubic crystal with a stacking sequence in all primitive vector directions of ...AAA.... The figure resembles the Peierls-Nabarro model of atomic movement as the dislocation moves through the lattice and demonstrates why the stress required to plastically deform a crystal with a dislocation is much less than the stress required for deforming a defect-free crystal structure. In a defect-free crystal, plastic deformation is considered to occur by slip between characteristic lattice planes and all atoms above and below the slip plane have to move relatively a distance equal to the lattice constant in the slip direction to attain the crystal periodicity. The atomic movement during dislocation slip is localized and takes place at a substantially reduced scale. The red arrows in Fig. 10a indicate approximately the distance and direction of atomic movement under the applied shear stress  $\tau$ . The atomic movement during dislocation slip from site S to N is largely limited to two lattice planes, i.e., the extra half atom plane (2) and

the plane next to it (3). In Fig. 10a, the green balls represent the initial atomic configuration and the white ones depict the final positions of the atoms after one step of dislocation slip. It can be seen that all the atoms involved have moved only a small fraction of the dislocation slip distance  $b$ . The required energy and stress are thus substantially reduced compared to that required for deforming a perfect crystal (see [43] and [44] for detailed analysis). For the edge  $\langle 11\bar{2}3 \rangle \{11\bar{2}2\}$  dislocations described in Fig. 2, the atomic movement during slip has to be different from the above description, mainly due to the huge difference in stacking sequence in the slip direction. Fig. 10b shows the atomic configuration on the cross-section of an edge  $\langle 11\bar{2}3 \rangle \{11\bar{2}2\}$  dislocation, with atoms projected from one  $(1\bar{1}00)$  plane, and the possible atomic movement required to complete a single step slip. The initial dislocation line is at site A and its final position is at site C after a single step slip. Owing to the specific stacking sequence along the  $\langle c+a \rangle$  direction, the extra half atomic plane A'A'' is  $21 \{3\bar{3}6\bar{1}6\}$  planes apart from its next symmetrical position CC'. The movement of individual atoms in the pattern as shown in Fig. 10a cannot achieve the transition of the extra half atomic plane from A'A'' to C'C''. To complete a single step slip, the atoms on  $22 \{3\bar{3}6\bar{1}6\}$  planes (No1 to 22) above the slip plane and those on another set of  $22 \{3\bar{3}6\bar{1}6\}$  planes (No 23 to 44) below the slip plane need to move relatively a distance of Burgers vector AC in the opposite directions parallel to the slip plane as indicated by red arrows in Fig. 10b. Effectively, all atoms above the slip plane have to move a distance of the Burgers vector, relative to all the atoms below, to attain the periodicity and continuity of the crystal. This is exactly what happens in the deformation of a defect-free crystal and such a dislocation has no meanings as a mechanism of plastic deformation. Yet, collective atomic slip over adjacent planes requires a high stress and may occur between close-packed planes in perfect crystals. It is beyond reality for the  $\langle 11\bar{2}3 \rangle \{11\bar{2}2\}$  slip system in Mg. The atom immediately above the dislocation line at site A is A' in Fig. 10b, the extra half atomic plane begins at A' and there are only two visible

atoms A' and A'' on the plane in the field of view. There should be no doubt that the atoms on the  $\{3\bar{3}6\bar{1}6\}$  planes are too far apart to act collectively. Besides,  $\{11\bar{2}2\}$  planes are interlocked as shown from the full atomic projection in Fig. 2b and their relative movement is physically unlikely.

The illustration in Fig. 10b is independent of actual core structures and hence the operations that can be employed to reconstruct core structures of an edge  $\langle 11\bar{2}3 \rangle \{11\bar{2}2\}$  dislocations are not important in the disproof of  $\langle 11\bar{2}3 \rangle \{11\bar{2}2\}$  dislocation. It is the nature of the crystal structure associated with the  $\langle 11\bar{2}3 \rangle \{11\bar{2}2\}$  slip system that determines its impossibility as discussed above. In the case of a screw dislocation, although the dislocation line can be better defined as it is along with the  $\langle c+a \rangle$  direction, the lattice translation has to be completed by the collective movement of atoms on the same amount of  $\{3\bar{3}6\bar{1}6\}$  planes as for an edge dislocation, which again is impossible. Although the reconstruction of possible  $\langle 11\bar{2}3 \rangle \{10\bar{1}1\}$  dislocation structures is not performed, the impossibility of  $\langle 11\bar{2}3 \rangle \{10\bar{1}1\}$  slip system is out of question as Fig. 3 shows clearly that the possible extra half atomic plane, dislocation line direction and the plane of shear all have extremely low atomic density. The atoms on these planes and directions cannot act collectively to play a role in plastic deformation.

## 5.2. Experimental disproof of $\langle c+a \rangle$ slip

The c-axis compression of Mg single crystals was conducted to support the crystallographic analysis with a comprehensive characterization of material performance. To the best of our knowledge, it is for the first time that a full set of crystallographic information was obtained by EBSD from the whole section of characteristic sample planes. Compression along c-axis provided the most favorable stress state for pyramidal dislocation slip. There are 6  $\langle 11\bar{2}3 \rangle \{11\bar{2}2\}$  and  $12 \frac{1}{3}$   $\langle 11\bar{2}3 \rangle \{10\bar{1}1\}$  slip systems and the operation of these dislocations should have led to a uniform deformation, a bulging sample and, more importantly, improved

ductility with increasing temperature. But these features were not observed and there was no evidence of  $\langle c+a \rangle$  slip in both deformation and fracture. Over the bulk volume of the samples deformed at all temperatures, none of the material flow pattern, the crystal shape change or the microstructures and textures developed supports the involvement of  $\langle c+a \rangle$  slip. Yet, the decreasing ductility with increasing temperature in the single crystal compression shows it clearly that the excellent ductility of polycrystalline Mg alloys has nothing to do with the activation of  $\langle c+a \rangle$  slip.

In previous studies, TEM studies frequently claim that  $\langle c+a \rangle$  dislocations lie along basal planes and coexist with  $\langle c \rangle$  and  $\langle a \rangle$  dislocations [11, 14, 45-48], which is explained as that  $\langle c+a \rangle$  is decomposed into  $\langle c \rangle$  and  $\langle a \rangle$  with a stacking fault between them [2, 6, 47]. Such a decomposition is energetically unfavorable and the resultant partial dislocations must be sessile as they don't share the same slip plane (it is interesting to know the details of the proposed stacking fault between the  $\langle c \rangle$  and  $\langle a \rangle$  partials but no information available). Yet,  $\langle c \rangle$  and  $\langle a \rangle$  vectors are primitive and they only make complete dislocations. There have been many proposals of  $\langle c+a \rangle$  dislocation decomposition in literature [e.g. 2, 6, 18, 21]. Unfortunately, all decompositions are based on energy calculations of the related lattice vectors without considering crystallographic feasibility. The relaxation of a complete dislocation and the resultant formation of partial dislocations must meet the lattice translation requirement, which is not justified with any of the decomposition proposals in literature. Of particular concern is the so-called off-plane decomposition, which is fundamentally questionable as it transforms a line defect into a 3D defect, in which the stacking fault involves multiple lattice planes and the related stress and strain fields are spread in the full space. TEM was not performed in the present work because it would not help in finding a non-existent body. Based on the crystallographic configuration displayed in Fig. 2 and 3,

there are no reflectors for  $\langle c+a \rangle$  dislocations as the strongest beam condition occurs with  $g = 1/d_{\{33-6-16\}}$ , i.e.,  $g \cdot b = 22.9$  ( $|b| = 6.2\text{\AA}$ ;  $|g| = 3.7/\text{\AA}$ ), which is far too large to produce any significant imaging contrast (for basal dislocation,  $g \cdot b = 2$  ( $|g| = 1/d_{\{11-20\}} = 0.625/\text{\AA}$ ,  $|b| = 3.2\text{\AA}$ )).

Computer simulation has recently become an exploitable tool in verifying  $\langle c+a \rangle$  slip. An intrinsic transition of  $\langle c+a \rangle$  dislocations into a low energy configuration was simulated based on the construction of a pair of unstable partial dislocations as the initial state [2]. This work [2] was not able to verify the existence of a complete  $\langle c+a \rangle$  dislocation but demonstrated that  $\langle c+a \rangle$  partial dislocations were unstable and decomposed automatically, depending on stress and thermal activation, into low energy, basal-dissociated immobile dislocations. Although this computational work aimed to explain the poor ductility and high hardening rate in Mg, it effectively made a case that a  $\langle c+a \rangle$  dislocation was at least both thermally and mechanically unstable. **Indeed, a comprehensive stacking fault energy analysis by the same research group [36] has suggested that pyramidal zonal dislocations are unlikely and same for  $\langle c+a \rangle$  dissociation into three partials on the Pyramidal I plane.**

### 5.2.1. Compatible deformation

The pursuit of  $\langle c+a \rangle$  slip is primarily driven by the perception that five independent slip systems are required for uniform arbitrary strain of polycrystalline aggregates, which can only be met when non-basal slips are involved. According to von Mises [49], lattice slip leads on a macroscopic scale to the translation of one part of a crystal relative to another by a motion corresponding to a simple shear, and a single simple shear determines the value of one of the independent components of the strain tensor. A strain tensor without volume change under equilibrium has five independent components. Von Mises therefore claims that five independent slip systems are required to produce a general, small, homogeneous strain

without change in volume. Taylor recognizes that for a volume-preserving arbitrary plastic deformation, 5 independent slip systems need to be simultaneously active to achieve compatibility among the homogeneously deforming randomly misoriented grains [50]. However, the strain state at a point is a physical quantity that is independent of any particular coordinate system representation, whereas the strain components represented by a symmetric second-order tensor depend on the selected coordinate-system. A strain state can be represented in any coordinate systems with an unlimited number of independent components sets, although the principal strains and strain tensor invariants remain the same. Dislocation slip leads to relative movement of atoms and a unit slip generates a lattice displacement characterized by its Burgers vector  $\mathbf{b}$ , contributing directly to the relative displacement vector in deformation rather than a single component of a strain tensor. The correlation between slip and strain tensor components is invalid both physically and dimensionally. Although widely accepted, the von Mises criterion is unfounded and irrelevant to strain accommodation. In fact, despite the apparent failure to fulfil the von Mises criterion, Mg alloys can exhibit respectable ductility in the range of 15–25% at room temperature without involving  $\langle c+a \rangle$  slip. Strain accommodation occurs between regions and grains rather than at each point in the material as suggested by von Mises criterion. In a recent investigation on the deformation accommodation in an AZ31 Mg alloy, it has been shown that deformation is significantly heterogeneous from inside grain to grain boundaries and basal slips are responsible for both uniform deformation inside grain and highly strained grain boundary areas [5]. Improved ductility at elevated temperatures for Mg polycrystals is attributed to dynamic recrystallization, which constantly optimizes grain structures and orientation distribution for strain accommodation.

## 6. Conclusions



Fundamental issues of  $\langle 11\bar{2}3 \rangle \{11\bar{2}2\}$  and  $\langle 11\bar{2}3 \rangle \{10\bar{1}1\}$  pyramidal  $\langle c+a \rangle$  dislocations have been discussed to address the physical and energetic impossibility of their existence. The atomic configurations and crystallographic features in association with these non-basal dislocations have been reconstructed for the first time, demonstrating that the possible core structures of both  $\langle 11\bar{2}3 \rangle \{11\bar{2}2\}$  and  $\langle 11\bar{2}3 \rangle \{10\bar{1}1\}$  dislocations would involve too many non-nearest neighbor atoms on multiple lattice planes and that such a collection of atoms cannot respond coordinatively to the applied stress and act as a mechanism of plastic deformation. Both the mechanical response and behavior of deformation and fracture during c-axis compression of Mg single crystals at room temperature and elevated temperatures of up to 500°C showed no evidence of the involvement of pyramidal  $\langle c+a \rangle$  dislocations, providing physical disproof of  $\langle c+a \rangle$  slip as an essential deformation mechanism for magnesium.

### **Acknowledgement**

The authors are grateful to Mr. Kai Zhang at Imperial College for his support in mechanical testing. Helpful discussions are highly appreciated with Prof. Kenong Xia at the University of Melbourne, Prof. Yanjun Li at Norwegian University of Science and Technology, and with Dr. Ebad Bagherpour, Prof. Hamid Assadi and Prof. Dmitry Eskin at Brunel University London. This work was supported by the EPSRC (EP/N007638/1, EP/N011368 and EP/R001715).

### **References**

1. S. R. Agnew, Deformation mechanisms of alloys. In: Advances in Wrought Magnesium Alloys: Fundamentals of Processing, Properties and Applications; Ed: C. Bettles, M. Barnett, Woodhead Pub Ltd, 2012.

2. Z. Wu, W. A. Curtin, The origins of high hardening and low ductility in magnesium, *Nature* 526 (2015) 62-67.
3. S. R. Agnew, O. Duygulu, Plastic anisotropy and the role of non-basal slip in magnesium alloy AZ31, *Inter. J. Plasticity* 21 (2005) 1161-1193.
4. U. F. Kocks, D. G. Westlake, The importance of twinning for the ductility of CPH poly/crystals, *Trans. TMS-AIME* 239 (1967) 1107-1109.
5. M. R. Barnett, Twinning and the ductility of magnesium alloys: Part I: "Tension" twins, *Mater. Sci. Eng. A464* (2007) 1-7.
6. B-Y. Liu et al, Large plasticity in magnesium mediated by pyramidal dislocations, *Science* 365(6448) (2019) 73-75.
7. R. E. Reed-Hill, W. D. Robertson, The crystallographic characteristics of fracture in magnesium single crystals, *Acta Metall.* 5 (1957) 717-726.
8. H. Yoshinaga, R. Horiuchi, Deformation mechanisms in magnesium single crystals compressed in the direction parallel to hexagonal axis, *Trans. JIM* 4(1963) 1-8.
9. P. B. Hirsh, J. S. Lally, The deformation of magnesium single crystals, *Phil. Mag.* 12 (1965) 595-648.
10. J. F. Stohr, J. P. Poirier, Etude en microscopie electronique du glissement pyramidal  $\{11\bar{2}\}$   $\langle 11\bar{2}3 \rangle$  dans le magnesium, *Philos. Mag.* 25 (1972) 1313-1329.
11. T. Obara, H. Yoshinga, S. Morozum,  $\{11\bar{2}2\}\langle 11\bar{2}3 \rangle$  slip system in magnesium, *Acta Metall.* 21 (1973) 845-853.
12. S. Ando, M. Tsushida, H. Kitahara, Deformation behavior of magnesium single crystal in c-axis Compression and a-axis Tension, *Mater. Sci. Forum* 654-656 (2010) 699-702.
13. Q. Li, Dynamic mechanical response of magnesium single crystal under compression loading: Experiments, model, and simulations, *J. Appl. Phys.* 109 (2011) 103514.

14. B. Syed, J. Geng, R.K. Mishra, K.S. Kumar, [0001] compression response at room temperature of single-crystal magnesium, *Scripta Mater.* 67 (2012) 700-703.
15. C. M. Byer, B. Li, B. Cao, K. T. Ramesh, Microcompression of single-crystal magnesium. *Scr. Mater.* 62, 536–539 (2010).
16. E. Lilleodden, Microcompression study of Mg (0001) single crystal, *Scr. Mater.* 62, 532-535 (2010).
17. Y. K. Xie, Z. Alam, A. Caffee, K. J. Hemker, Pyramidal I slip in c-axis compressed Mg single crystals. *Scripta Mater.* 112 (2016) 75-78.
18. Y. Tang, J. A. El-Awady, Formation and slip of pyramidal dislocations in hexagonal close-packed magnesium single crystals, *Acta Mater.* 71 (2014) 319-332.
19. X-Z. Tang, Y-F. Guo, S. Xu, Y-S. Wang, Atomistic study of pyramidal slips in pure magnesium single crystal under nano-compression, *Phil. Mag.* 95 (2015) 2013-2025.
20. M. Itakura *et al*, Novel cross-slip mechanism of pyramidal screw dislocations in magnesium, *Phys. Rev. Lett.* 116 (2016) 225501.
21. Z. Ding *et al*, Origins and dissociation of pyramidal  $\langle c+a \rangle$  dislocations in magnesium and its alloys, *Acta Mater.* 146 (2018) 265-272.
22. S. Sandlobes, S. Zaeferrer, I. Schestakow, S. Yi, R. Gonzalez-Martinez, On the role of non-basal deformation mechanisms for the ductility of Mg and Mg-Y alloys, *Acta Mater.* 59 (2011) 429-439.
23. B. Li, E. Ma, Pyramidal slip in magnesium: Dislocations and stacking fault on the  $\{10\bar{1}1\}$  plane, *Phil. Mag.* 89 (2009) 1223-1235.
24. B. C. Wonsiewicz, W. A. Backofen, Plasticity of magnesium crystals, *Trans. Metall. Soc. AIME* 239 (1967) 1422-1431.

25. K. D. Molodov, T. Al-Samman, D. A. Molodov, G. Gottstein, Mechanisms of exceptional ductility of magnesium single crystal during deformation at room temperature: multiple twinning and dynamic recrystallization, *Acta Mater.* 76 (2014) 314-330.
26. C. Zambaldi, C. Zehnder, D. Raabe, Orientation dependent deformation by slip and twinning in magnesium during single crystal indentation, *Acta Mater.* 91 (2015) 267-288.
27. K. A. Gschneider, Physical properties and interrelationships of metallic and semimetallic elements, *Solid State Physics.* 16 (1964) 308-315.
28. A. Bondi, van der Waals volumes and radii, *J Phys Chem* 64 (1964) 441-451.
29. P. Atkins, L. Jones, *Chemical Principles: The Quest for Insight* (4<sup>th</sup> ed.), W. H. Freeman and Company, 2008, p. 236.
30. J. Kerr, Strengths in chemical bonds: in *Handbook of Chemistry and Physics* (85<sup>th</sup> ed.), D.R. Lide (ed.), CRC Press, 2003, p. 9-54.
31. W. Domcke, P. Hänggi, D. Tannor, Dynamics of driven quantum systems, *Chem. Phys.* 217 (1997) 117- 416.
32. S. Takeuchi, T. Hashimoto, K. Maeda, Plastic deformation of bcc metal single crystals at very low temperatures, *Trans. Japan Ins. Met.* 23 (1982) 60-69.
33. U. Müller, Symmetry relationships between crystal structures: applications of crystallographic group theory in crystal chemistry, Oxford University Press, Oxford, 2013.
34. T. B. Massalski, Structure and stability of alloys, In: *Physical Metallurgy*, R. W. Cahn, P. Haasen (ed) (4<sup>th</sup> ed.), North-Holland, 1996, p.135-203.
35. V. Vitek, Intrinsic stacking faults in body-centred cubic crystals, *Philos. Mag.* 18 (1968) 773-786.
36. B. Yin, Z. Wu, W. A. Curtin, Comprehensive first-principles study of stable stacking faults in hcp metals. *Acta Mater.* 123 (2017) 223-234.

37. X. Wu, R. Wang, S. Wang, Generalized-stacking-fault energy and surface properties for hcp metals: a first-principles study, *Appl. Surf. Sci.* 256 (2010) 3409-3412.
38. J. A. Yasi, L.G. Hector Jr., D.R. Trinkle, Prediction of thermal cross-slip stress in magnesium alloys from direct first-principles data, *Acta Mater.* 59 (2011) 5652-5660.
39. C. Hammond, Introduction to crystallography. Oxford University Press, RMS, 1990.
40. C. S. Roberts, Magnesium and its alloys, Wiley and Sons, New York, 1960.
41. M. H. Yoo, Slip, twinning, and fracture in hexagonal close-packed metals, *MTA* 12 (1981) 409-418.
42. T. Al-Samman et al, Softening and dynamic recrystallization in magnesium single crystals during c-axis compression, *Acta Mater.* 60 (2012) 537-545.
43. P.M. Anderson, J. P. Hirth, J. Lothe, *Theory of dislocations*, third edition, Cambridge University Press, 2017, p. 3-20.
44. F. R. N. Nabarro, Fifty-year study of the Peierls-Nabarro stress, *Mater. Sci. Eng. A234-236* (1997) 67-76.
45. S. Ando, H. Tonda, Non-basal slips in magnesium and magnesium-lithium alloy single crystals. *Mater. Sci. Forum* 350-351 (2000) 43-48.
46. H. Tonda, S. Ando, Effect of temperature and shear direction on yield stress by  $\{11\bar{2}2\}$   $\langle 11\bar{2}3 \rangle$  slip in HCP metals, *Metall. Mater. Trans. A33* (2002) 831-836.
47. B. Li, P. Yan, M. Sui, E. Ma, Transmission electron microscopy study of stacking faults and their interaction with pyramidal dislocations in deformed Mg, *Acta Mater.* 58 (2010) 173-179.
48. A. Kumar, B. M. Morrow, R. J. McCabe, I. J. Beyerlein, An atomic-scale modelling and experimental study of  $\langle c+a \rangle$  dislocations in Mg, *Mater. Sci. Eng. A695* (2017) 270-278.
49. R. Von Mises, Mechanik der plastischen Formaenderung von Kristallen, *Math. Mech.* 8 (1928) 161-185.

50. G. I. Taylor, Analysis of plastic strain in a cubic crystal, Stephen Timoshenko 60<sup>th</sup> Anniversary 218-228, Macmillan, New York, 1938.
51. A. Orozco-Caballero, D. Lunt, J. D. Robson, J. Quinta da Fonseca, How magnesium accommodates local deformation incompatibility: A high-resolution digital image correlation study, *Acta Mater.* 133 (2017) 367-379.

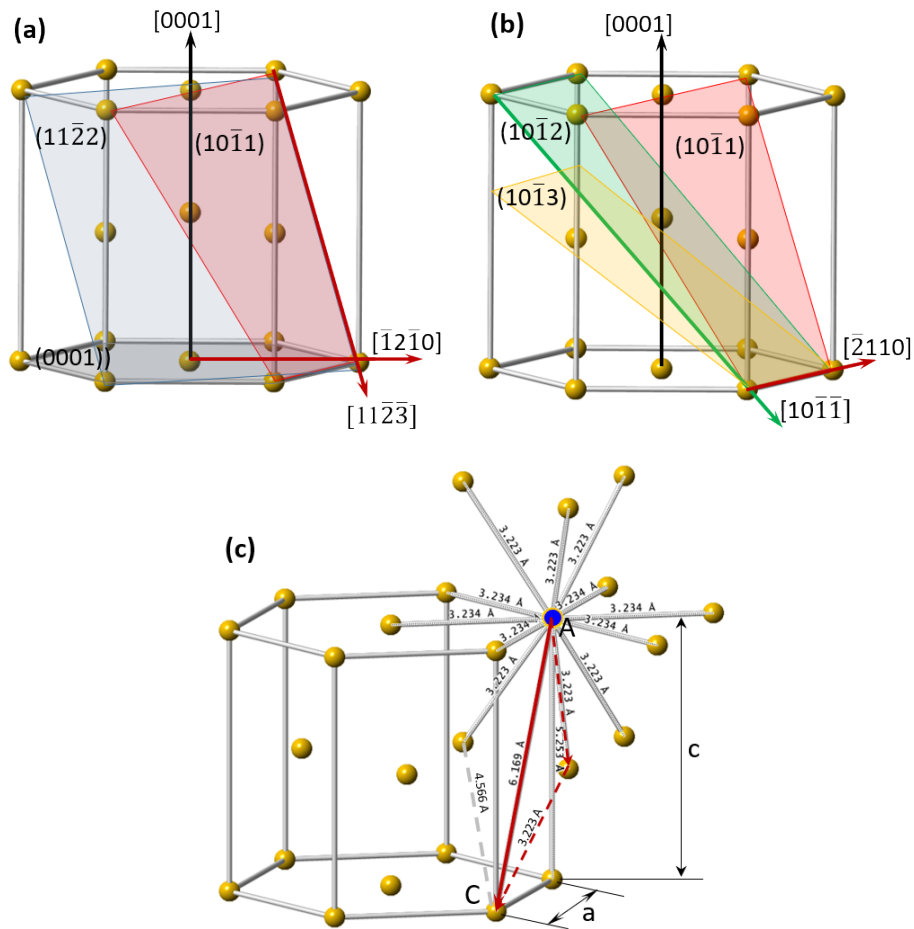
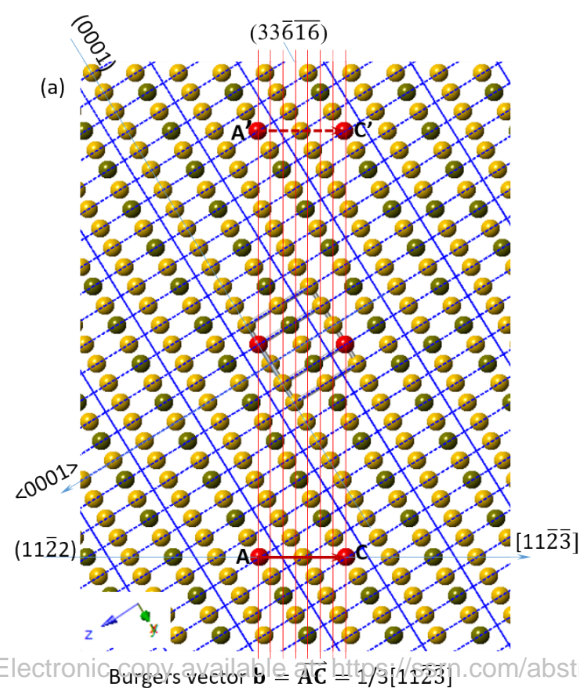
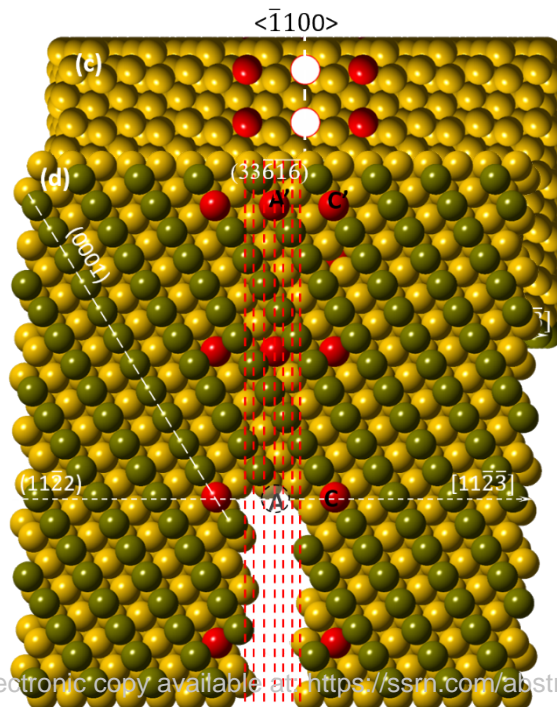
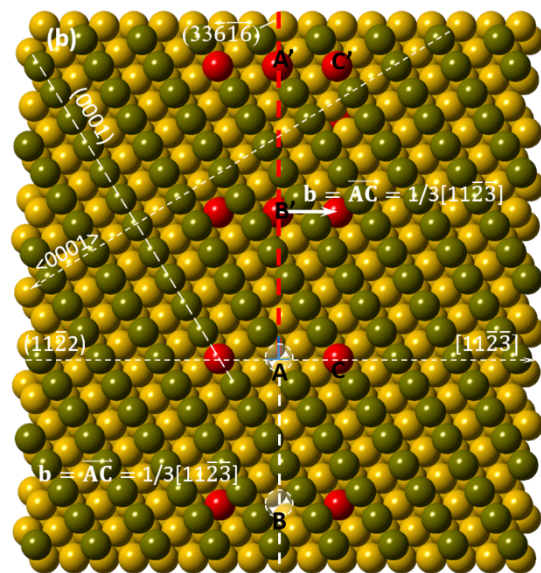
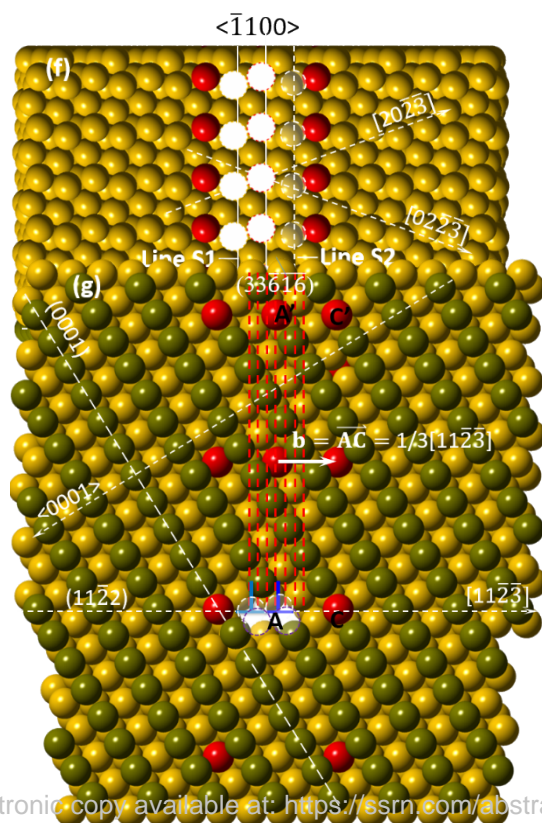
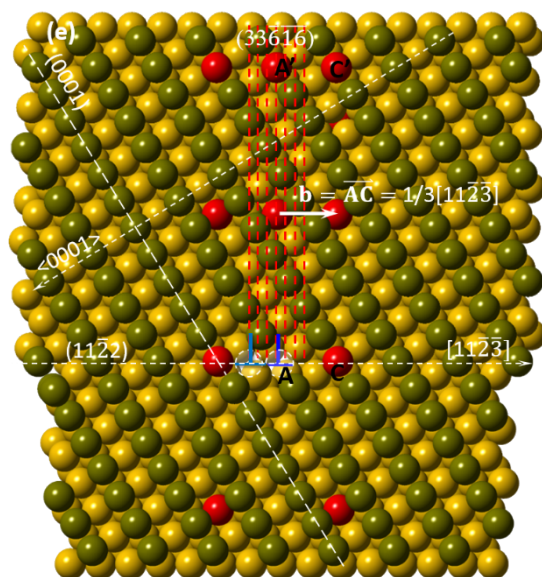


Fig.1 Unit hcp lattice illustrations of basal slip system, non-basal  $\langle c+a \rangle$  slip systems and common primary twinning systems: (a) basal slip system  $\langle 11\bar{2}0 \rangle \{0001\}$  and pyramidal  $\langle c+a \rangle$  slip systems  $\langle 11\bar{2}3 \rangle \{11\bar{2}2\}$  and  $\langle 11\bar{2}3 \rangle \{10\bar{1}1\}$ ; (b) primary  $\{10\bar{1}1\}$ ,  $\{10\bar{1}2\}$  and  $\{10\bar{1}3\}$  twinning systems; (c) pyramidal dislocation Burgers vector  $\overline{AC} = \langle c+a \rangle = 1/3 \langle 11\bar{2}3 \rangle$  and the 12 coordination atoms of atom A (same for every atoms) -  $a$  and  $c$  are lattice constants.









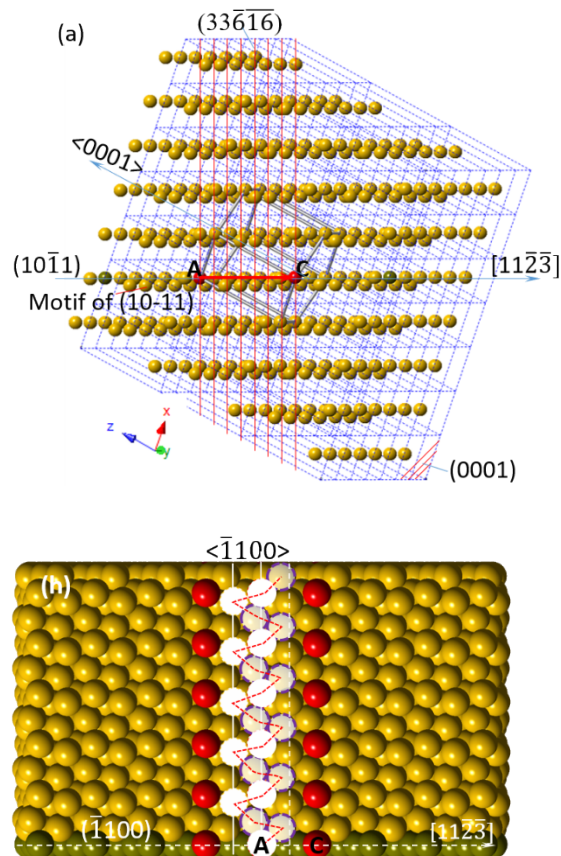


Fig. 2 Crystallographic reconstruction of an edge  $\langle 11\bar{2}3 \rangle \{11\bar{2}2\}$  dislocation with different core structures. (a) Crystallographic elements of the dislocation shown in the Ball & Stick model, including the 23  $(3\bar{3}6\bar{1}6)$  planes (only 8 red lines drawn for clarity) on Burgers vector  $\overline{AC}$  (Mg unit cell in blue lines and hcp lattice in grey lines); (b) and (c) the dislocation structure formed by removing a single half- $(3\bar{3}6\bar{1}6)$  plane; (d) the atomic configuration after removing 22 half- $(3\bar{3}6\bar{1}6)$  planes without relaxation or fixation operations; (e) and (f) the dislocation structure formed by removing 22 half- $(3\bar{3}6\bar{1}6)$  planes and refilling the whole empty space below the slip plane; (g) and (h) the dislocation structure formed by removing 22 half- $(3\bar{3}6\bar{1}6)$  planes and refilling the whole empty space, except the plane immediately below the slip plane. (b)-(h) all presented with the Full Space model.

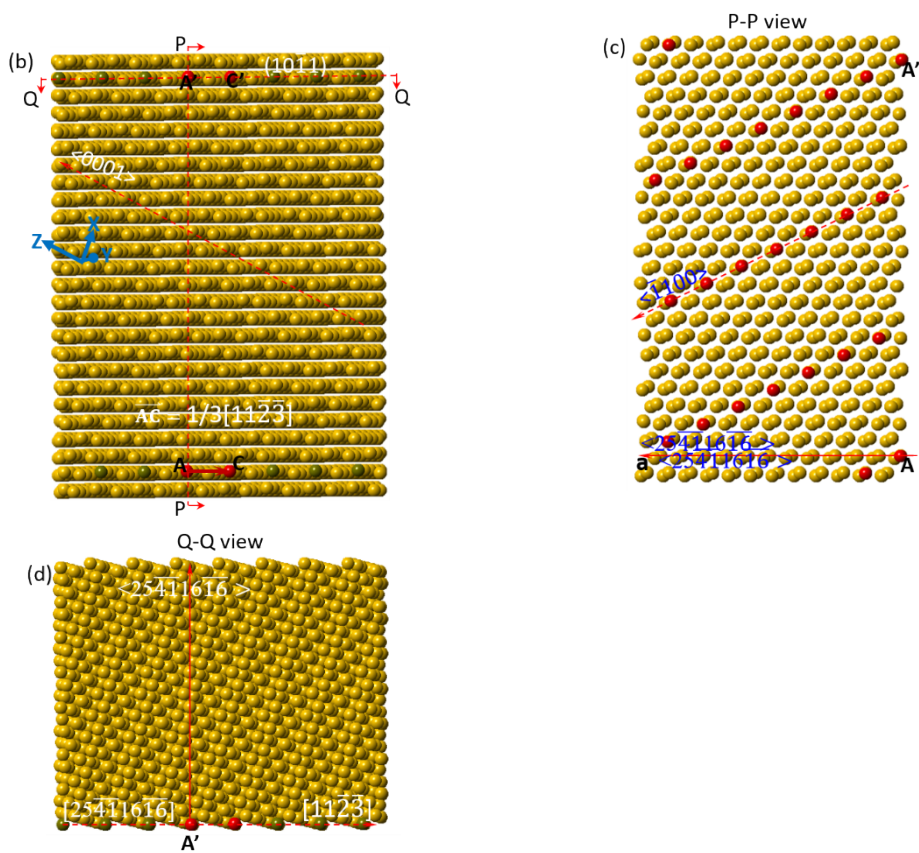


Fig. 3 Crystallographic configurations in relation to of an edge pyramidal  $\langle 11\overline{2}3 \rangle \{10\overline{1}1\}$  dislocation. (a) Ball & Stick model view of the crystallographic configuration along the dislocation line direction  $[25411616]$ , including 23  $(33\overline{6}16)$  planes (only 8 red lines drawn for clarity) on Burgers vector  $\overline{AC}$  (Mg unit cell in blue lines and hcp lattice in grey lines); (b) the full space model of the atomic configuration shown in (a) with all atoms on the paper plane highlighted in green and red; (c) the atomic configuration of a possible extra half atomic plane  $(33\overline{6}16)$ , viewing along the Burgers vector direction  $[11\overline{2}3]$  with all atoms on the paper plane highlighted in red; (d) a view of slip plane  $(10\overline{1}1)$ .

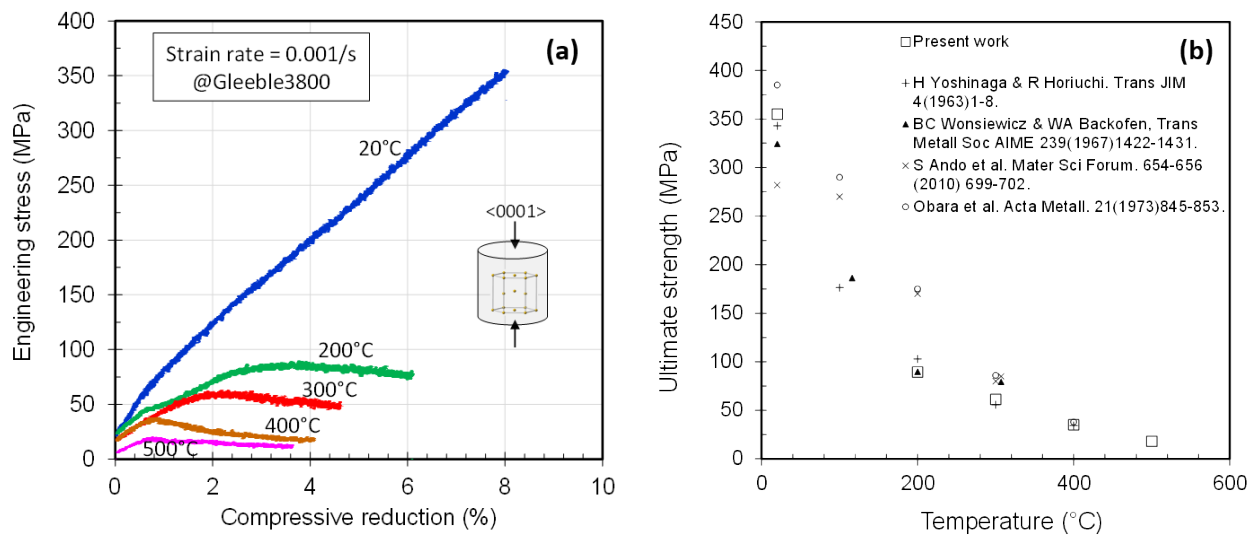


Fig. 4. Mechanical response of Mg single crystal in c-axis compression: (a) Stress vs strain curves at different temperatures; (b) Ultimate strength as a function of temperature, in comparison with data obtained under similar conditions in literature.

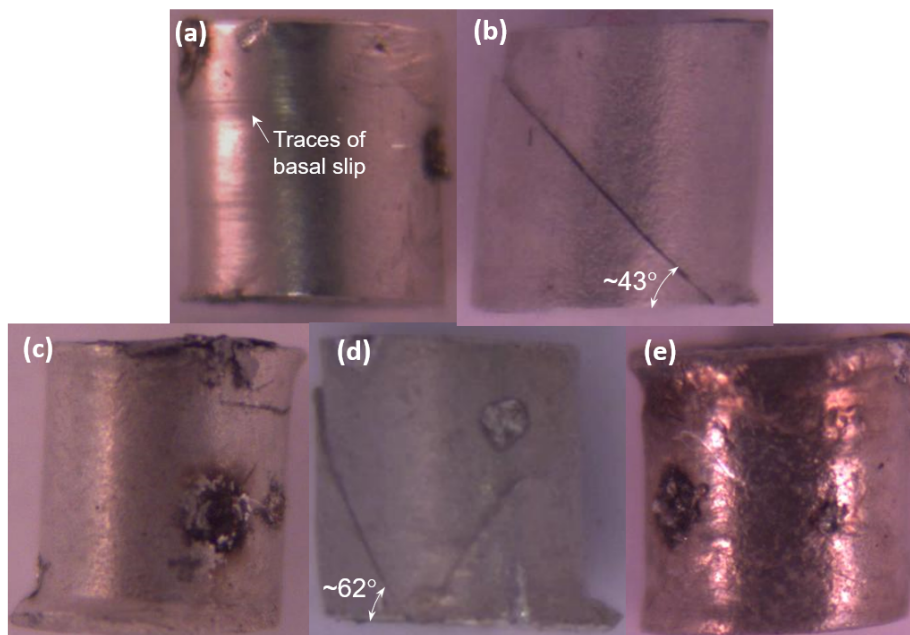


Fig. 5. Photographs of Mg single crystal samples after c-axis compression at (a) 20°C, (b) 200°C, (c) 300°C, (d) 400°C and (e) 500°C, showing features of material flow and crack development. Note: the dark areas are spots where thermal couples were welded to the sample; they were found to have no significant impact on the deformation behavior.



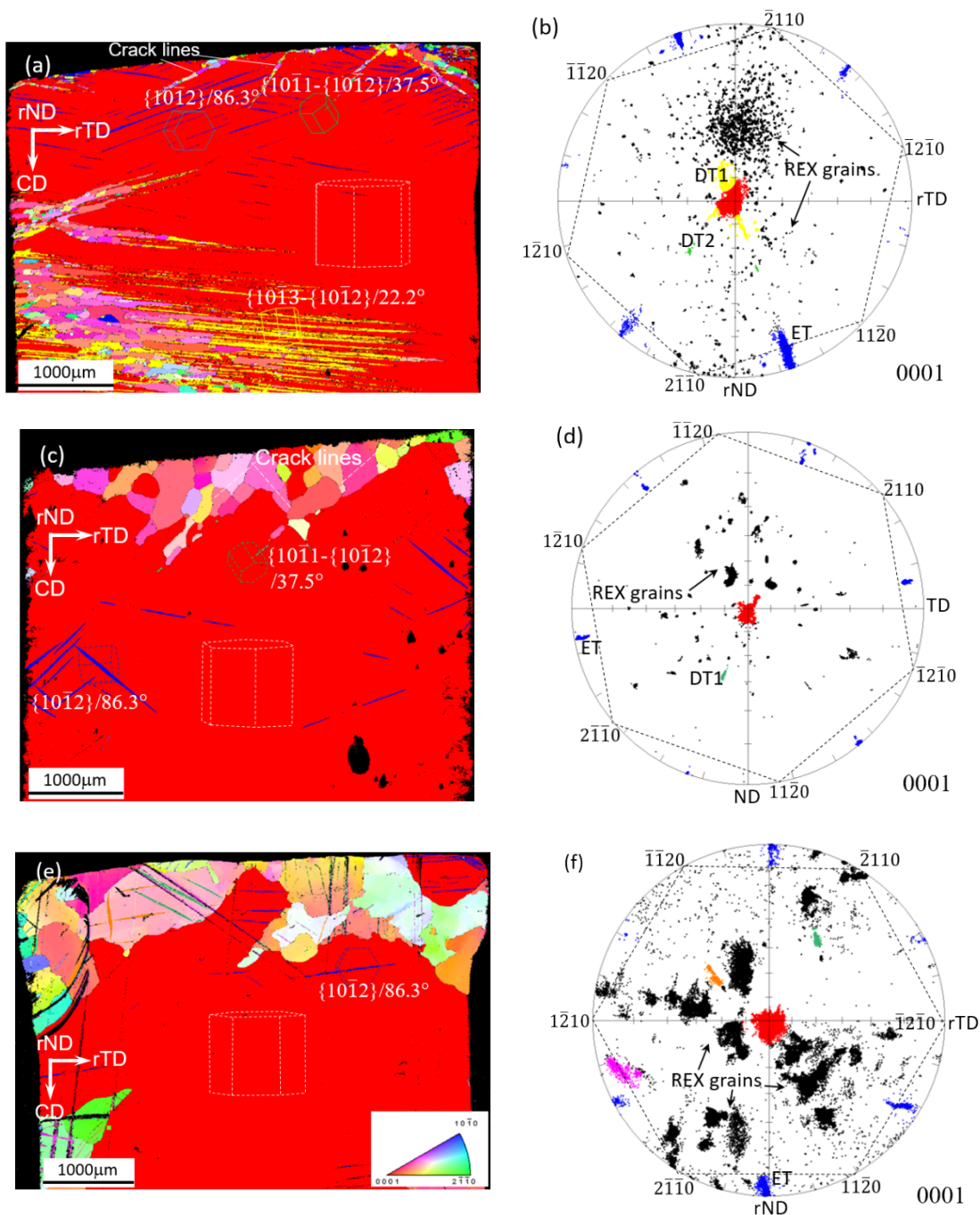


Fig. 6. Typical deformation structures and related crystallographic features: (a), (c) and (e) EBSD maps for samples deformed at 20°C, 300°C and 500°C, respectively, and (b), (d) and (f) 0001 pole figures drawn from the EBSD data in (a), (c) and (e), respectively. The matrix and twins are highlighted so that the same color in both EBSD maps and pole figures represents the same characteristic feature, except the recrystallized grains which are defined by the IPF color code (inserted in (e)). The hcp unit cell drawn by dotted lines in both EBSD maps and 0001 pole figures present the orientation of the matrix of individual samples.

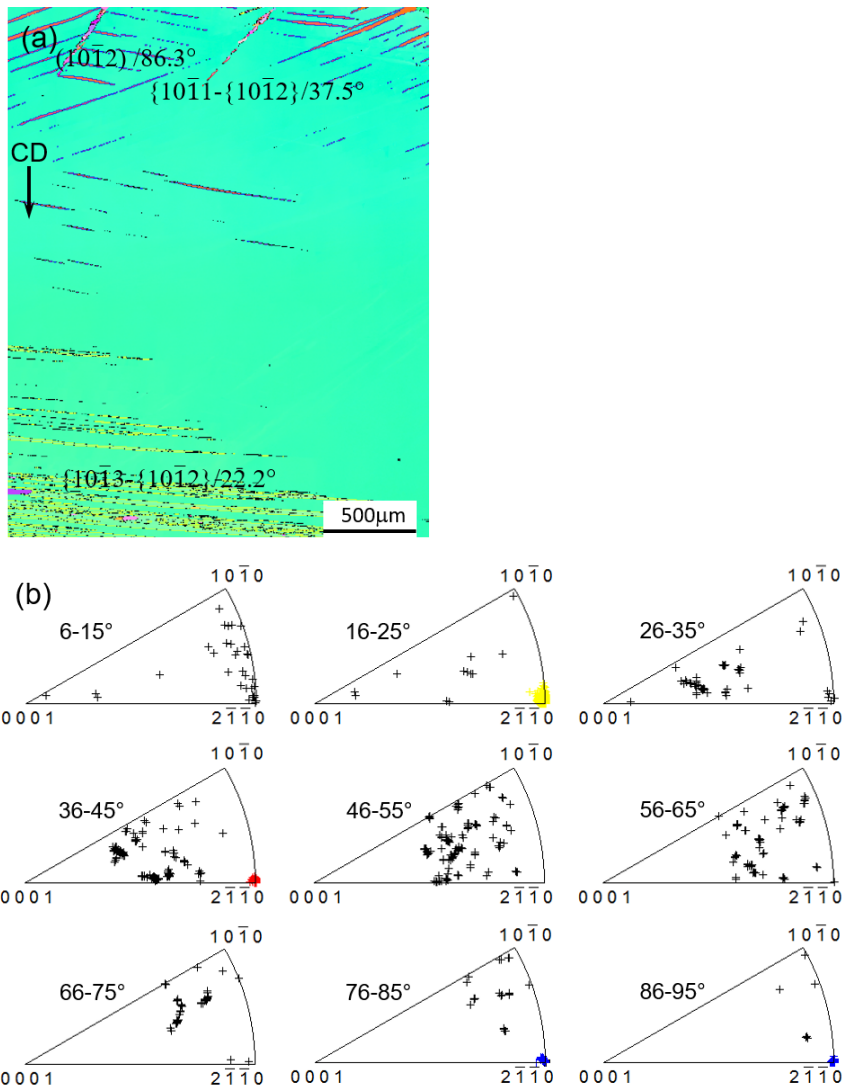


Fig. 7. An example of twinning relationship analysis using misorientation distribution function with EBAX OIM software: (a) IPF EBSD map obtained from the sample deformed at 20°C showing different types of twins highlighted in the color defined in (b); (b) rotation axis distribution as a function of misorientation shows the range of misorientation and rotation axis for individual groups of twin bands (red -  $\{10\bar{1}1\}$ - $\{10\bar{1}2\}$  DT1; yellow -  $10\bar{1}3$ - $\{10\bar{1}2\}$  DT2; blue -  $(10\bar{1}2)$  extension twins). The misorientations given to individual twin bands in (a) are the ideal values.

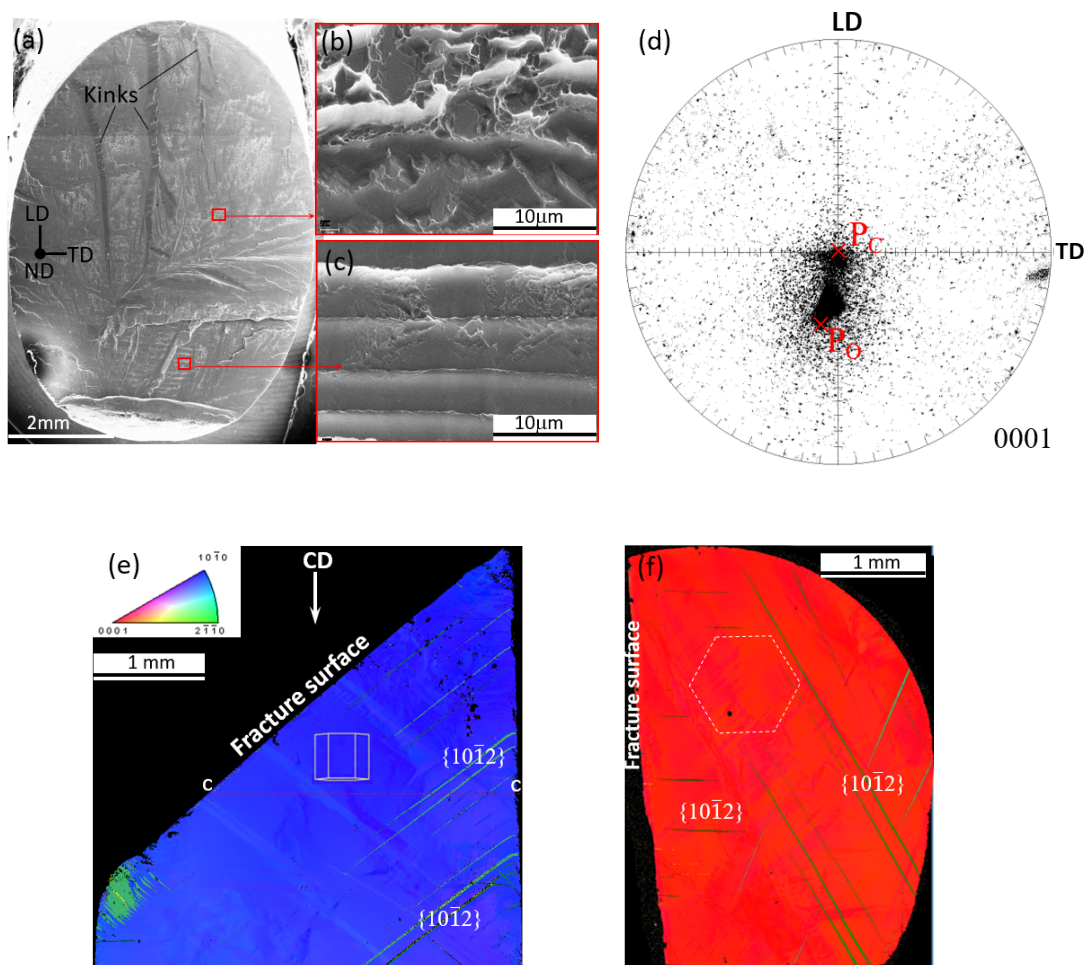
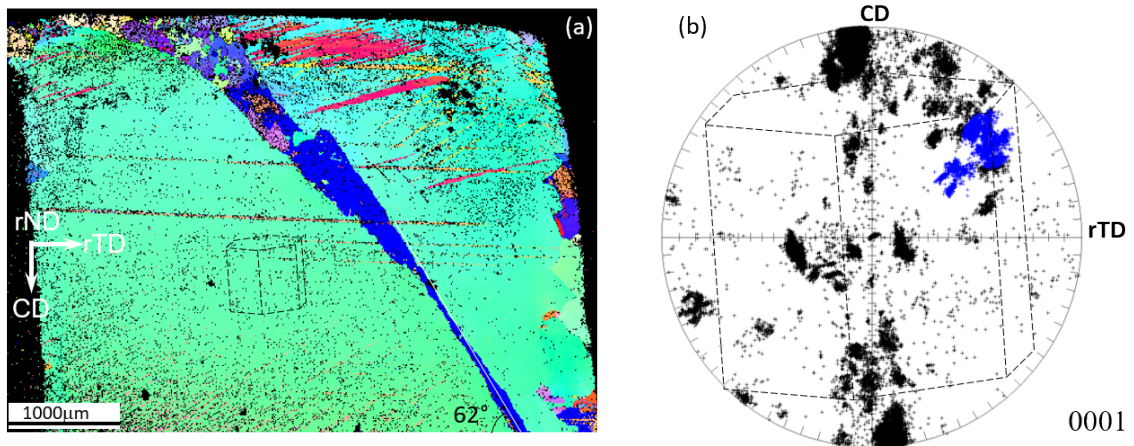
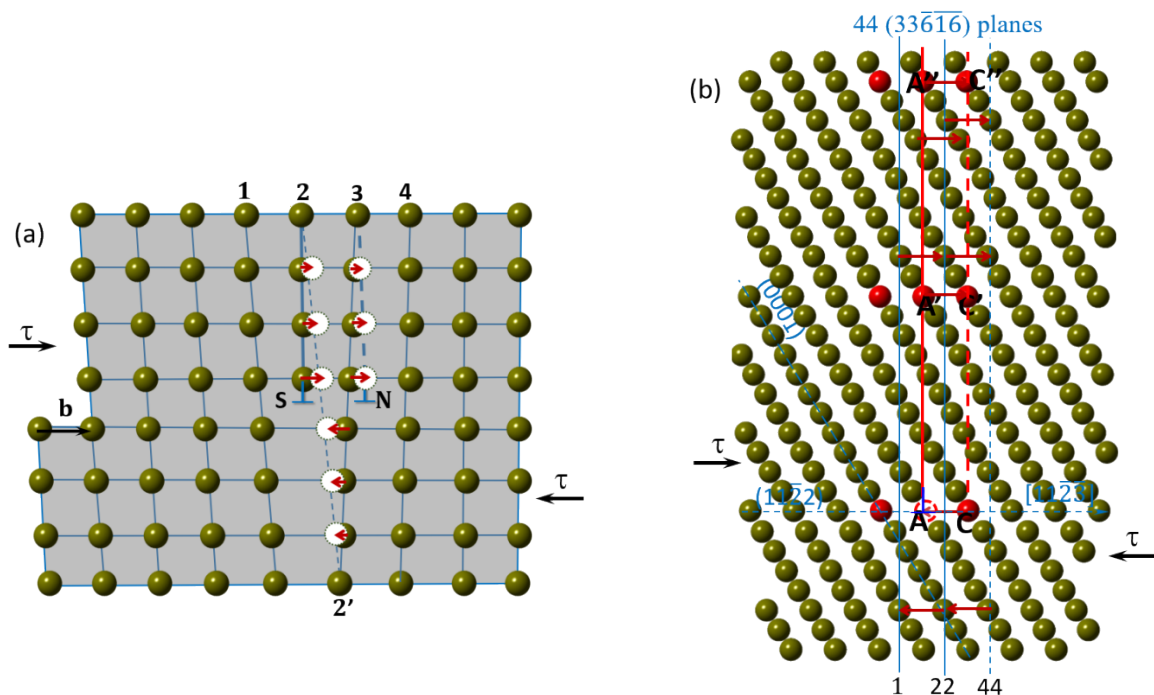


Fig. 8. Characteristic fracture features for the sample deformed at 200°C: (a), (b) and (c) SEM secondary electron micrographs showing fracture surface morphologies at a macro-scale (a) and a micron-scale (b) and (c); (d) (0001) pole figure showing orientation spread on the fracture surface; (e) IPF EBSD map from a longitudinal section perpendicular to the fracture surface showing the fracture surface is parallel to  $\{10\bar{1}2\}$  twins; (f) IPF EBSD map from a cross-section (along line C-C on (e)) normal to the compression axis showing irrelevance of the fracture surface with  $\{10\bar{1}2\}$  twins.



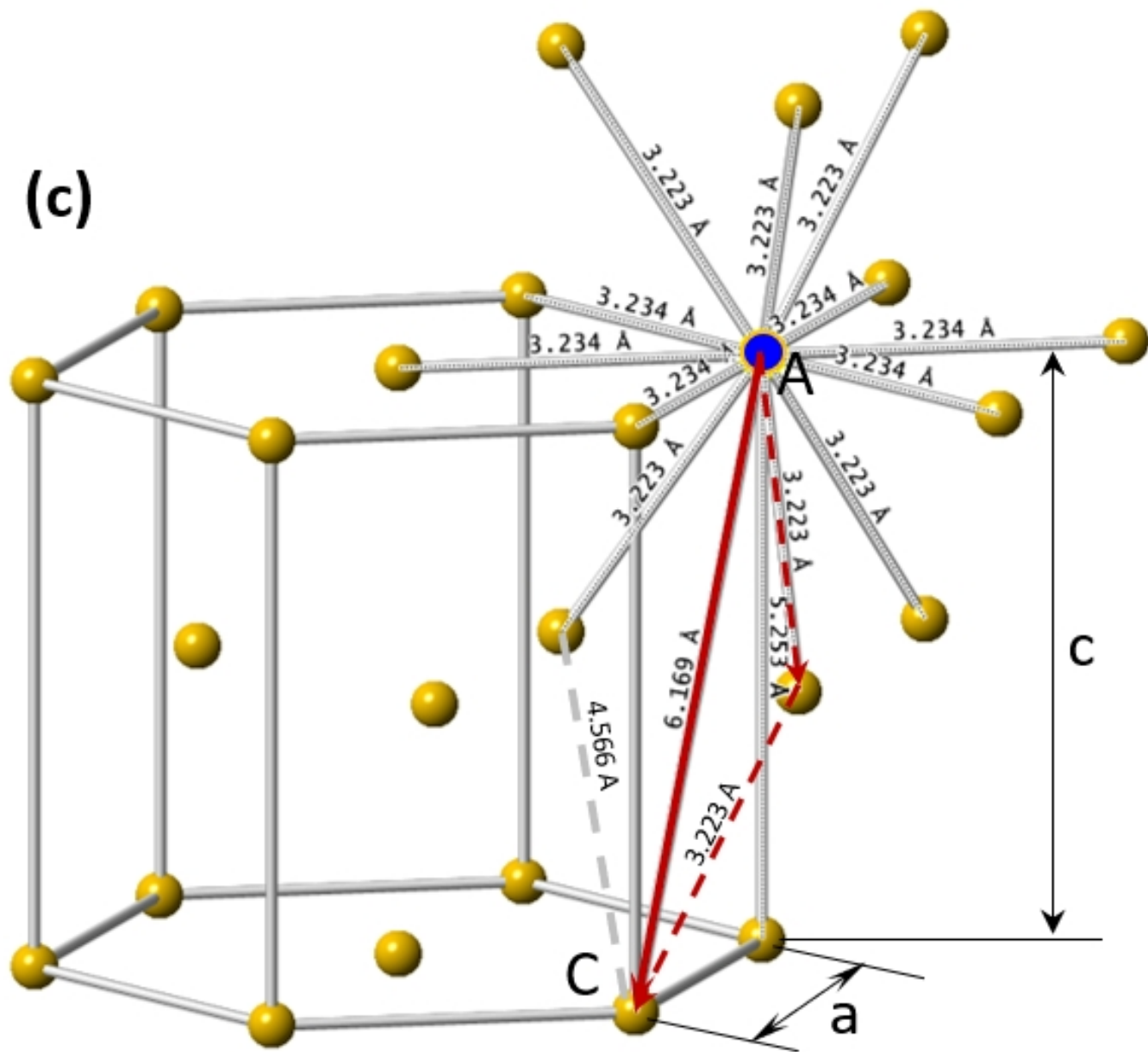
**Fig. 9.** EBSD map (a) and (0001) pole figure (b), showing that a through-sample fracture in a sample deformed at 400°C was possibly along a  $\{10\bar{1}1\}$  contraction twin, which has a misorientation of 56° and the twinning plane  $\{10\bar{1}1\}$  has an angle of about 62° to the basal plane.



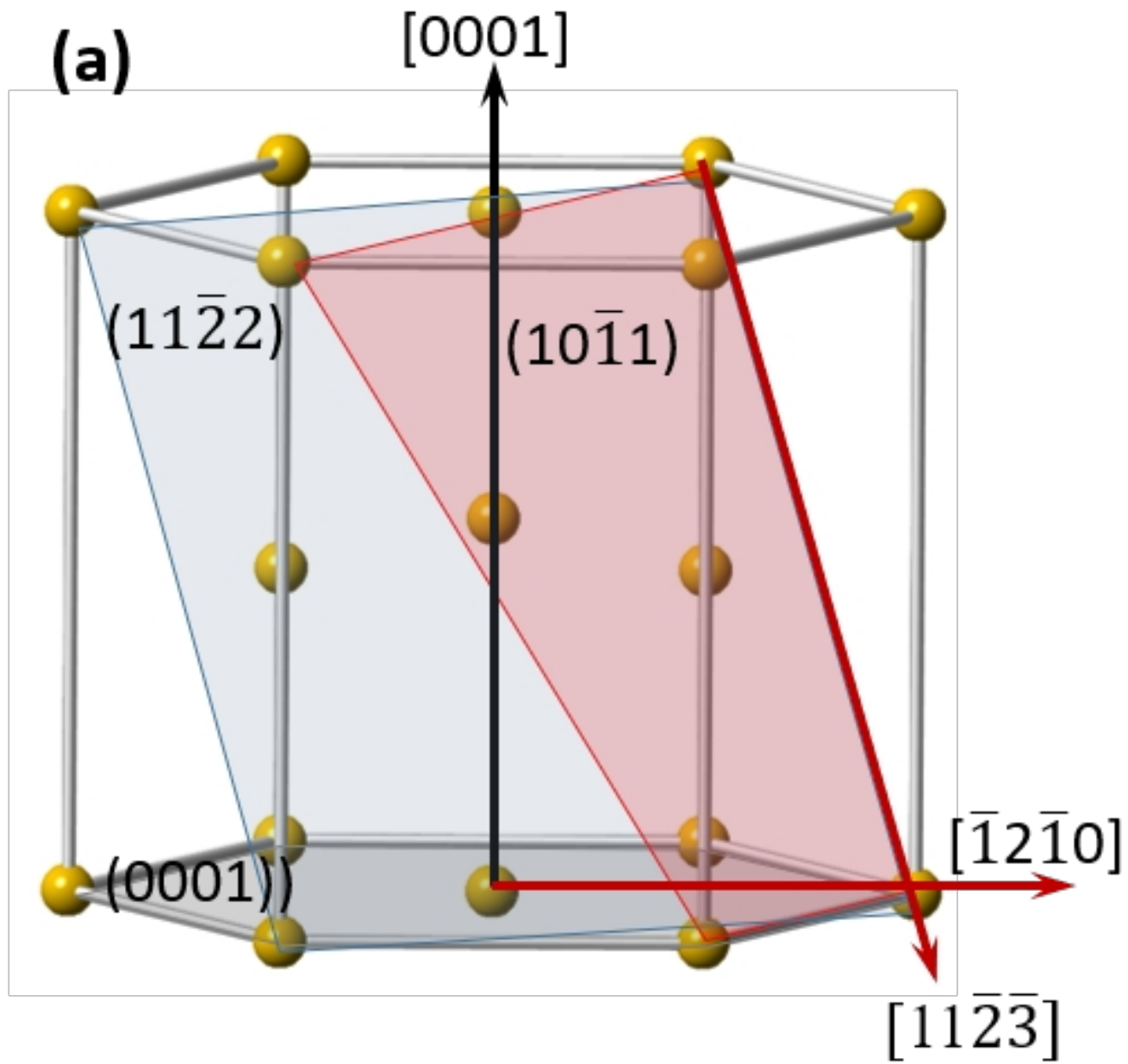
**Fig. 10.** The cross-section of an edge dislocation in a simple cubic crystal (a) and of an edge  $\langle 11\bar{2}3 \rangle \{11\bar{2}2\}$  dislocation, showing the possible atomic movement by the red arrows during dislocation slip.



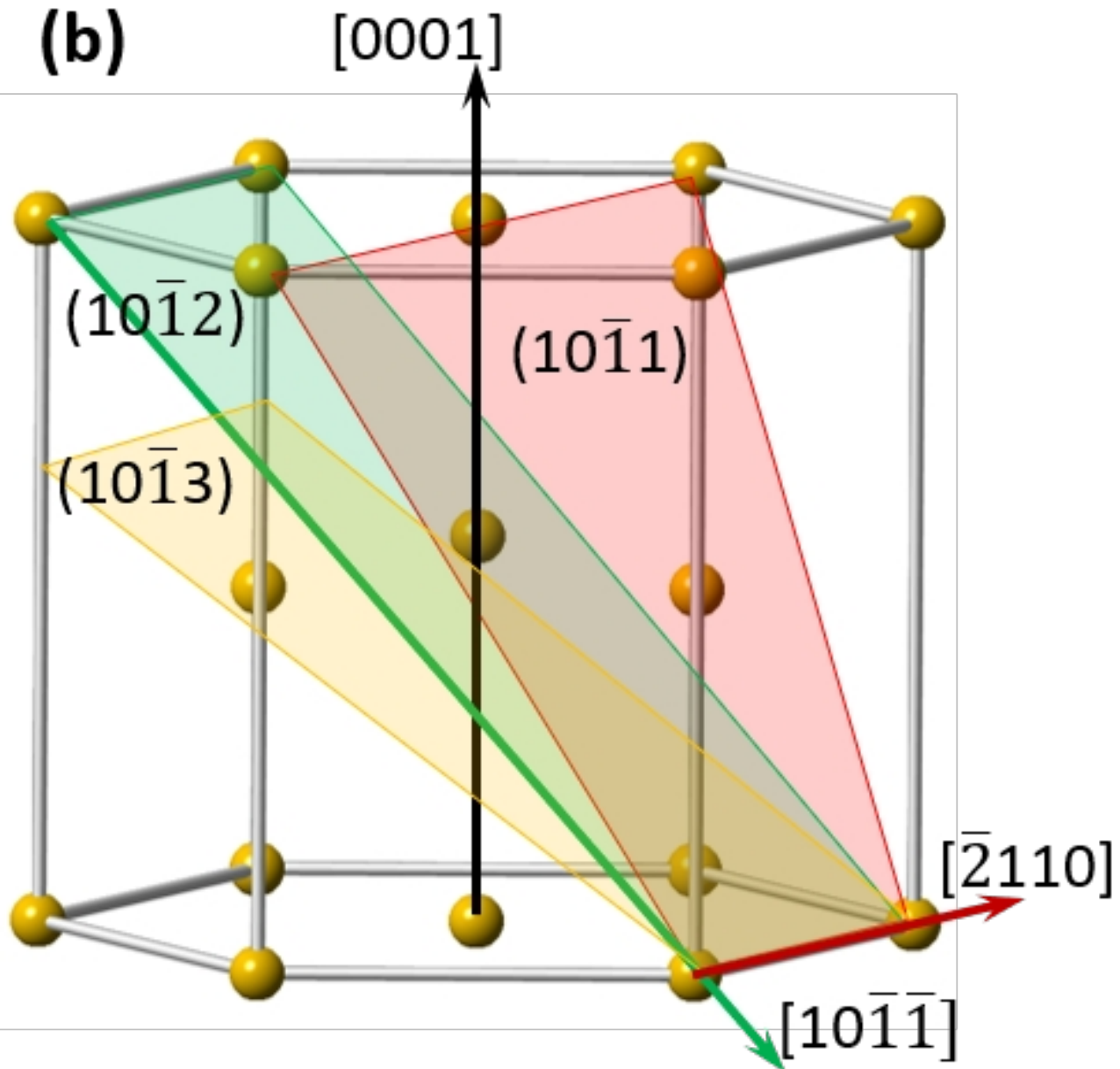
(c)



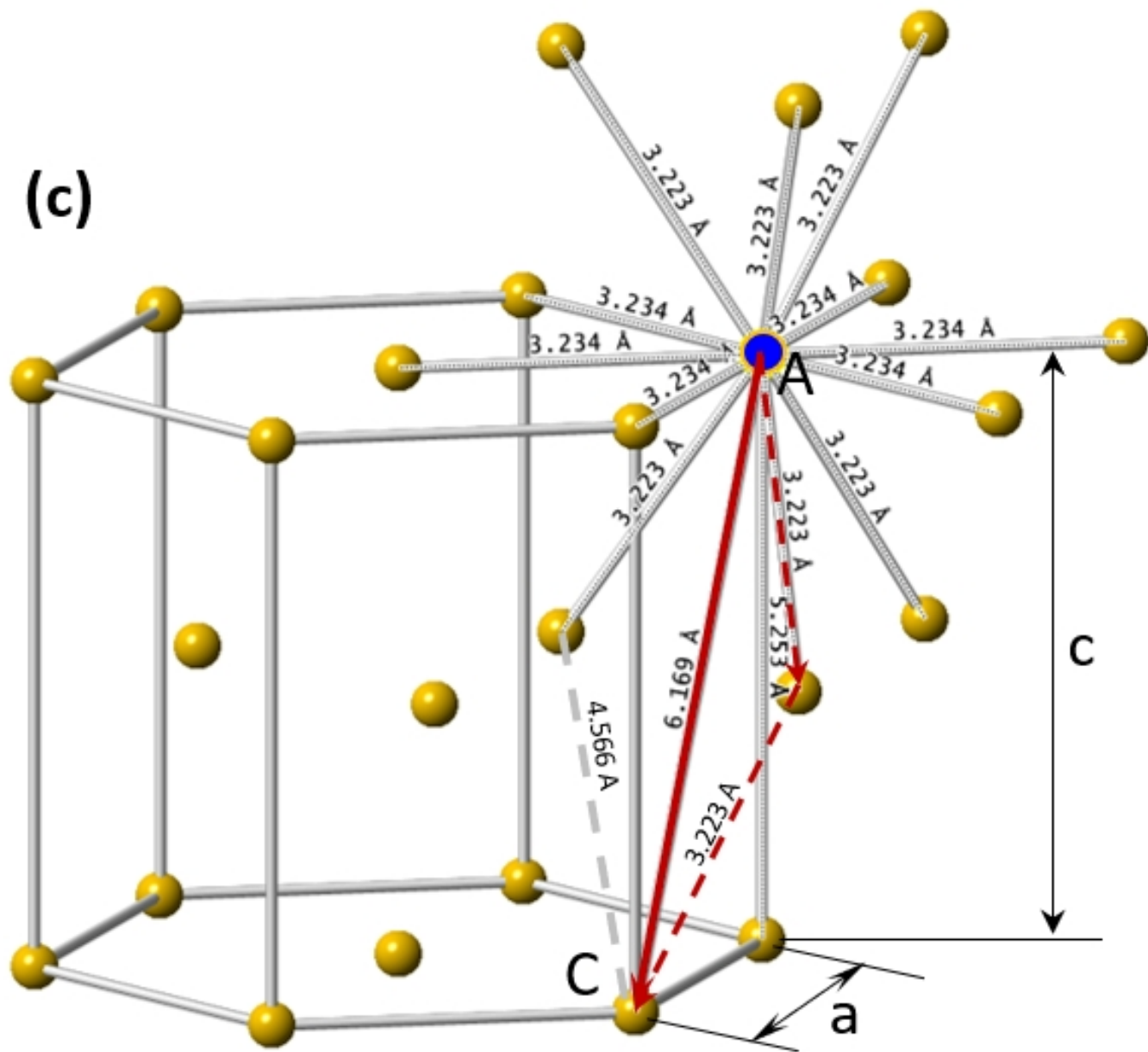
(a)

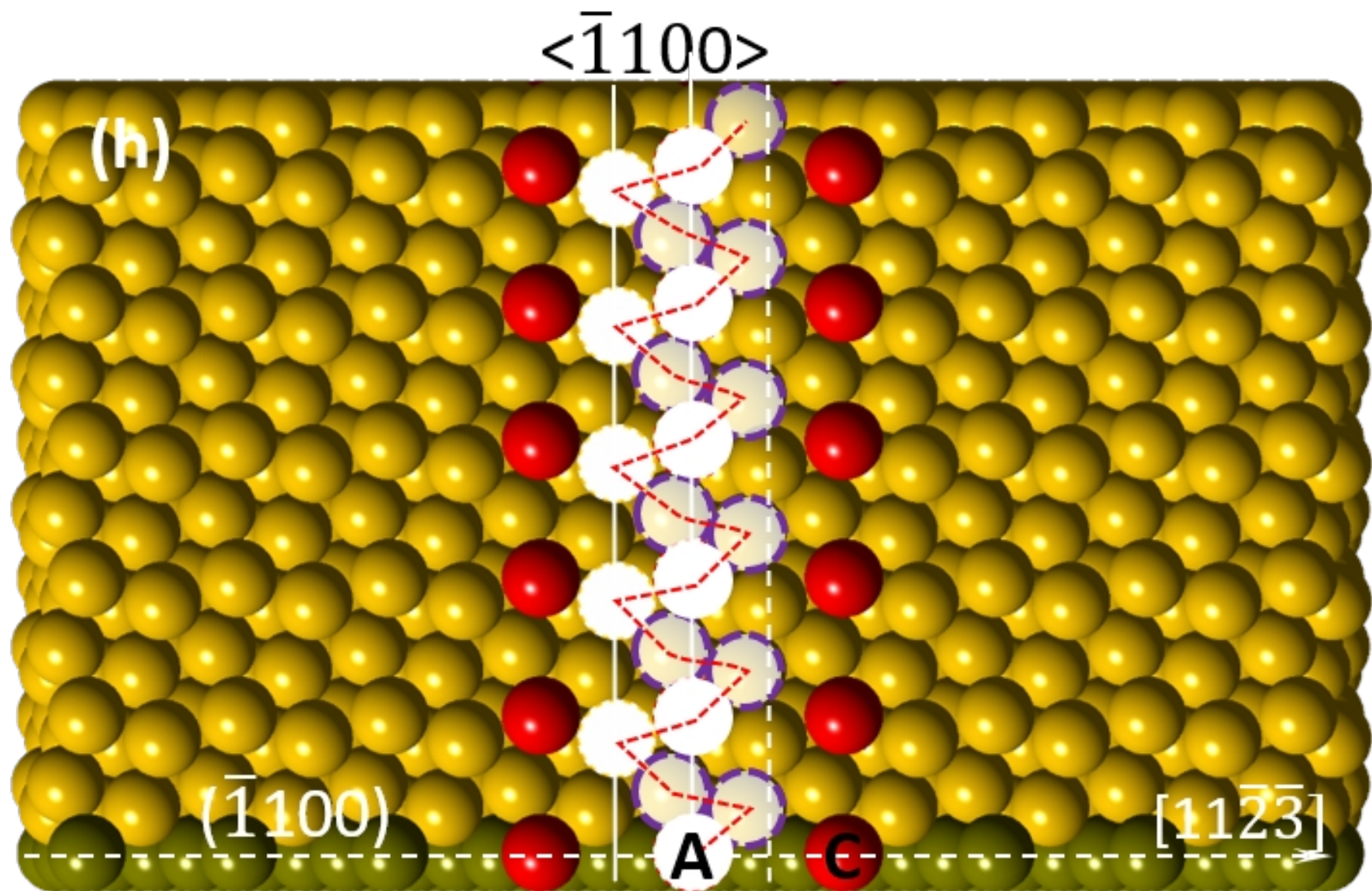


**(b)**

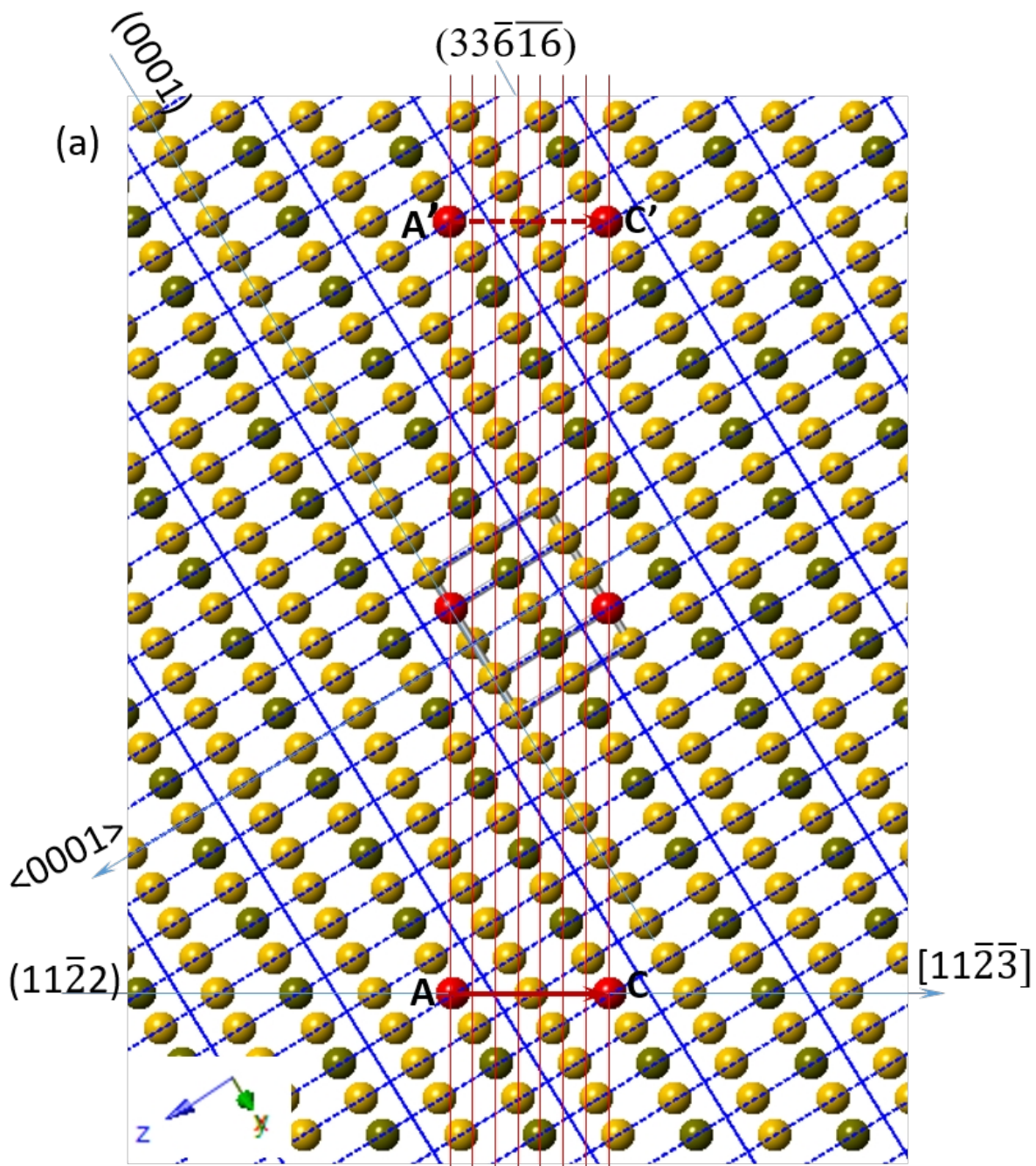


(c)

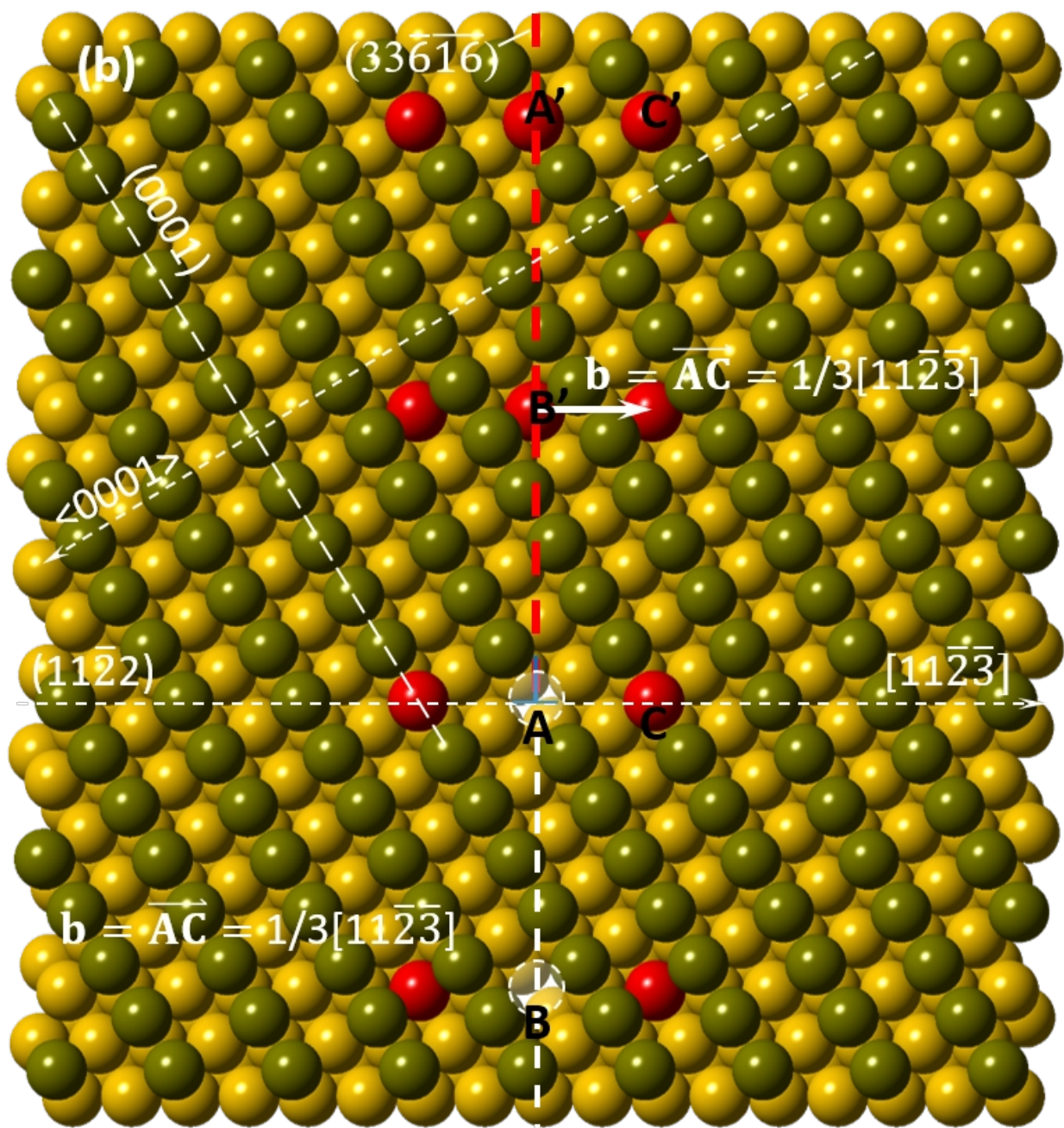




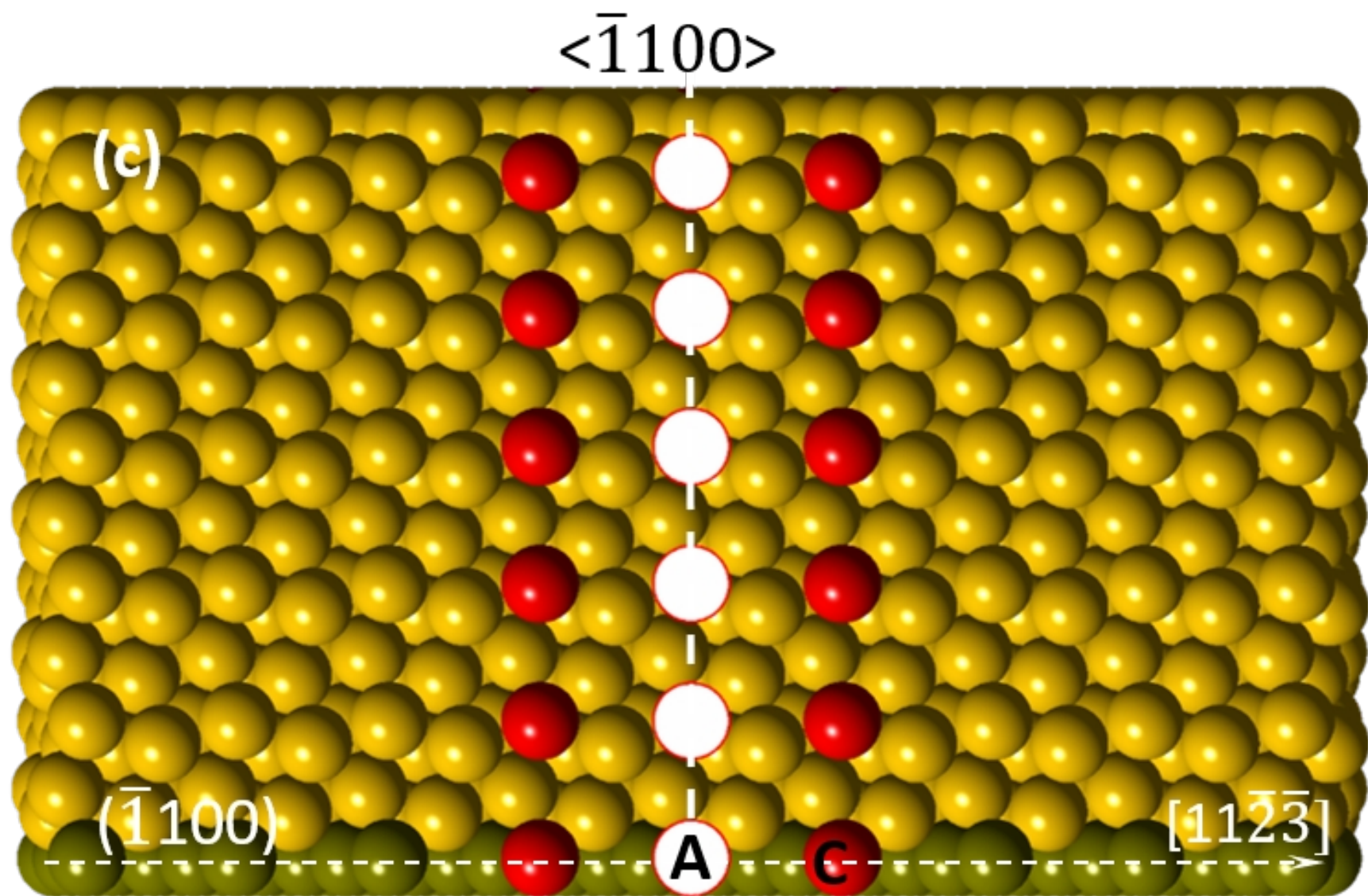




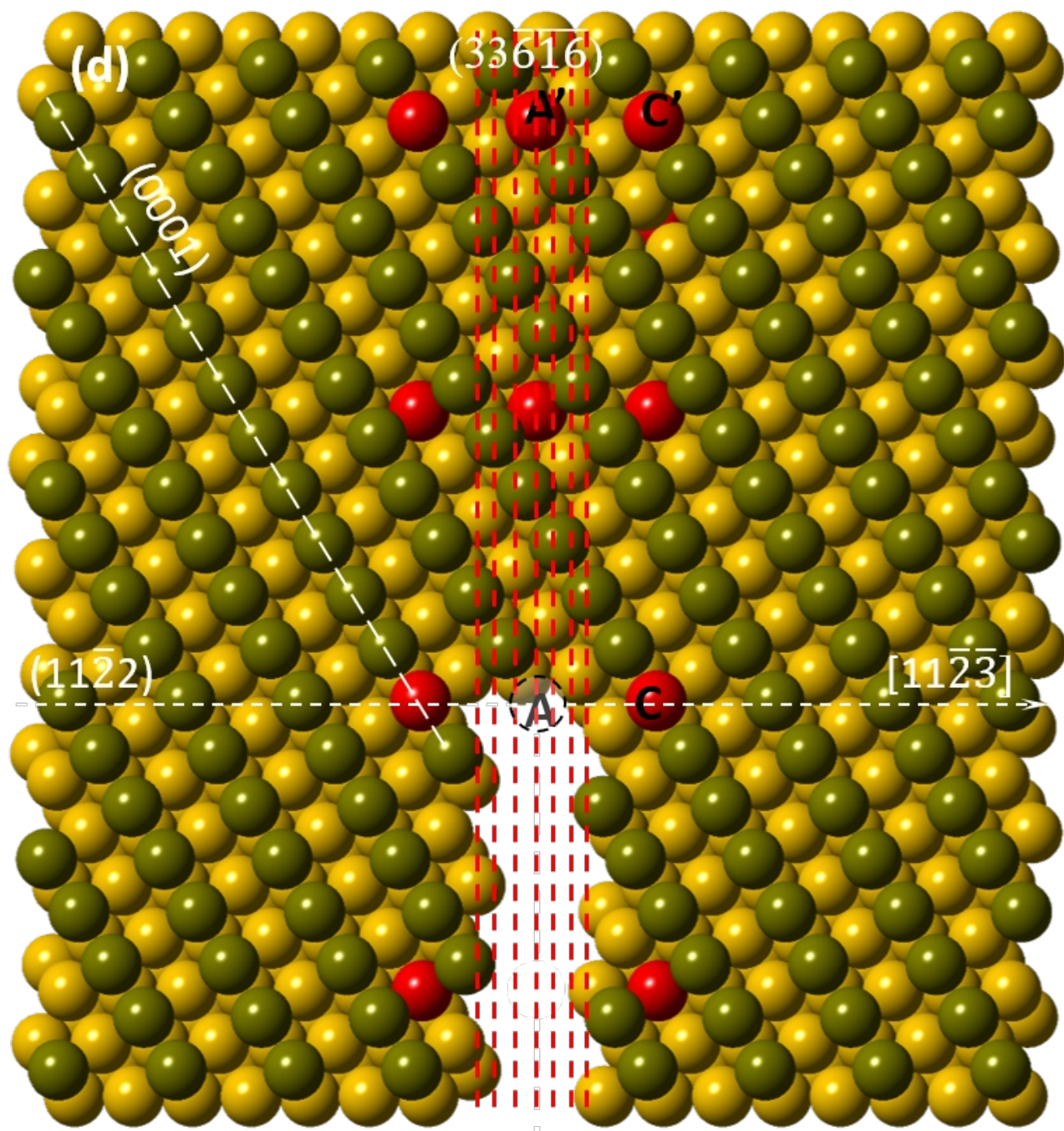
Burgers vector  $\mathbf{b} = \overline{AC} = 1/3[11\bar{2}\bar{3}]$

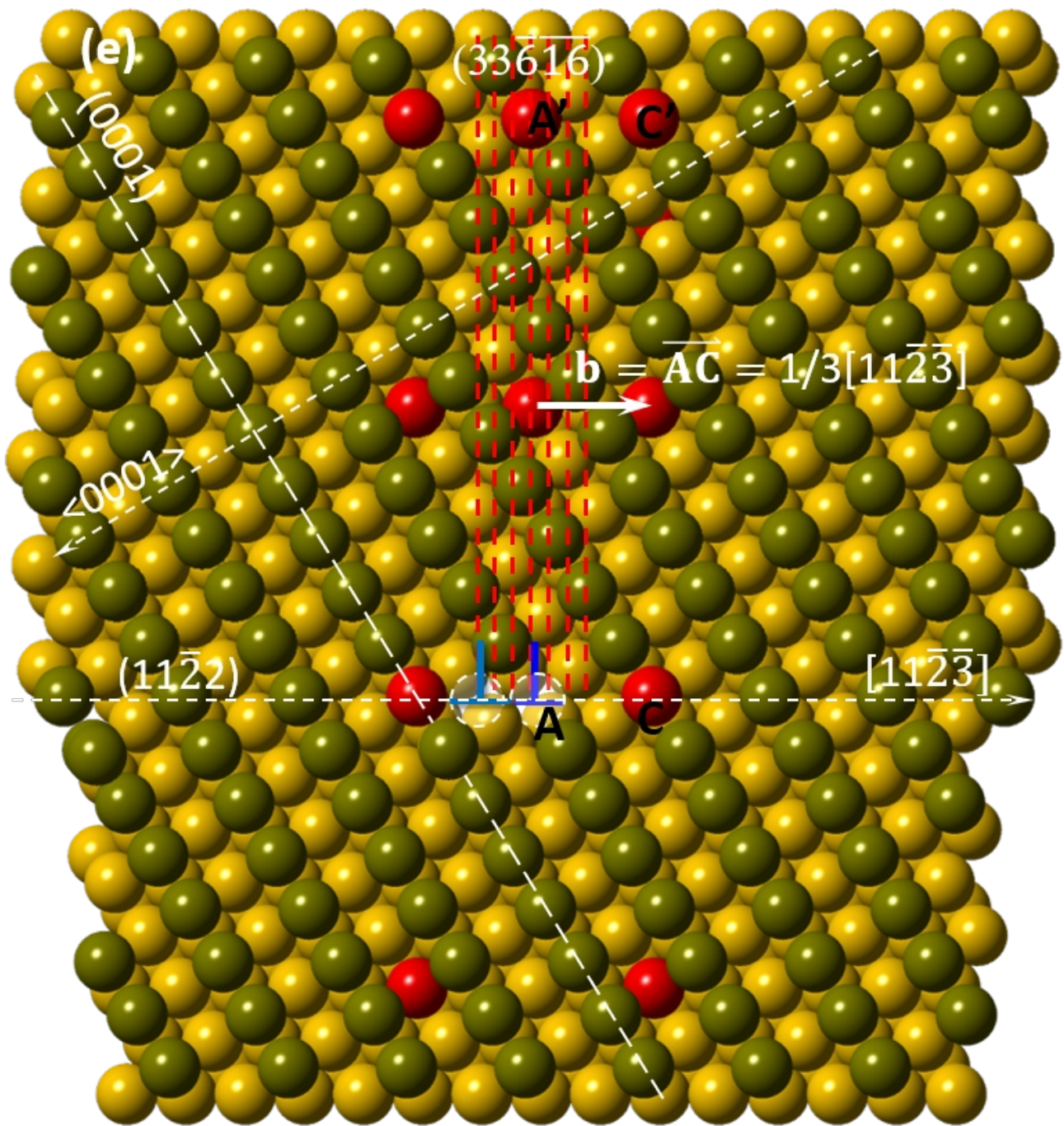


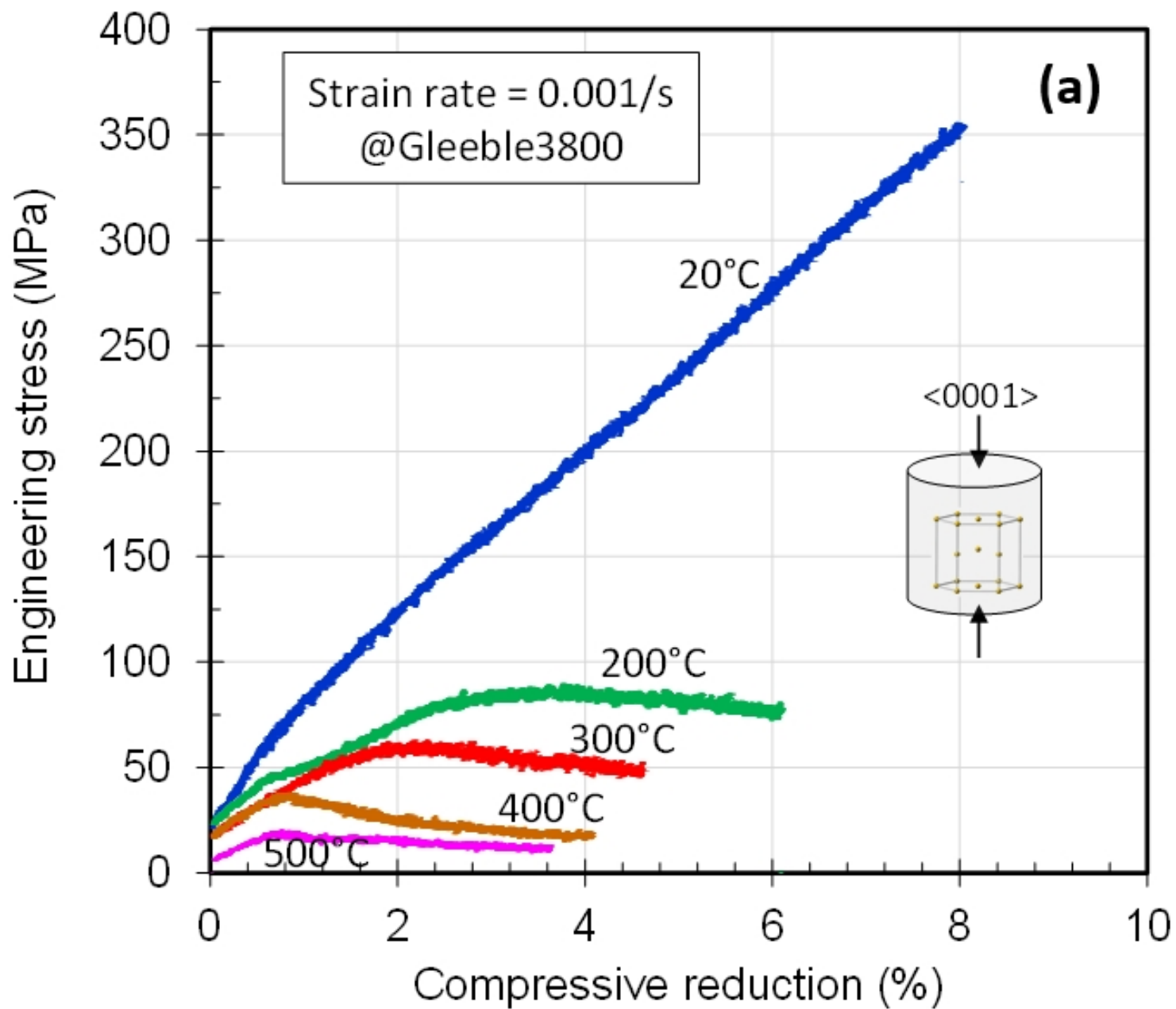




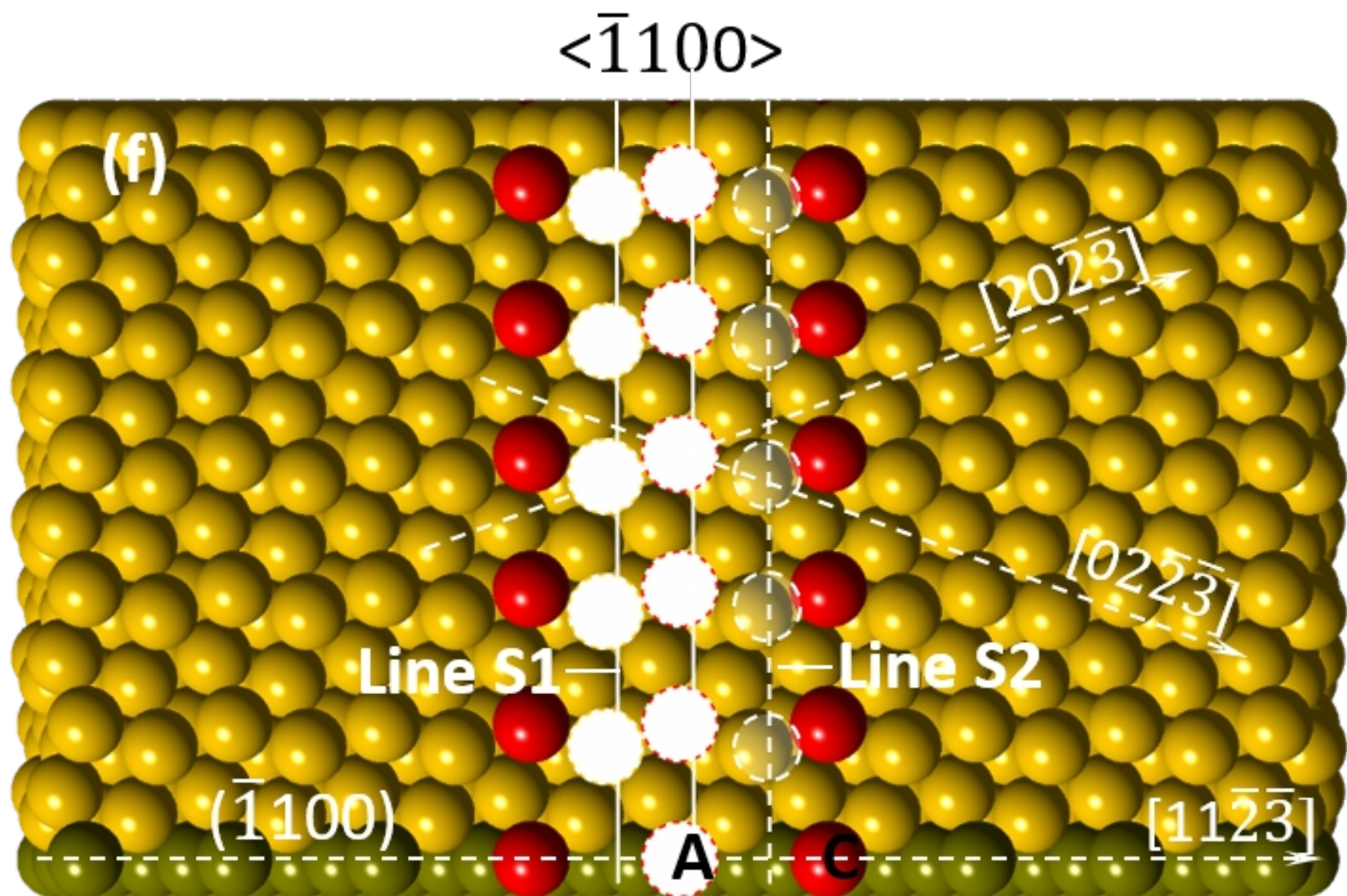


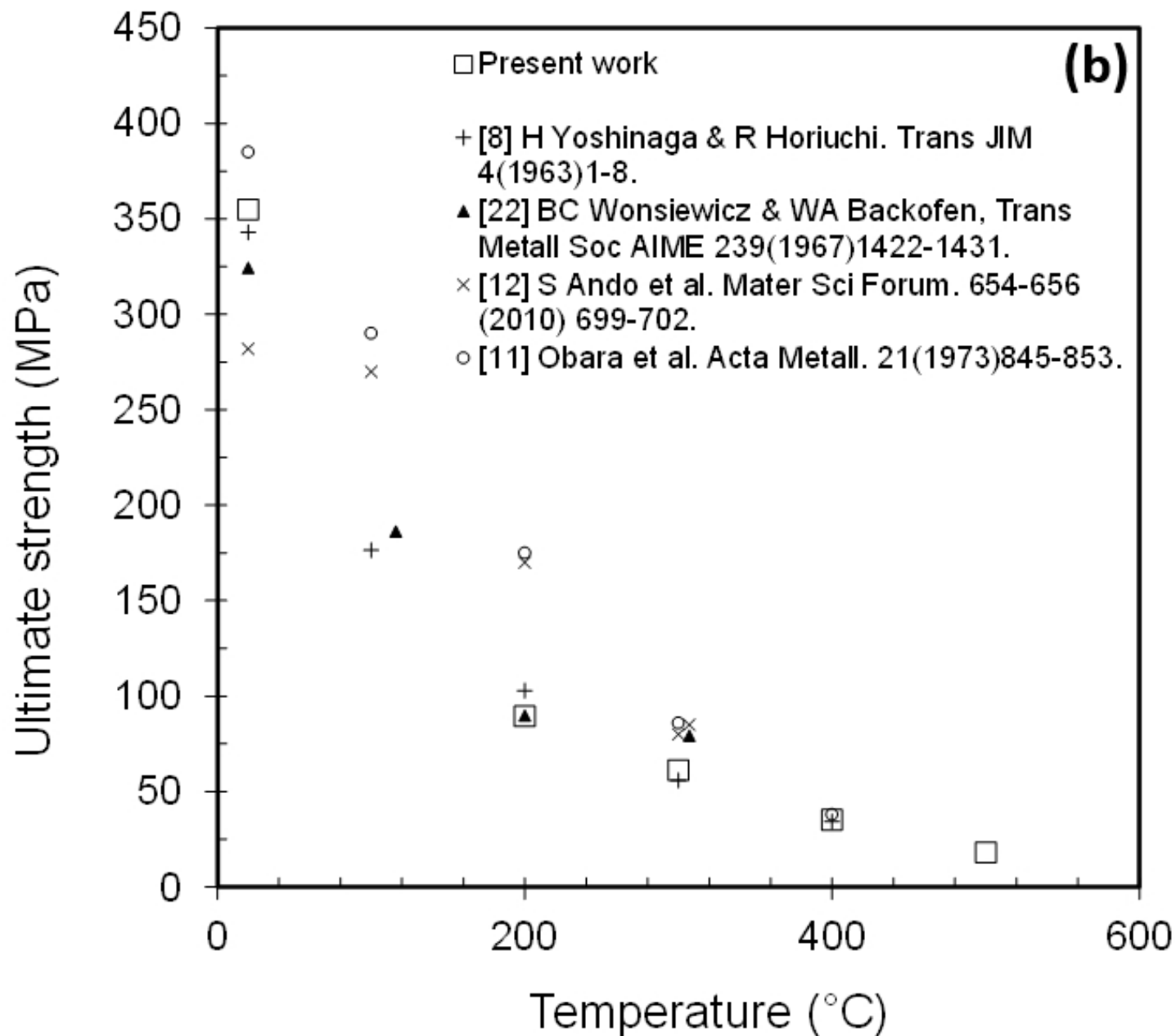


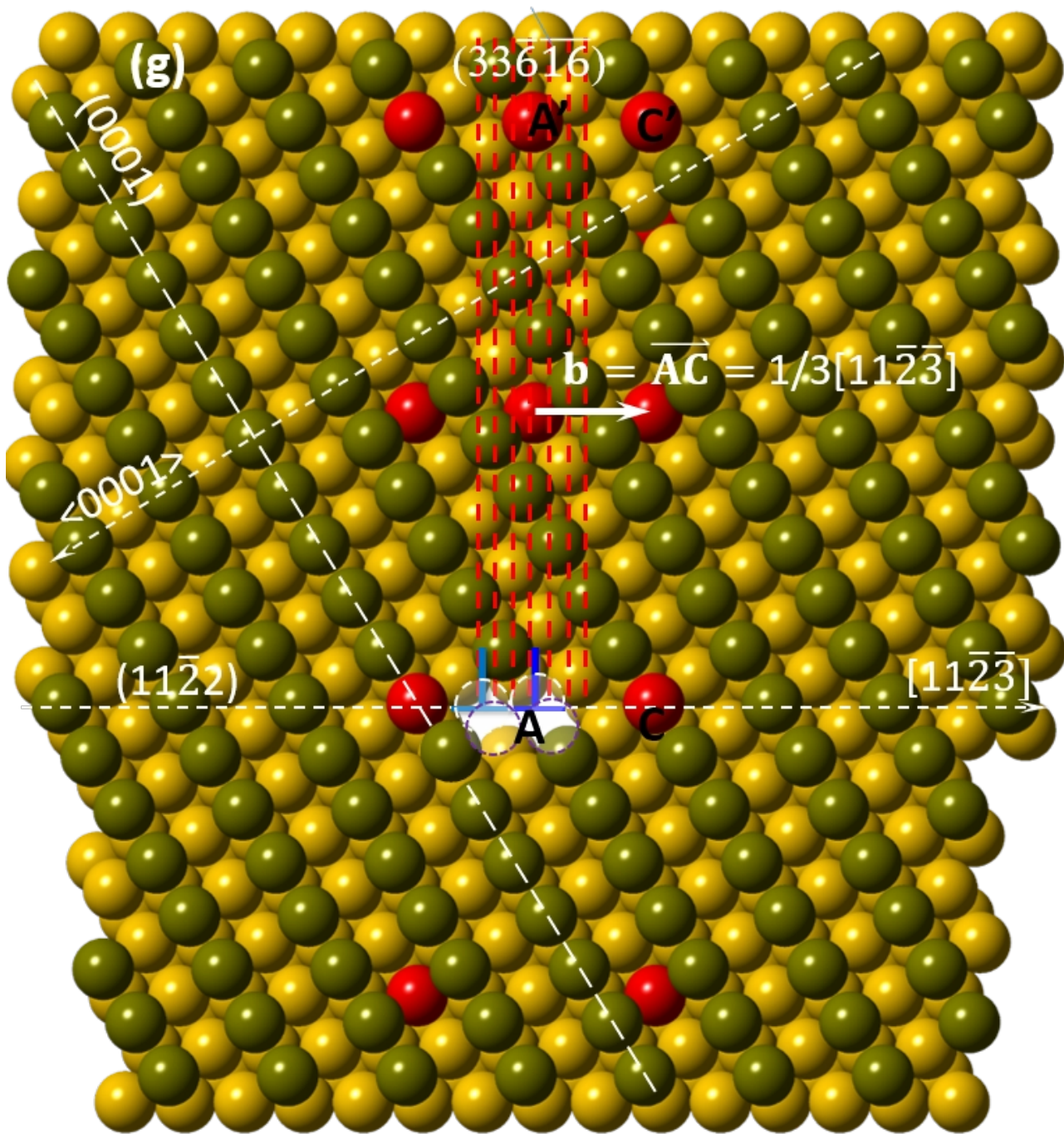




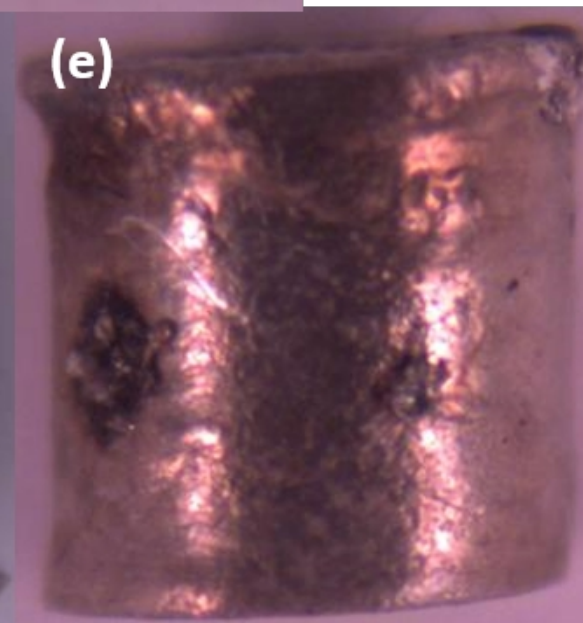
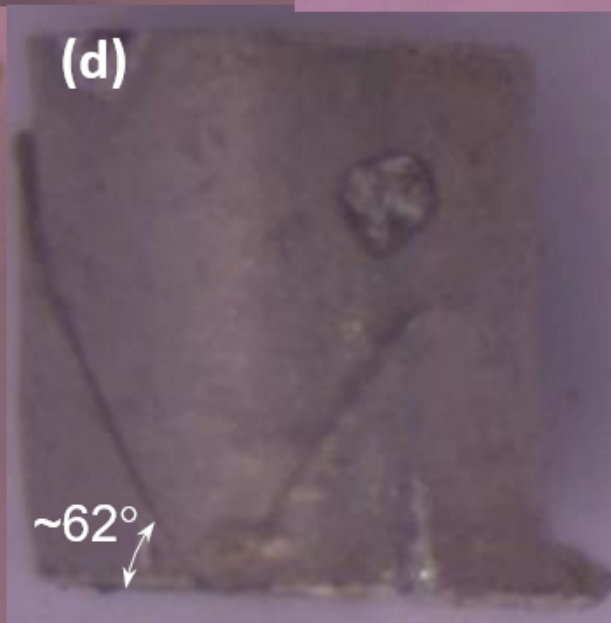
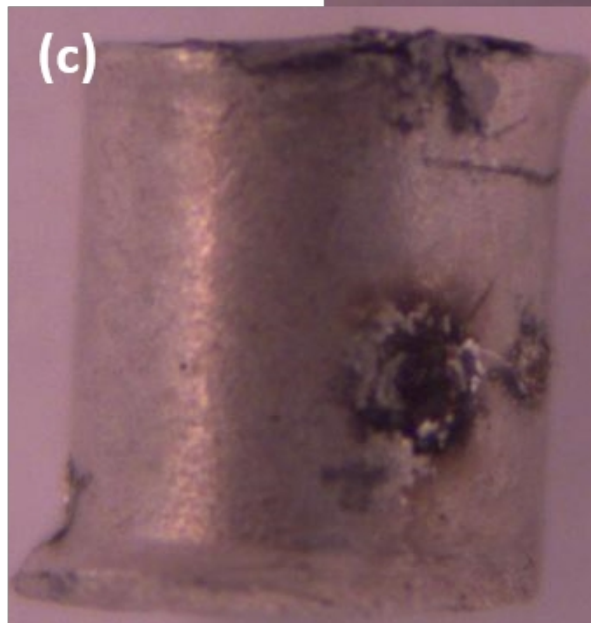
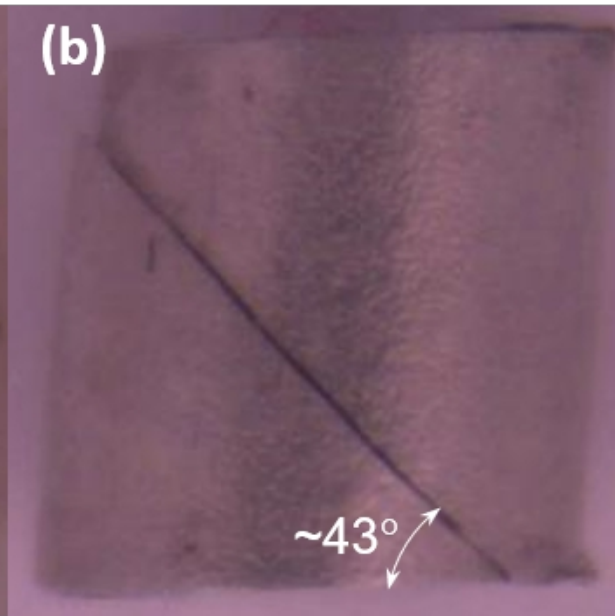
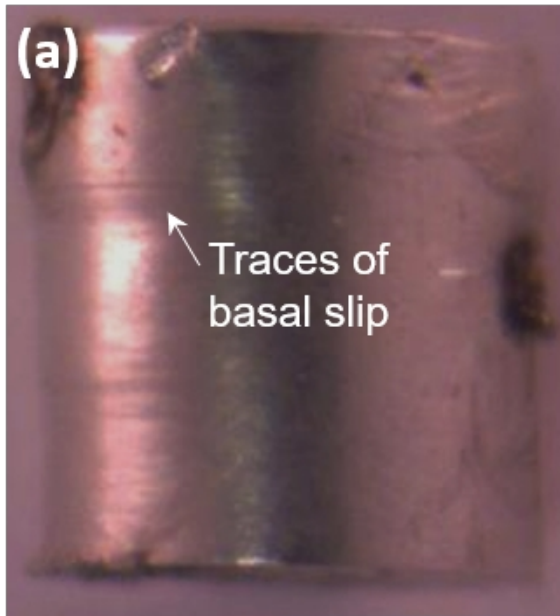


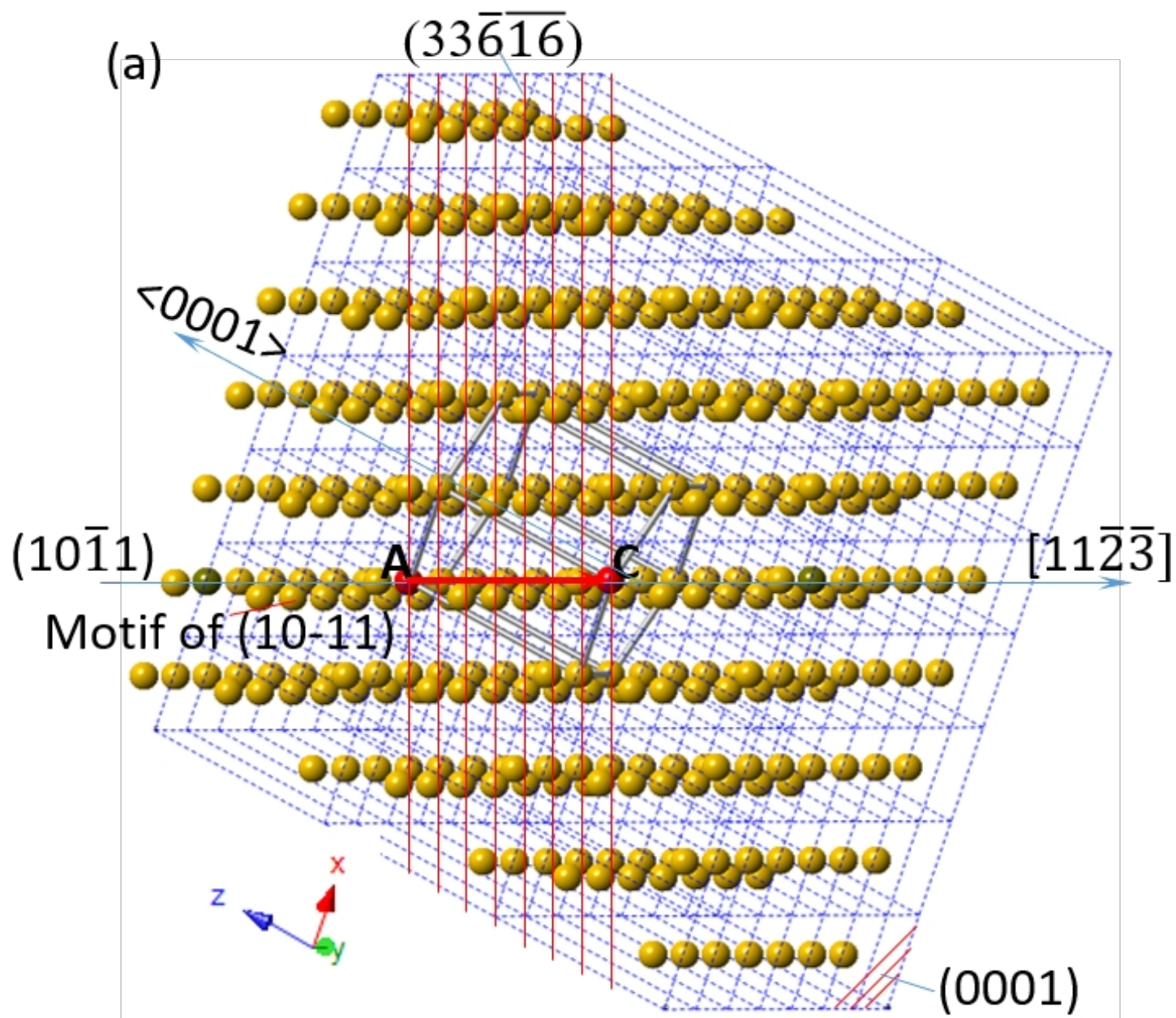




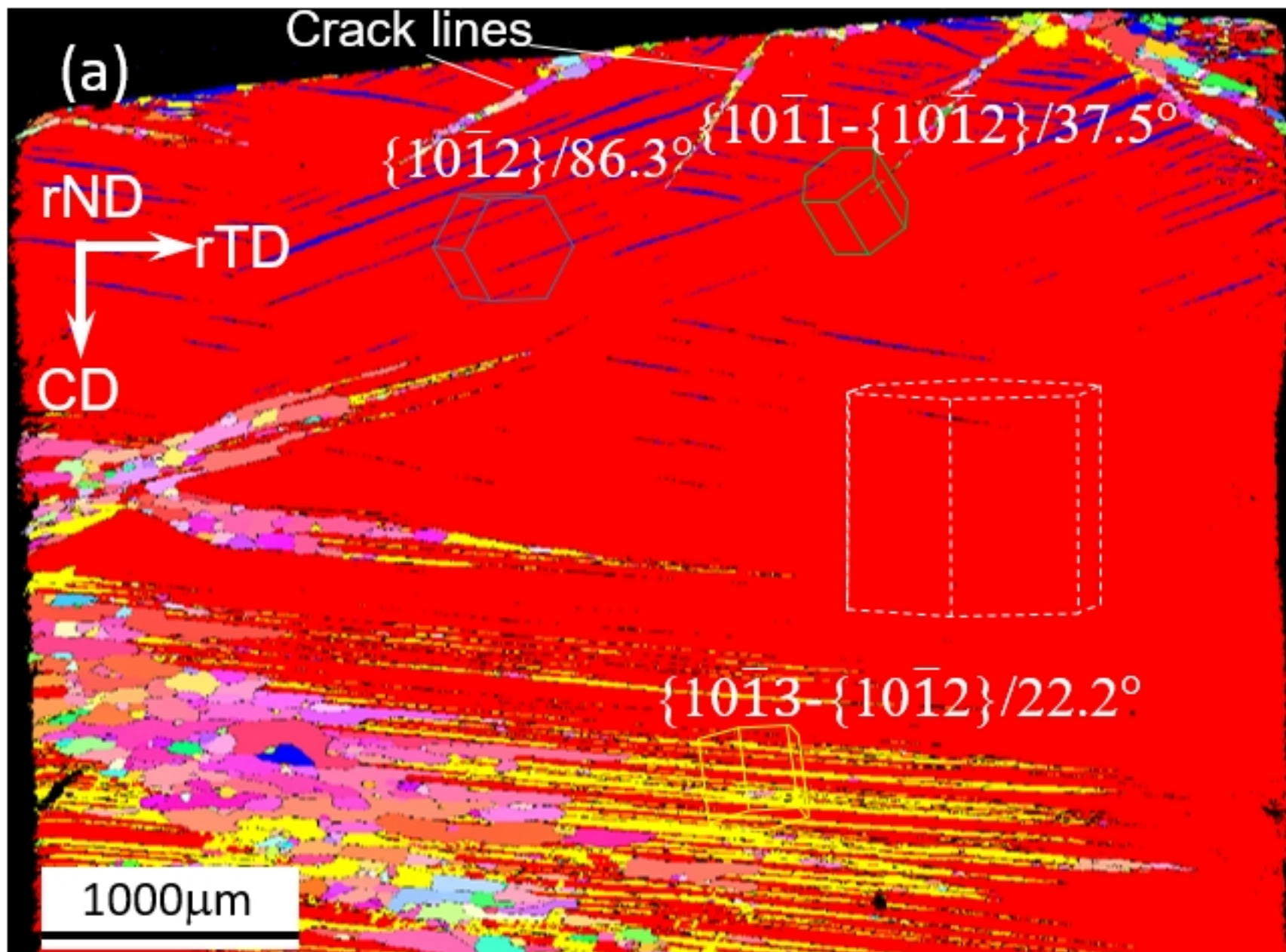


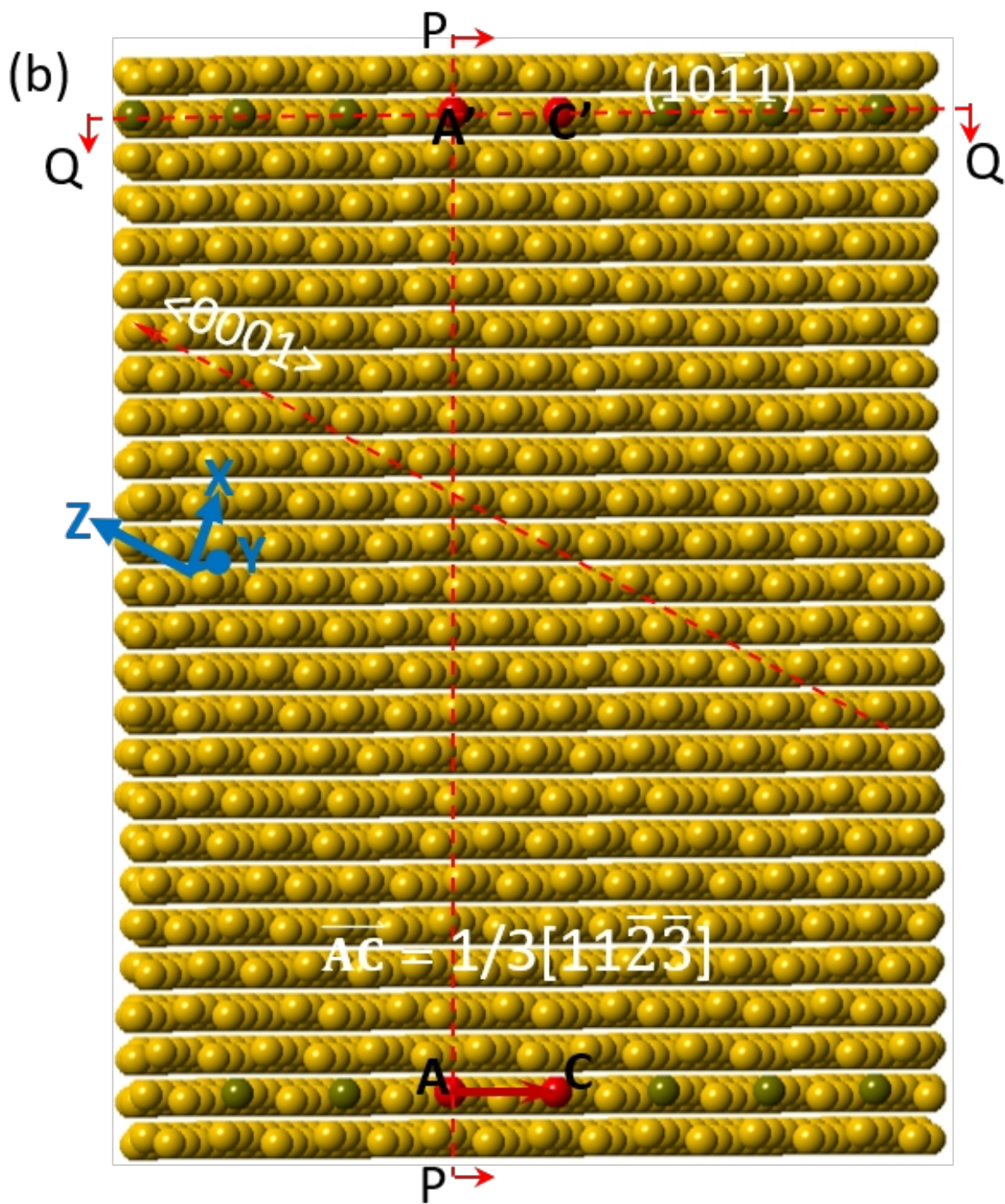


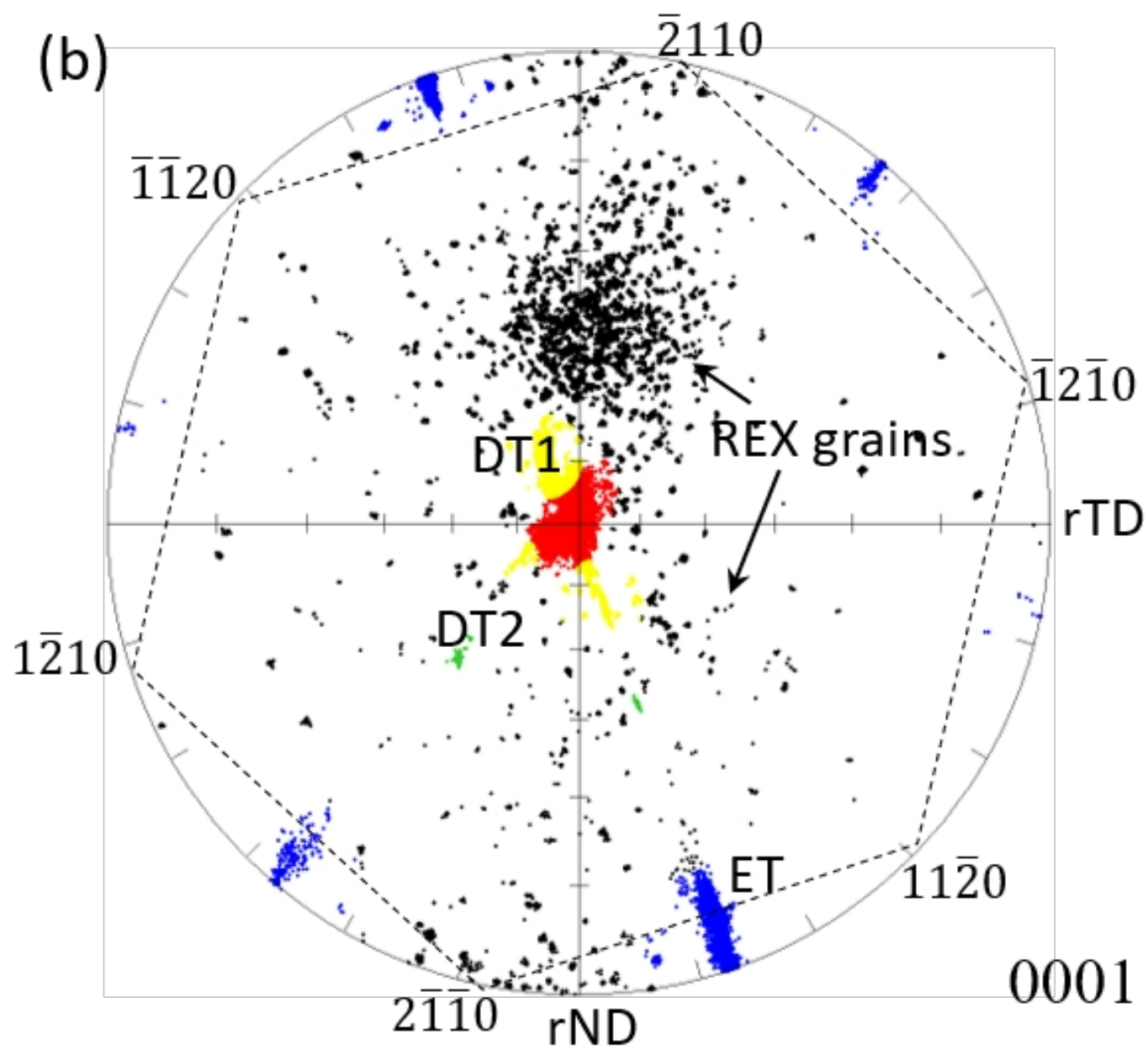








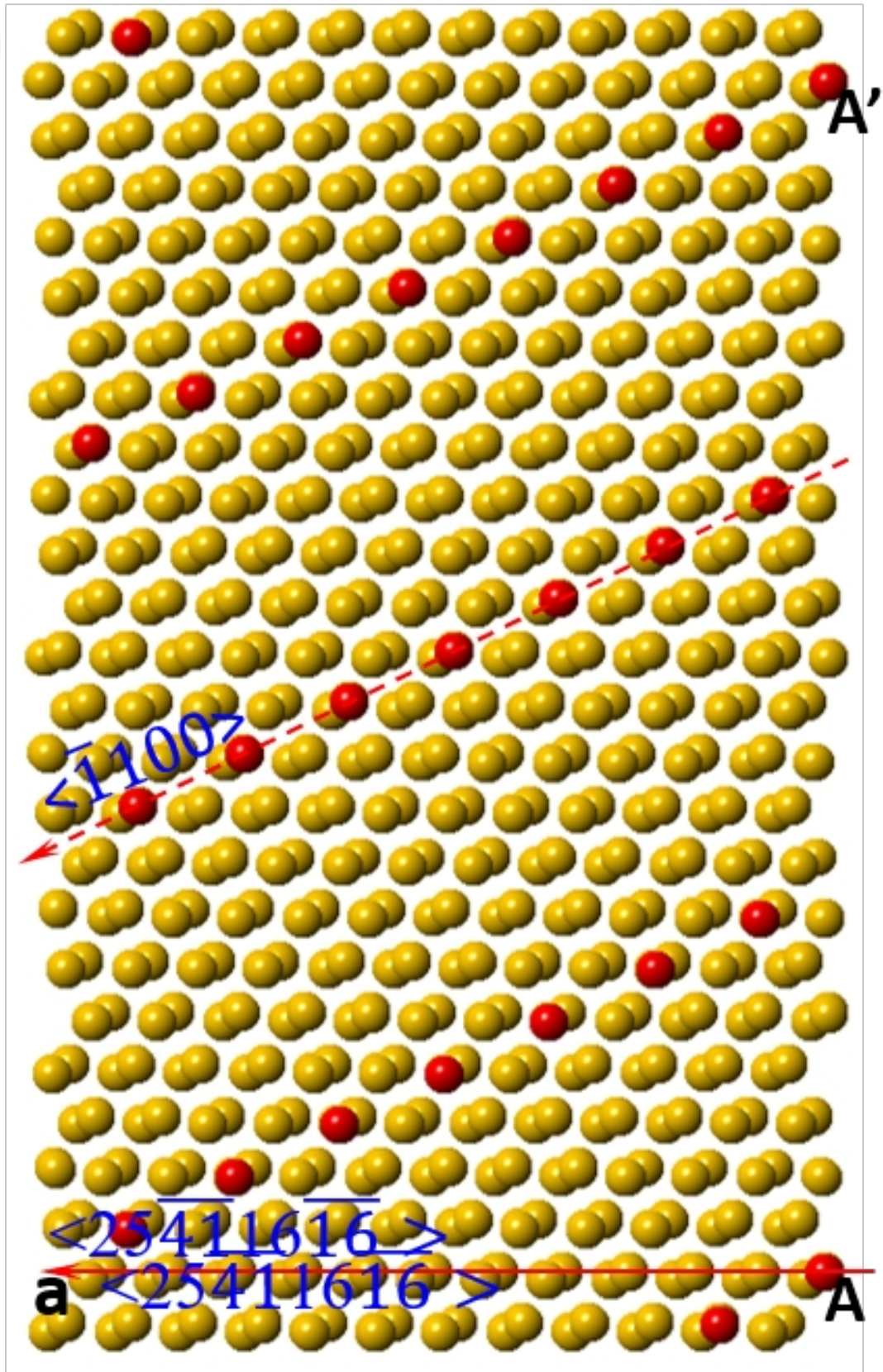


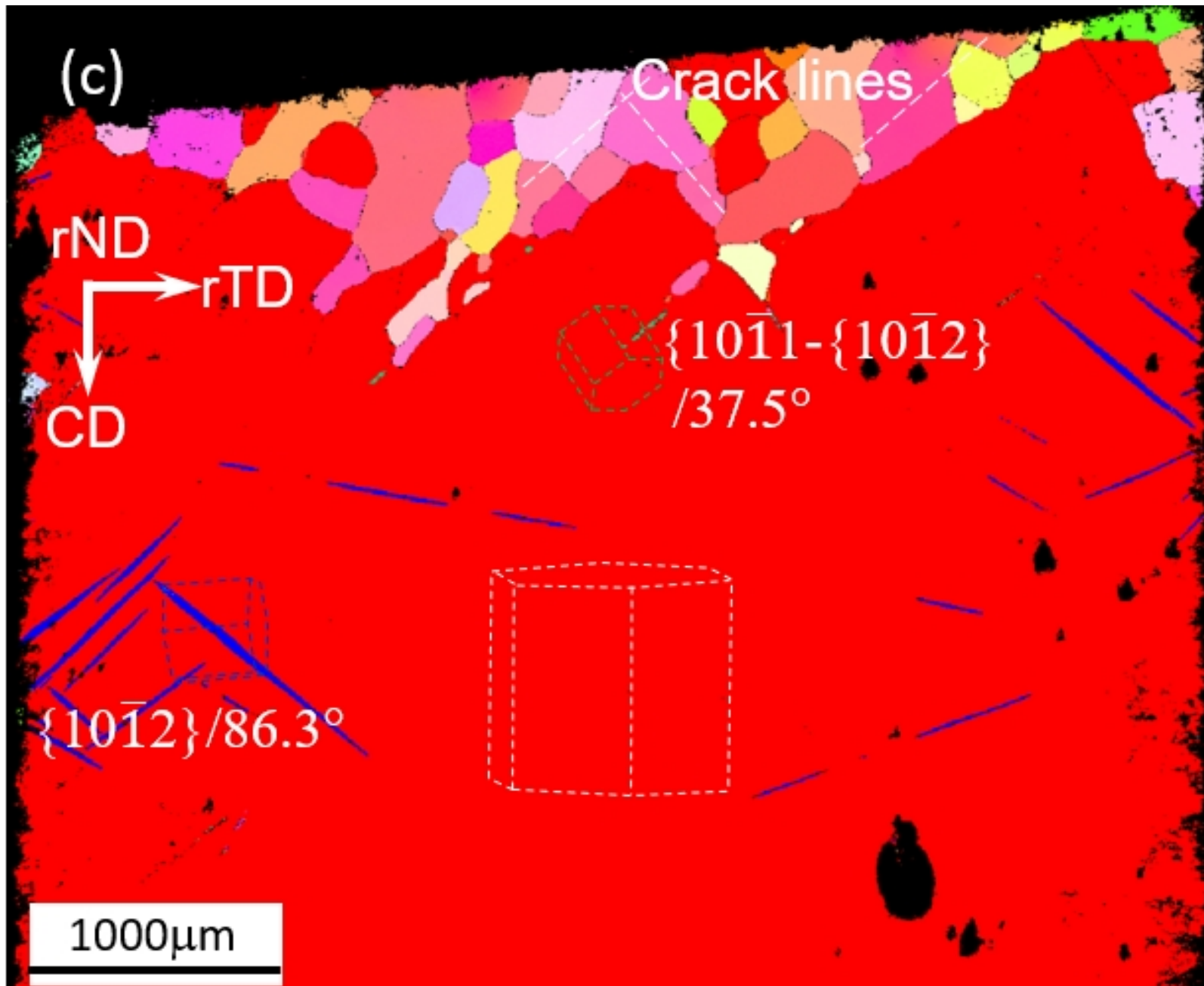




P-P view

(c)

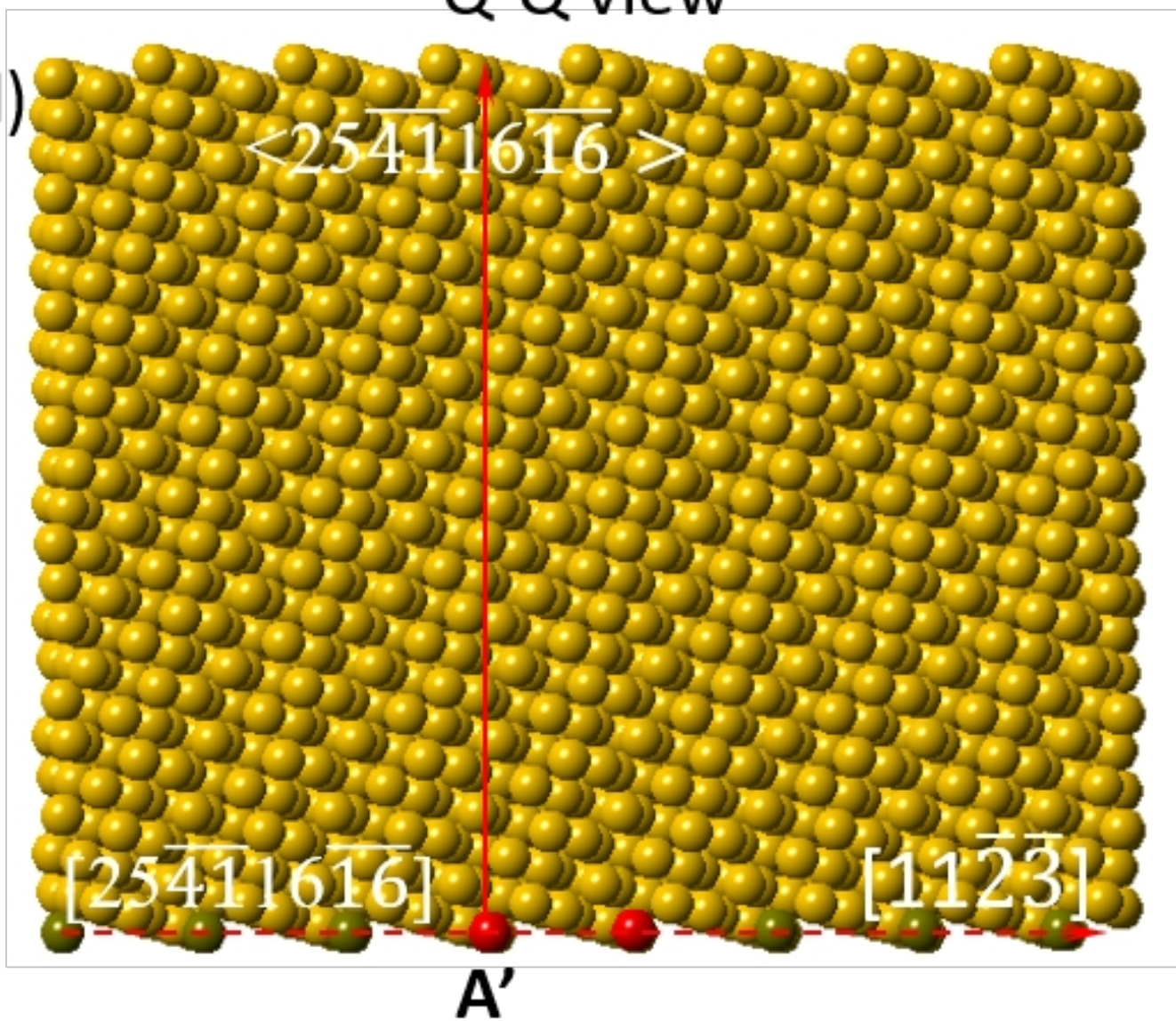


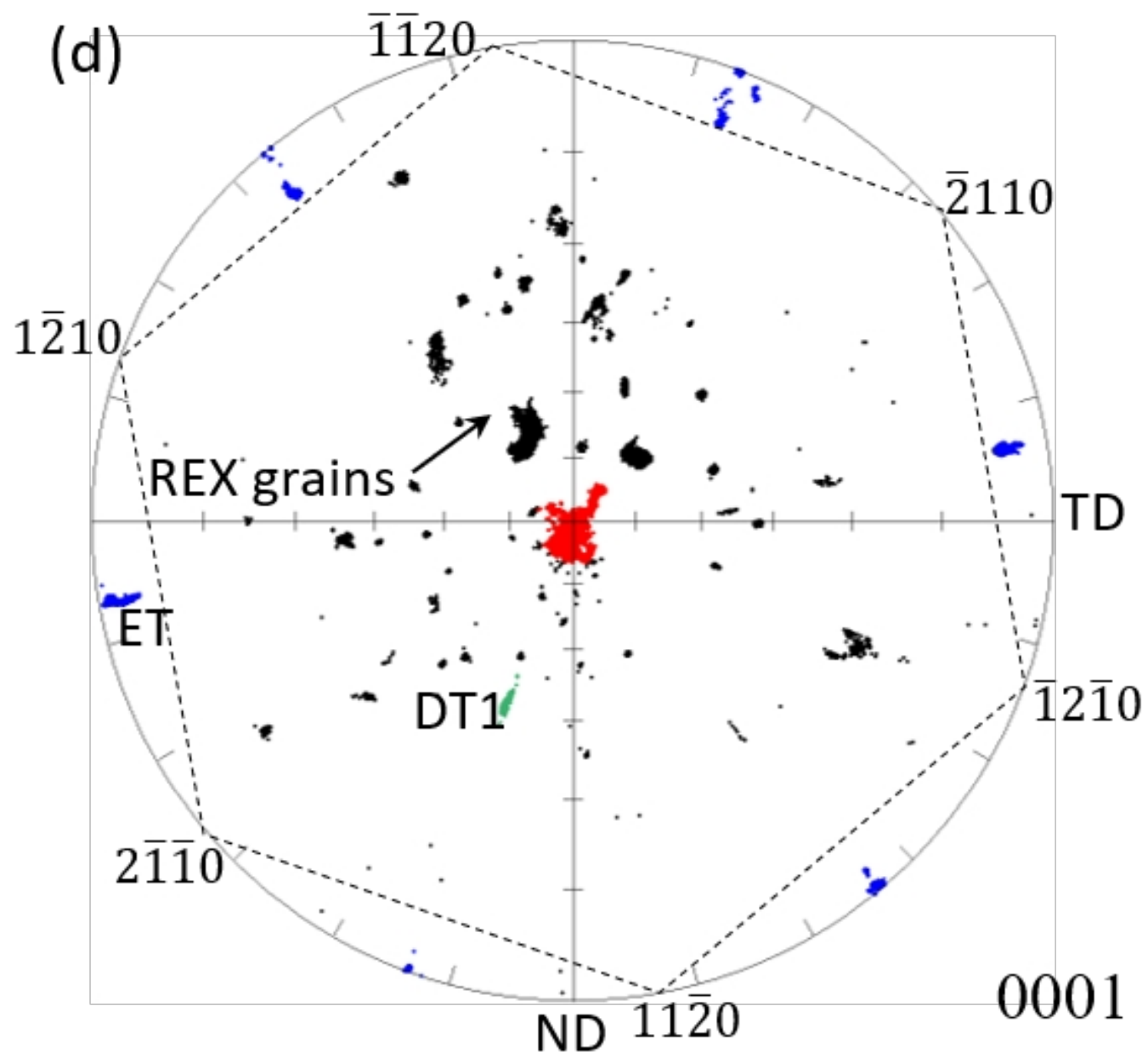


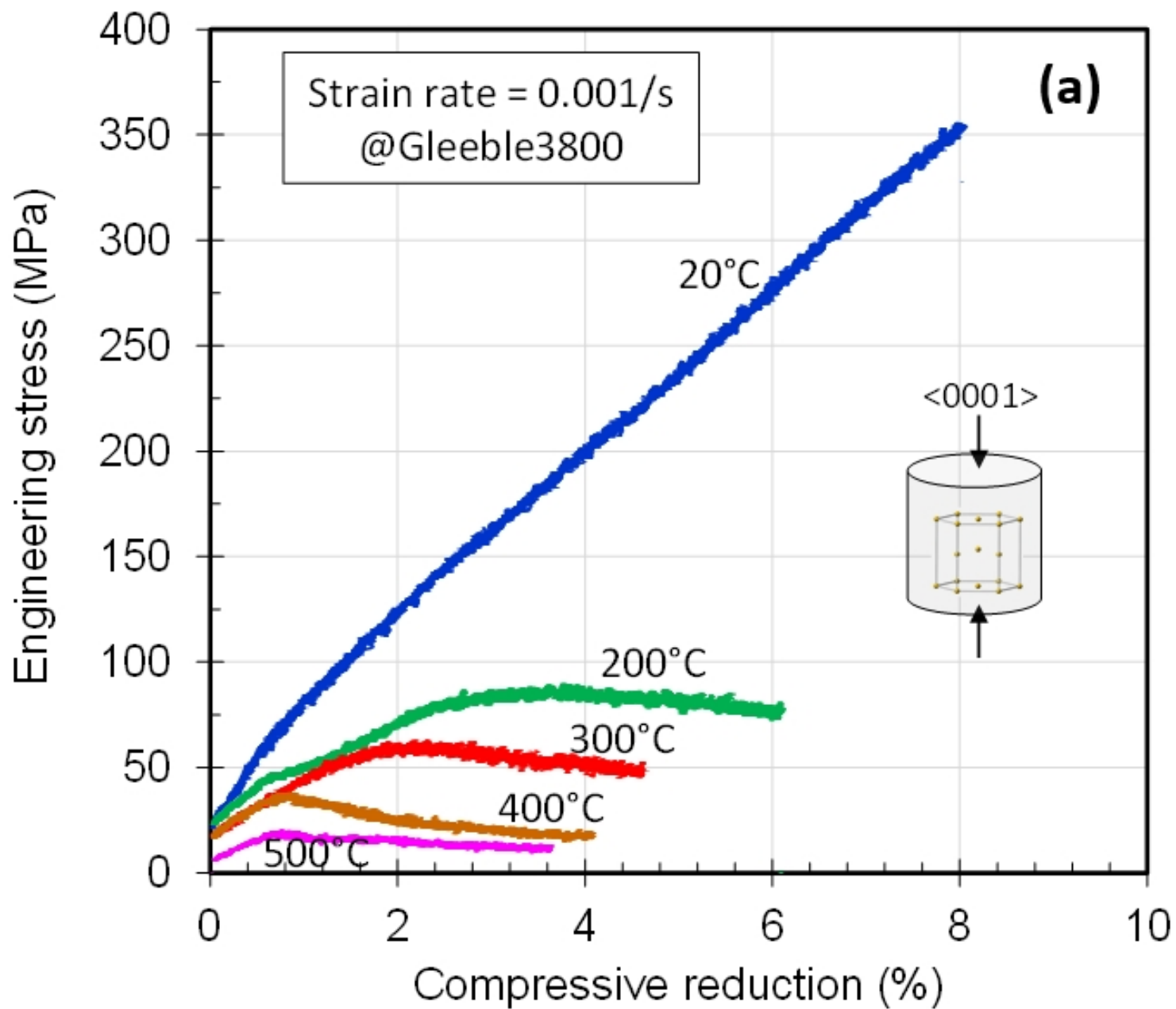


Q-Q view

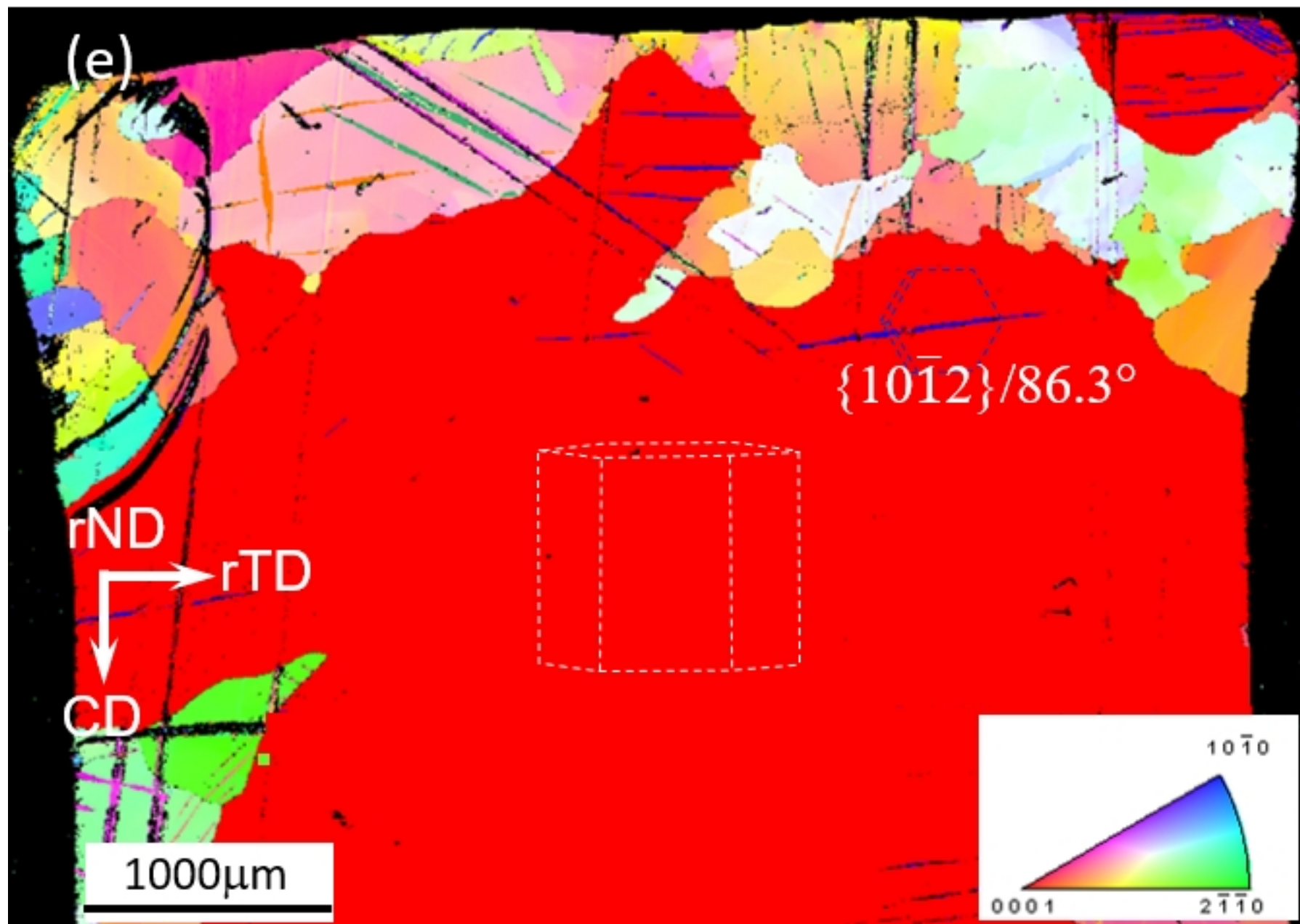
(d)

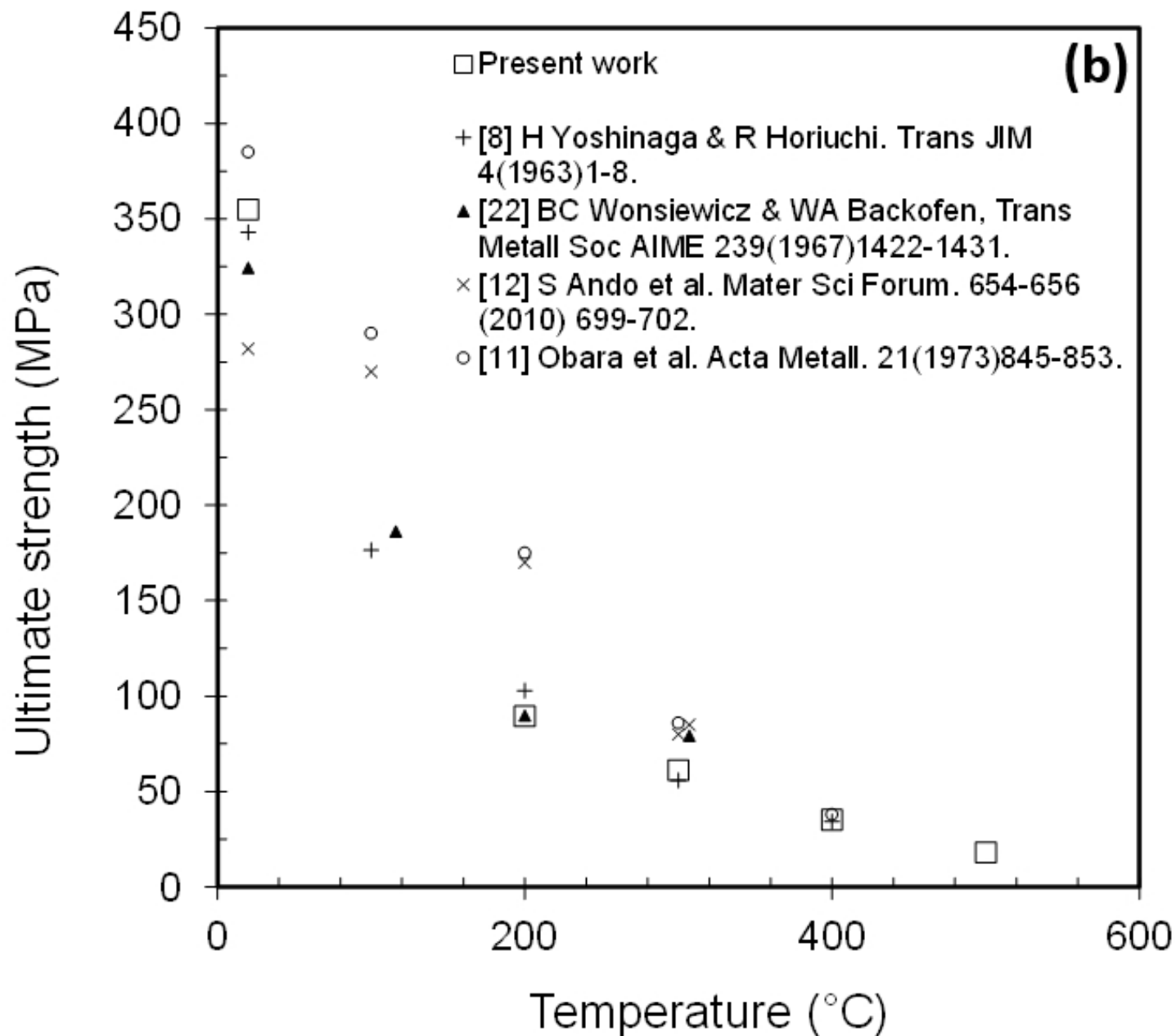


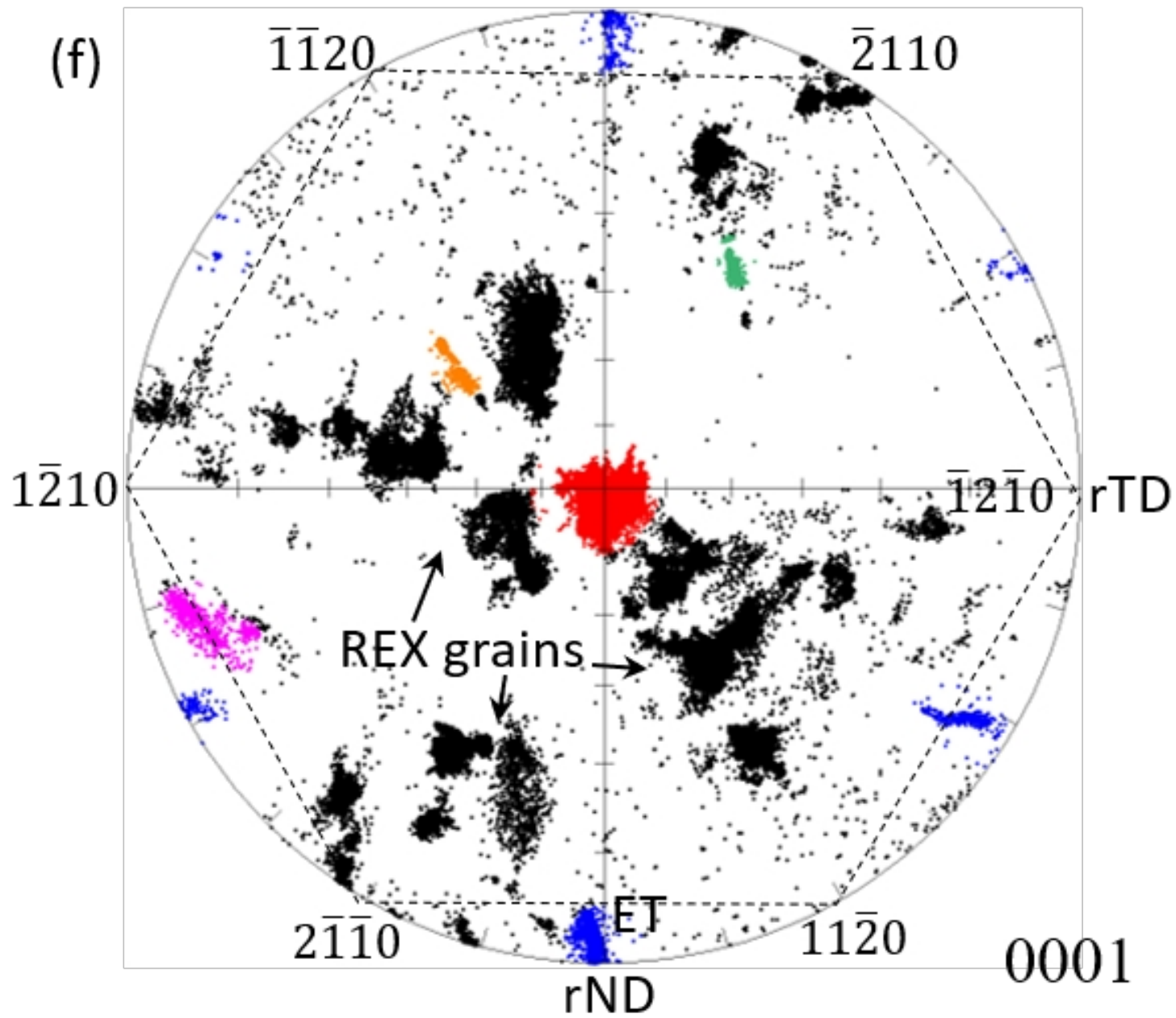


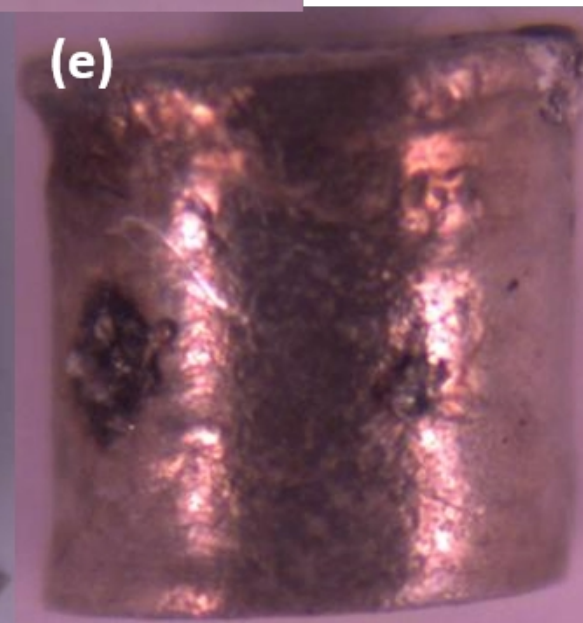
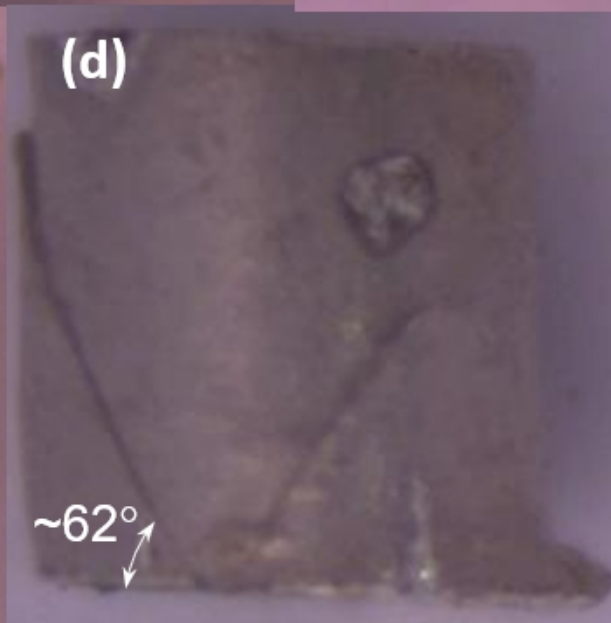
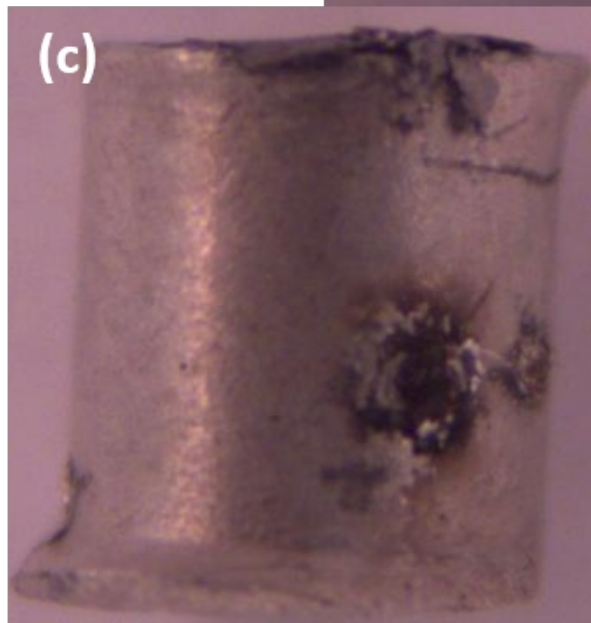
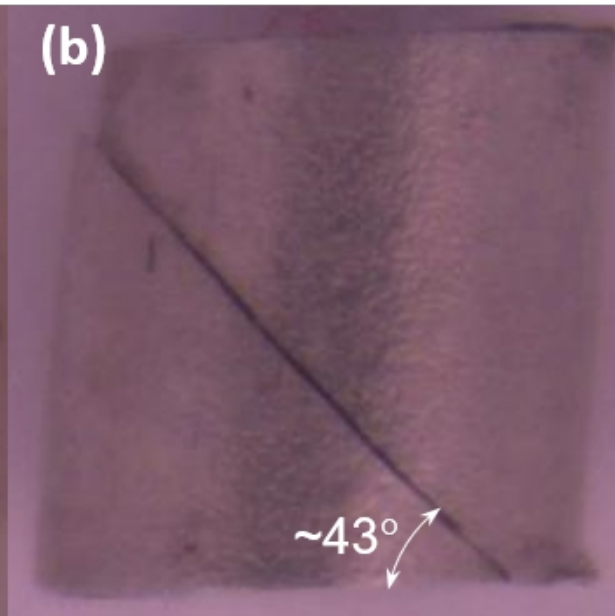
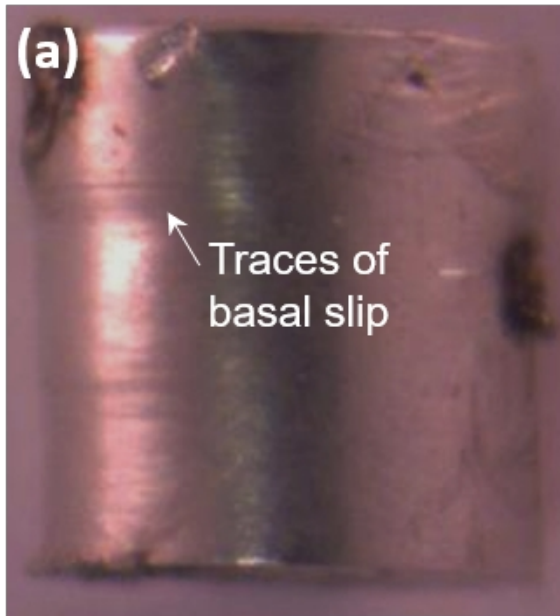








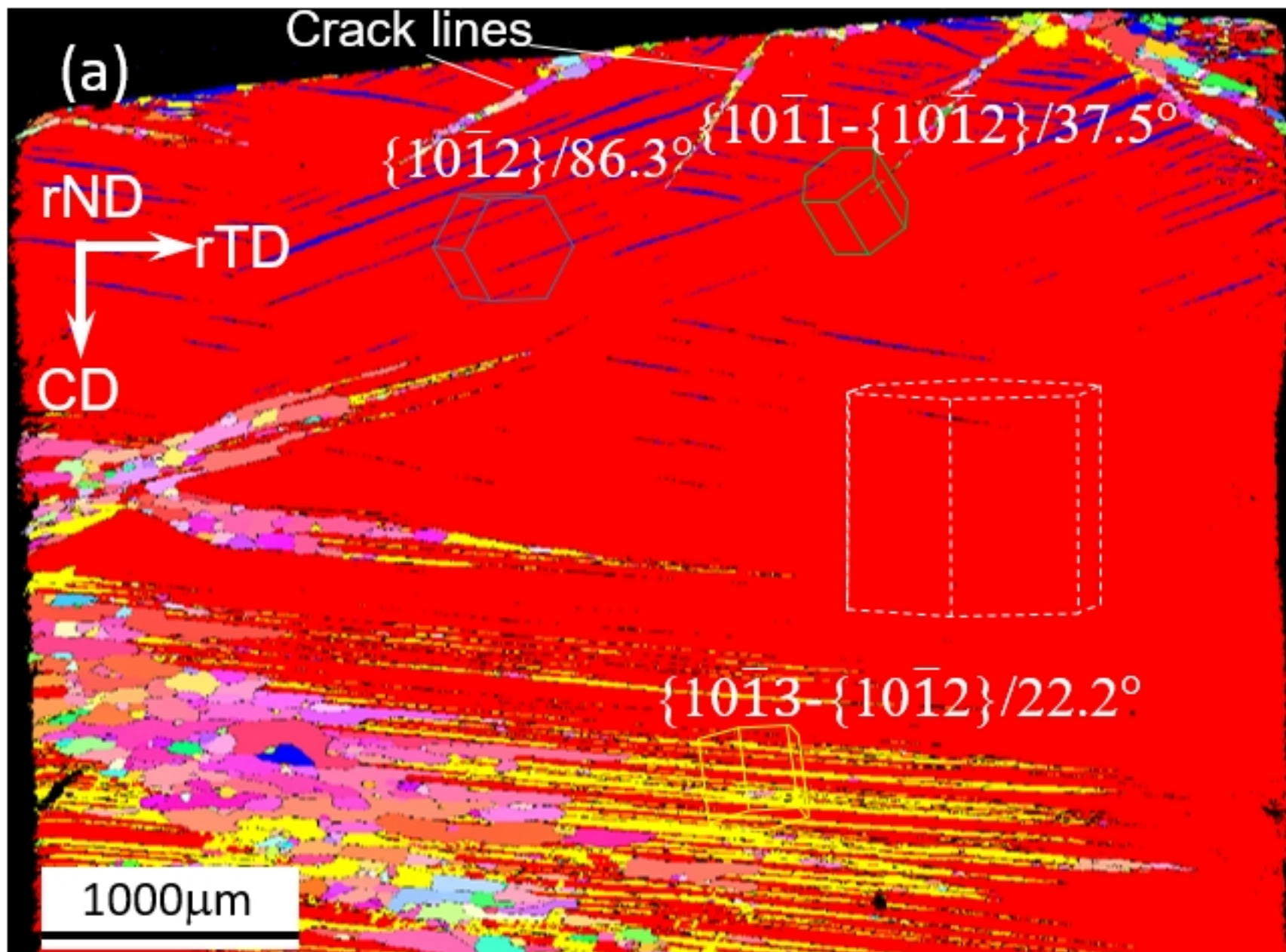


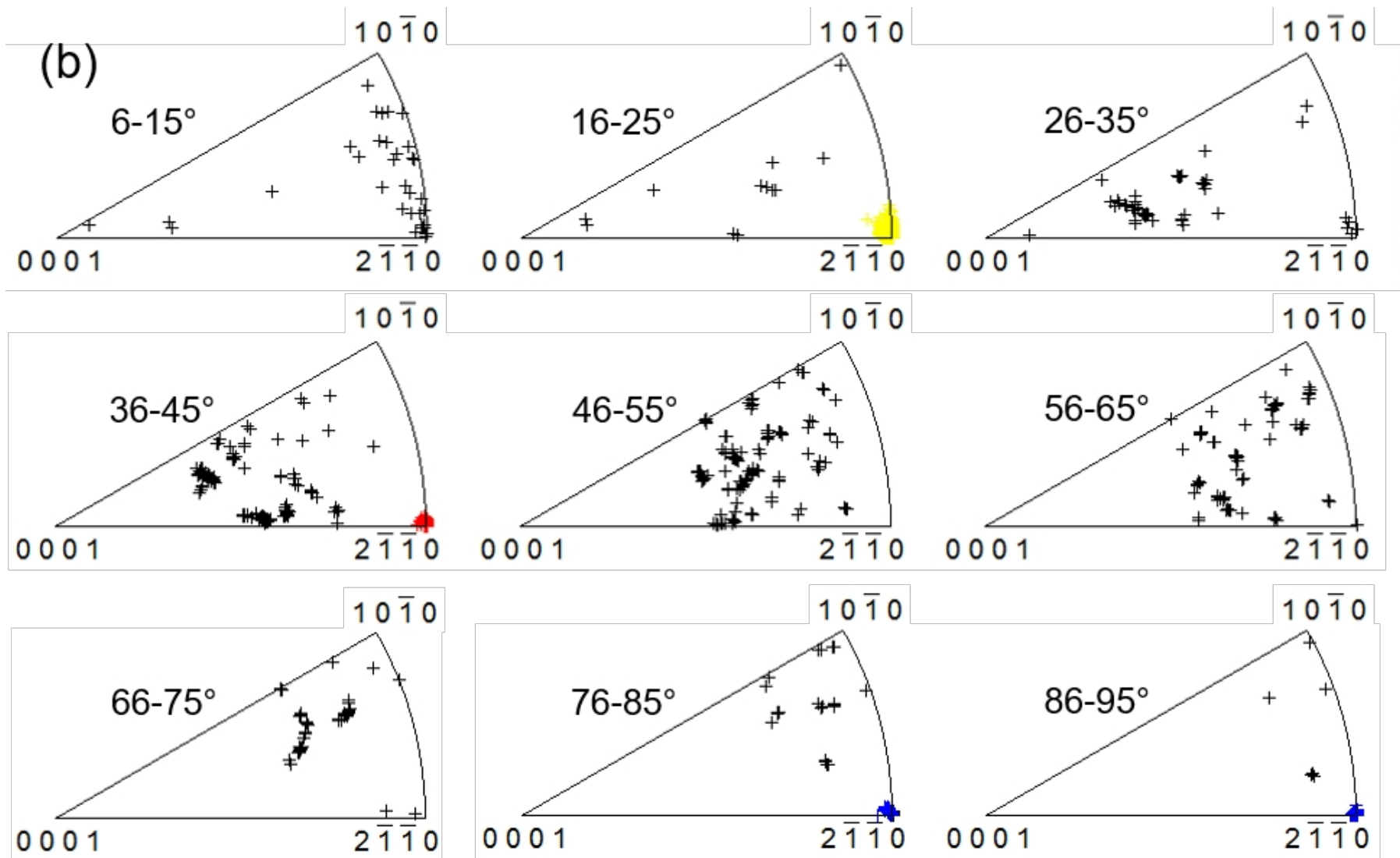


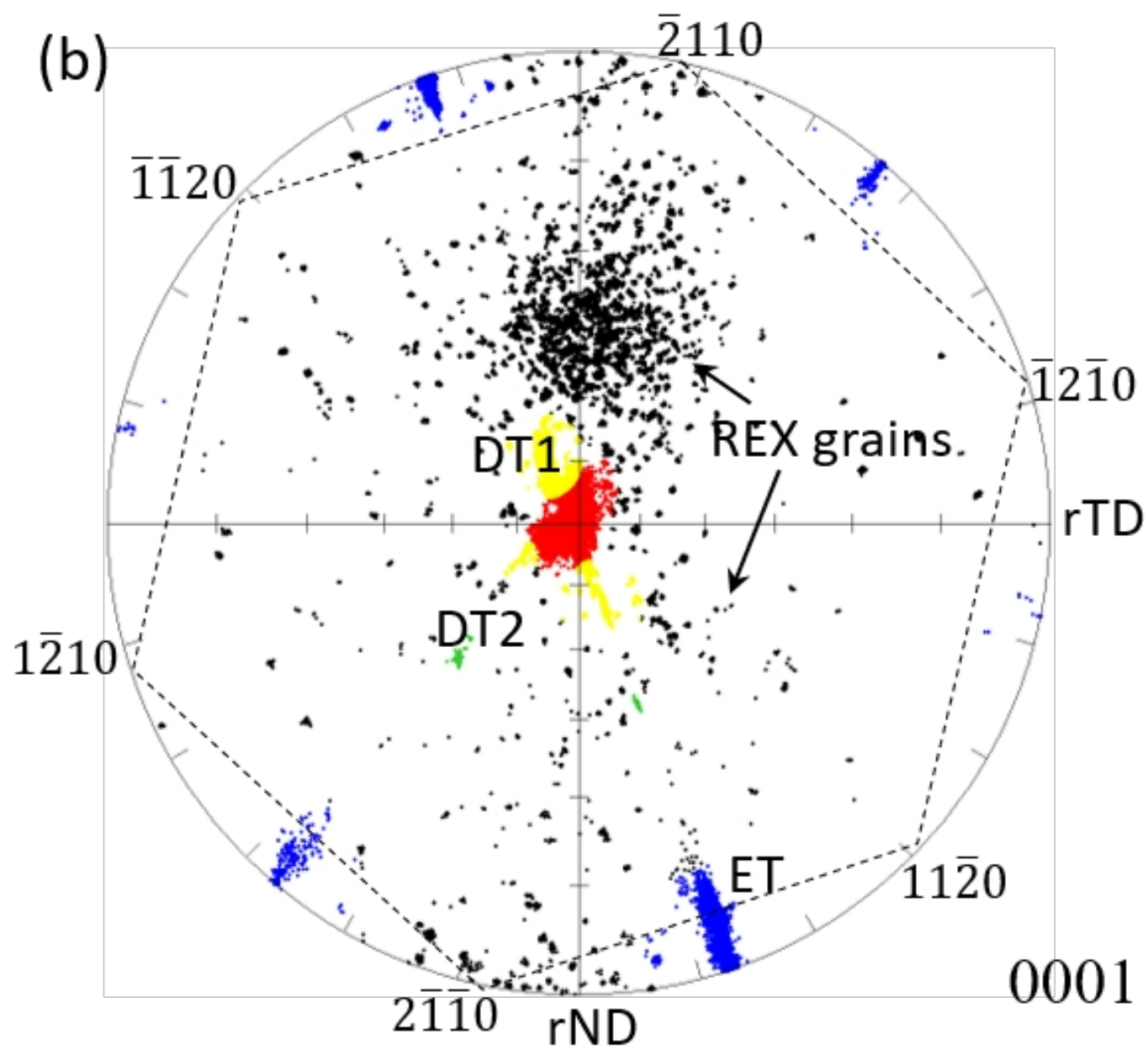


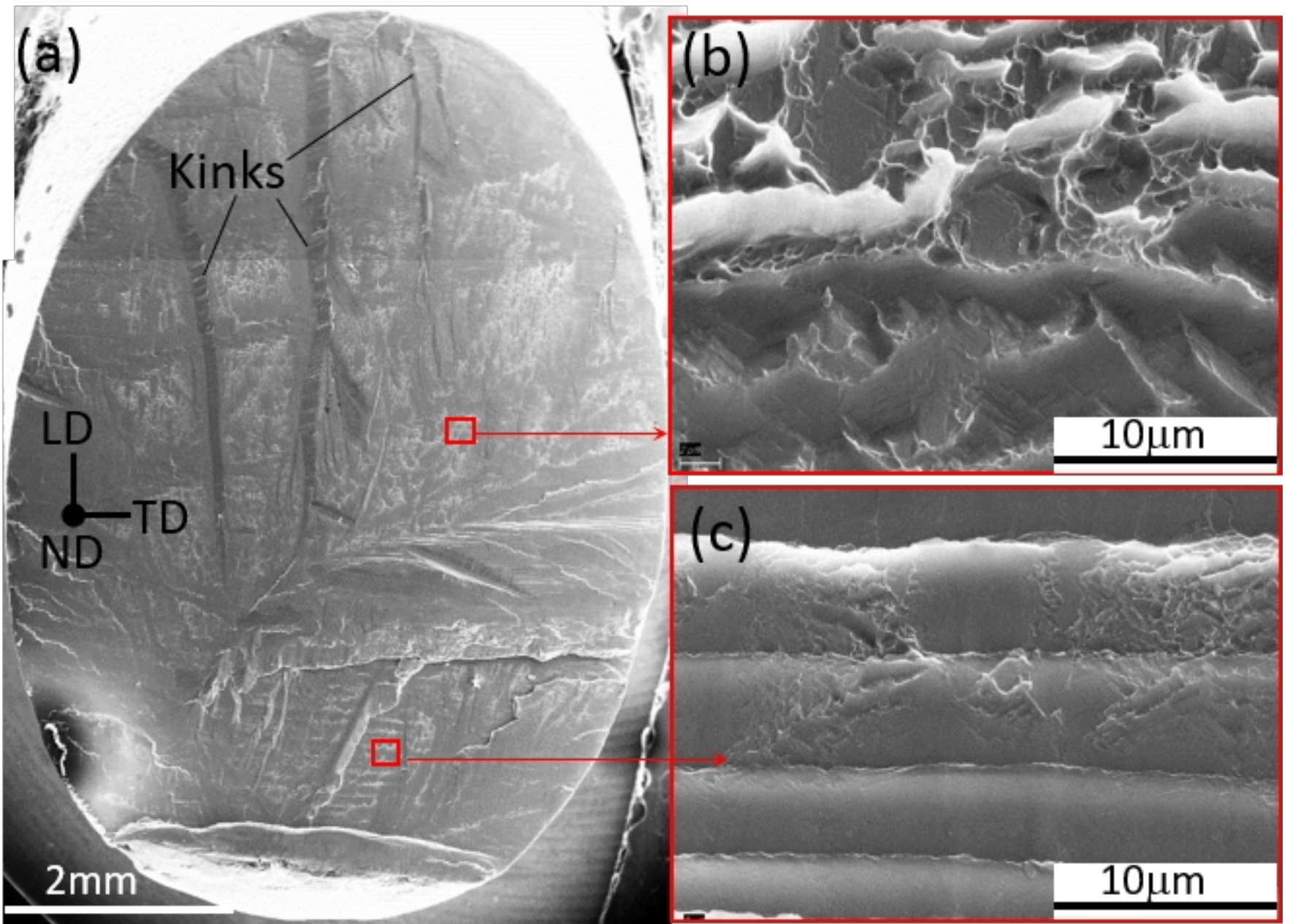




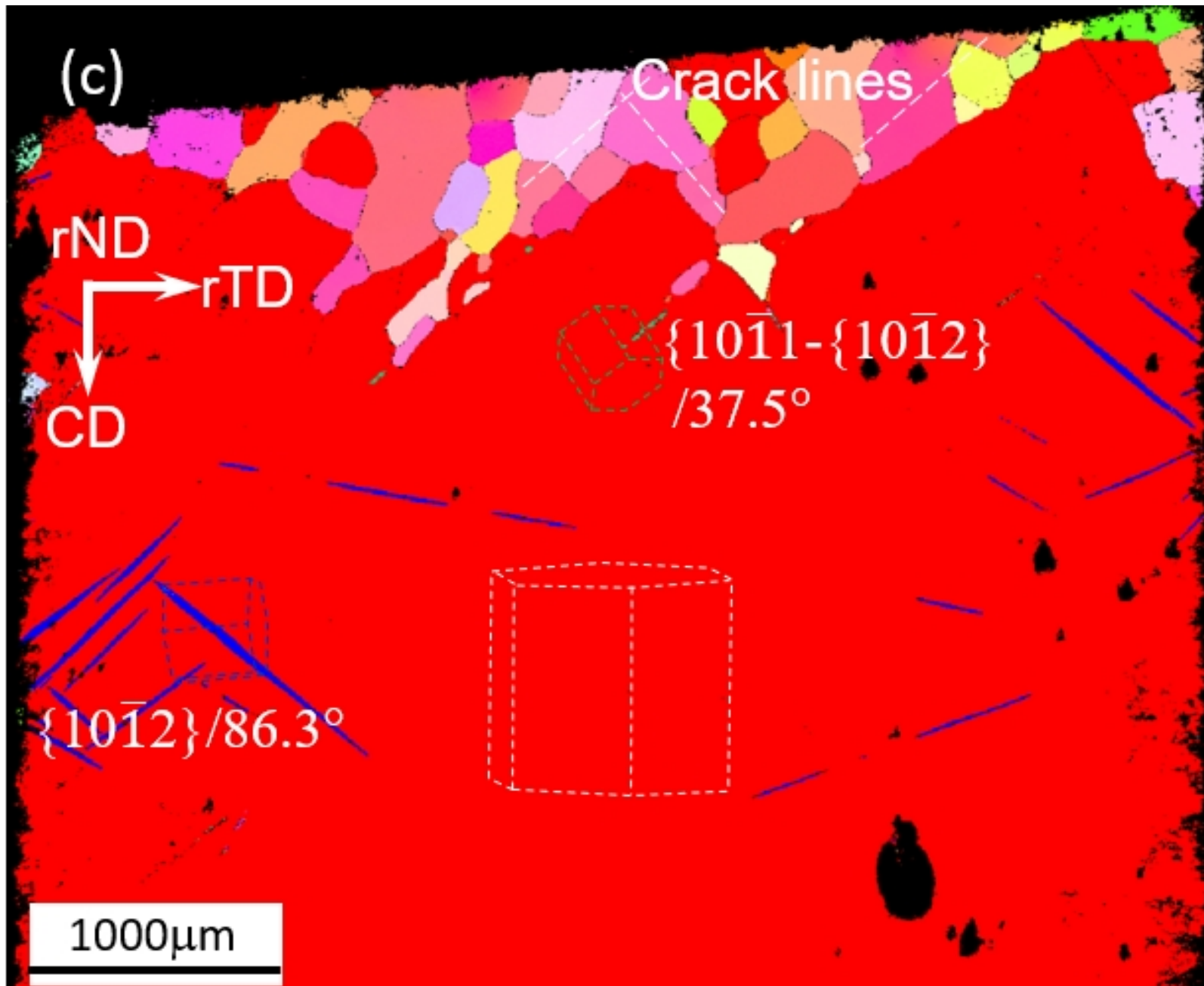




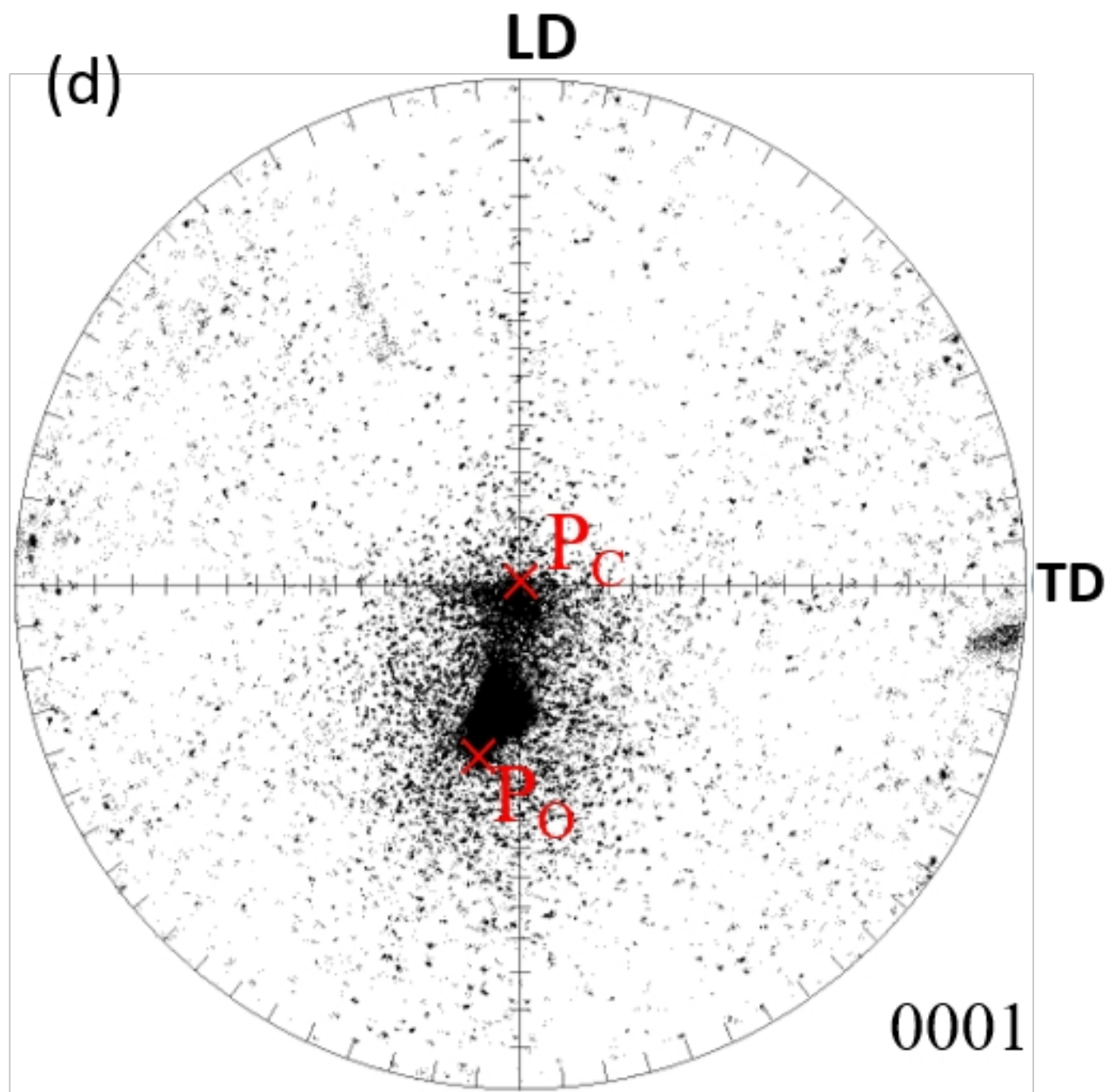


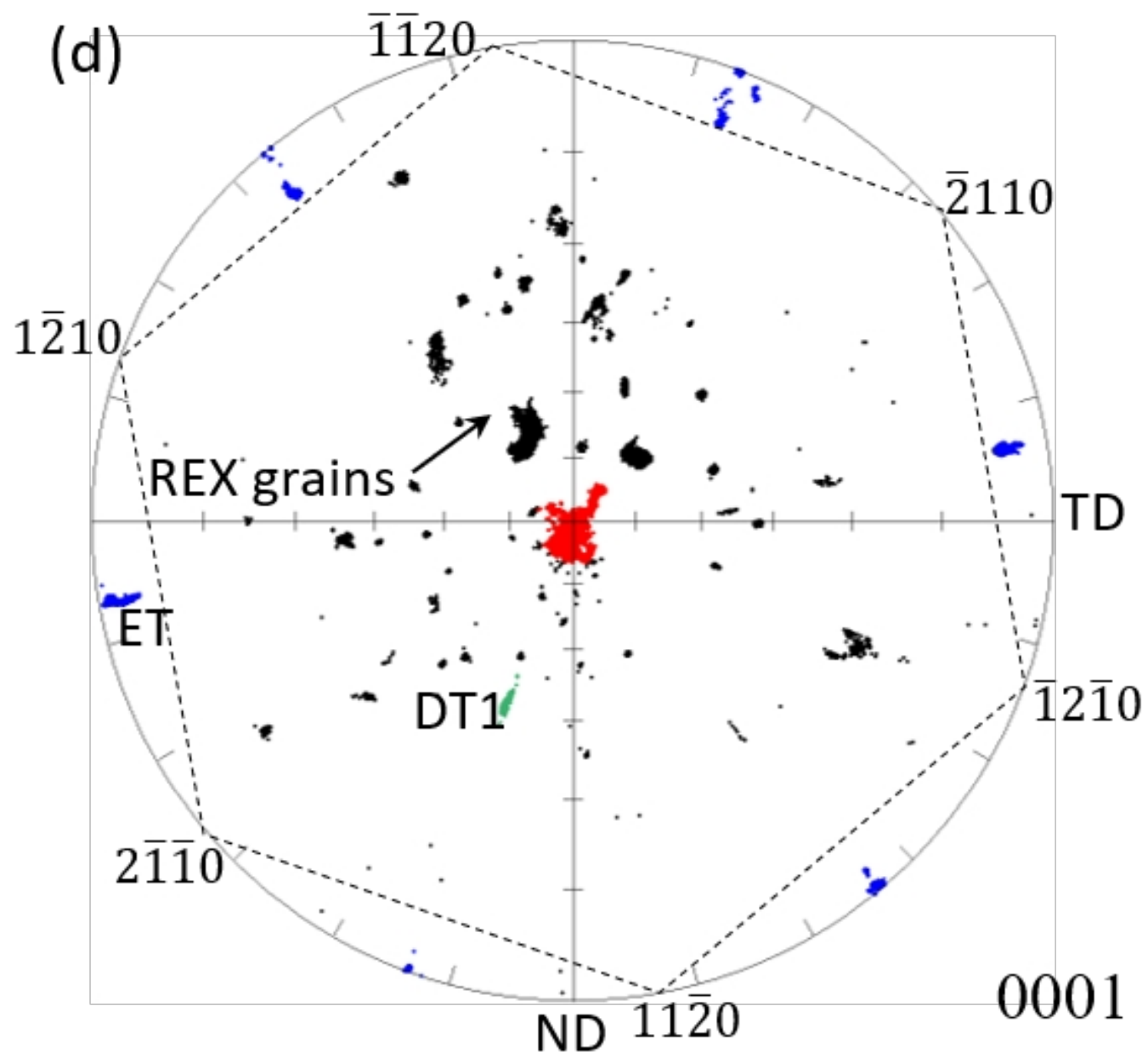


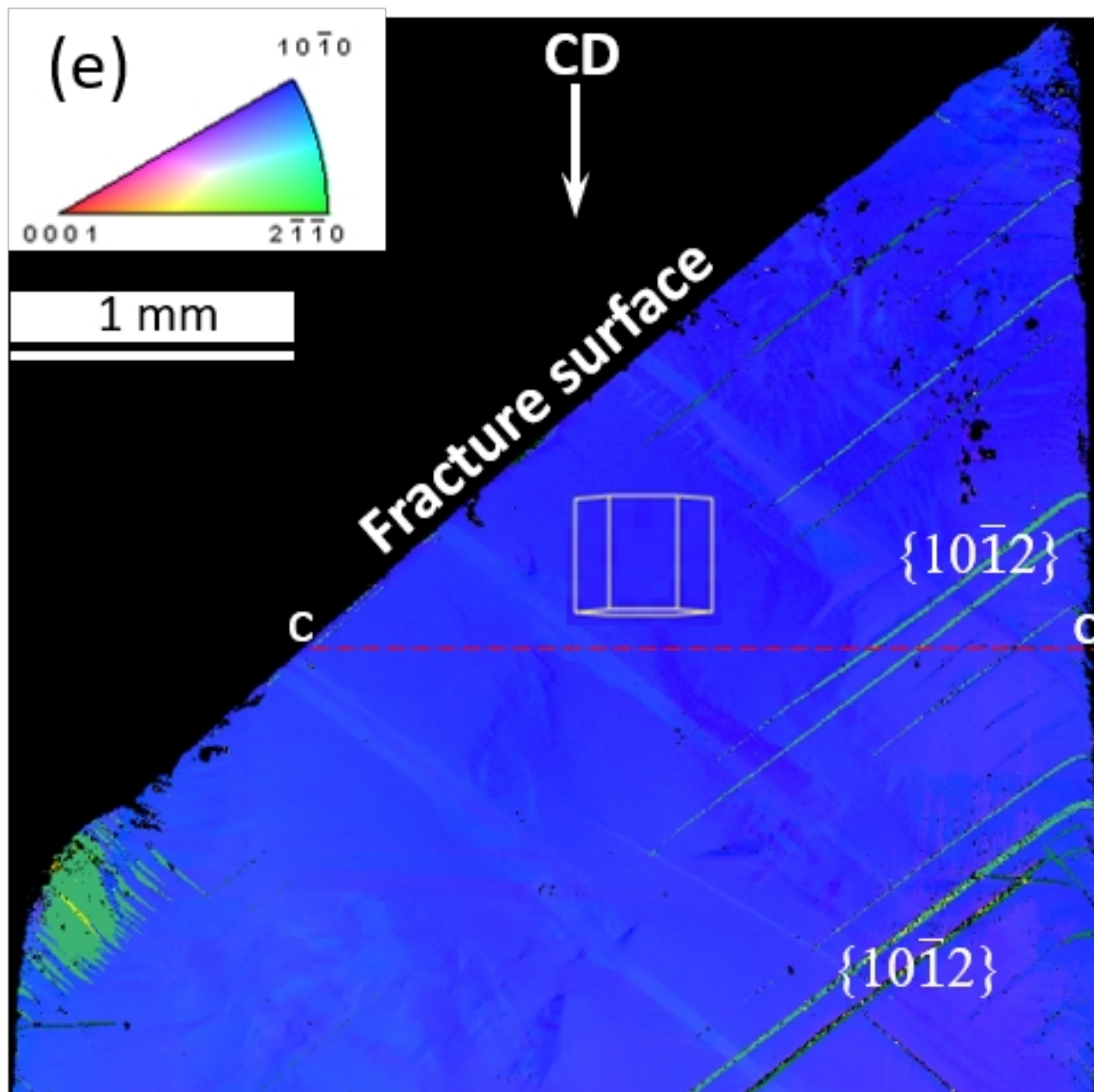


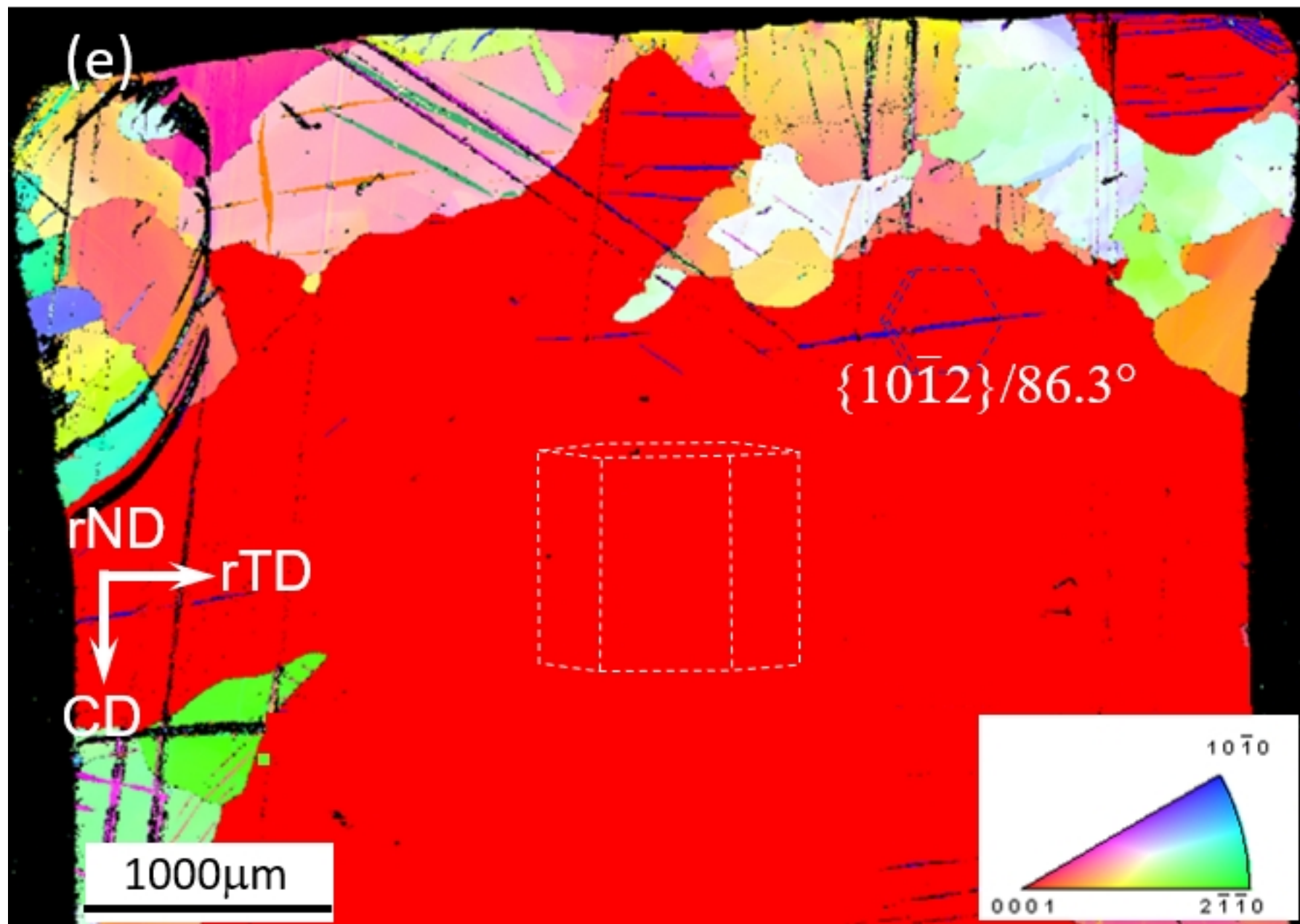


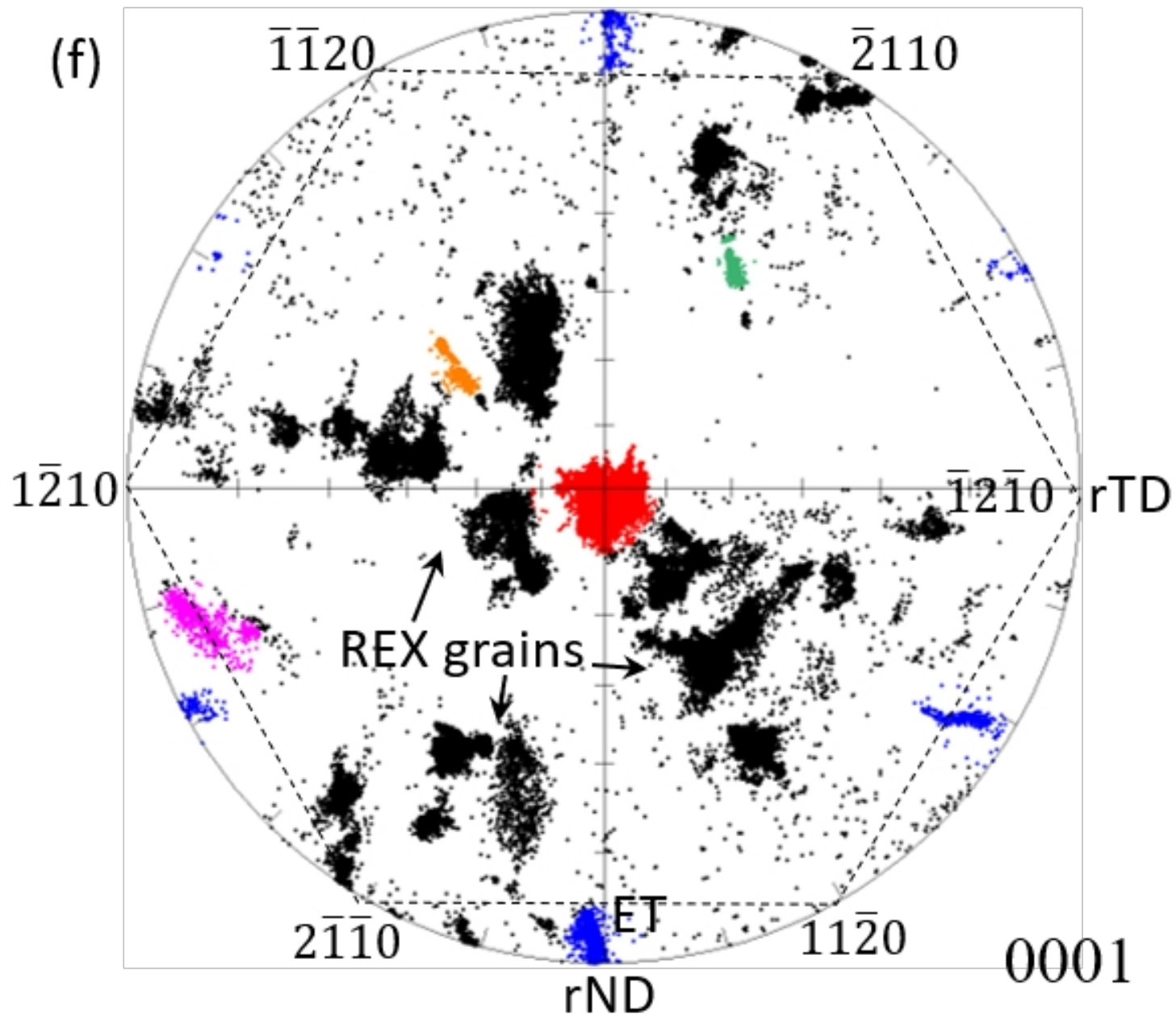




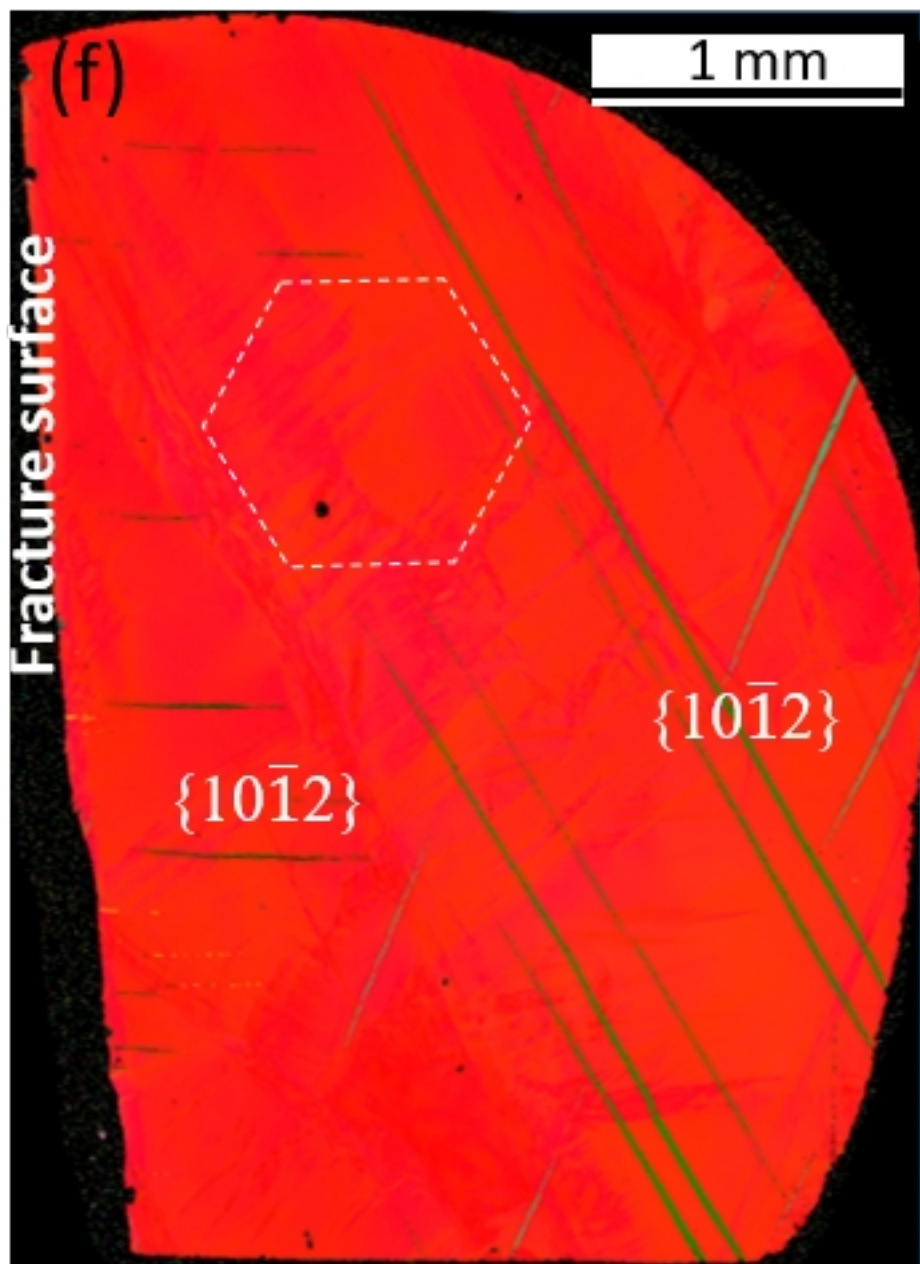






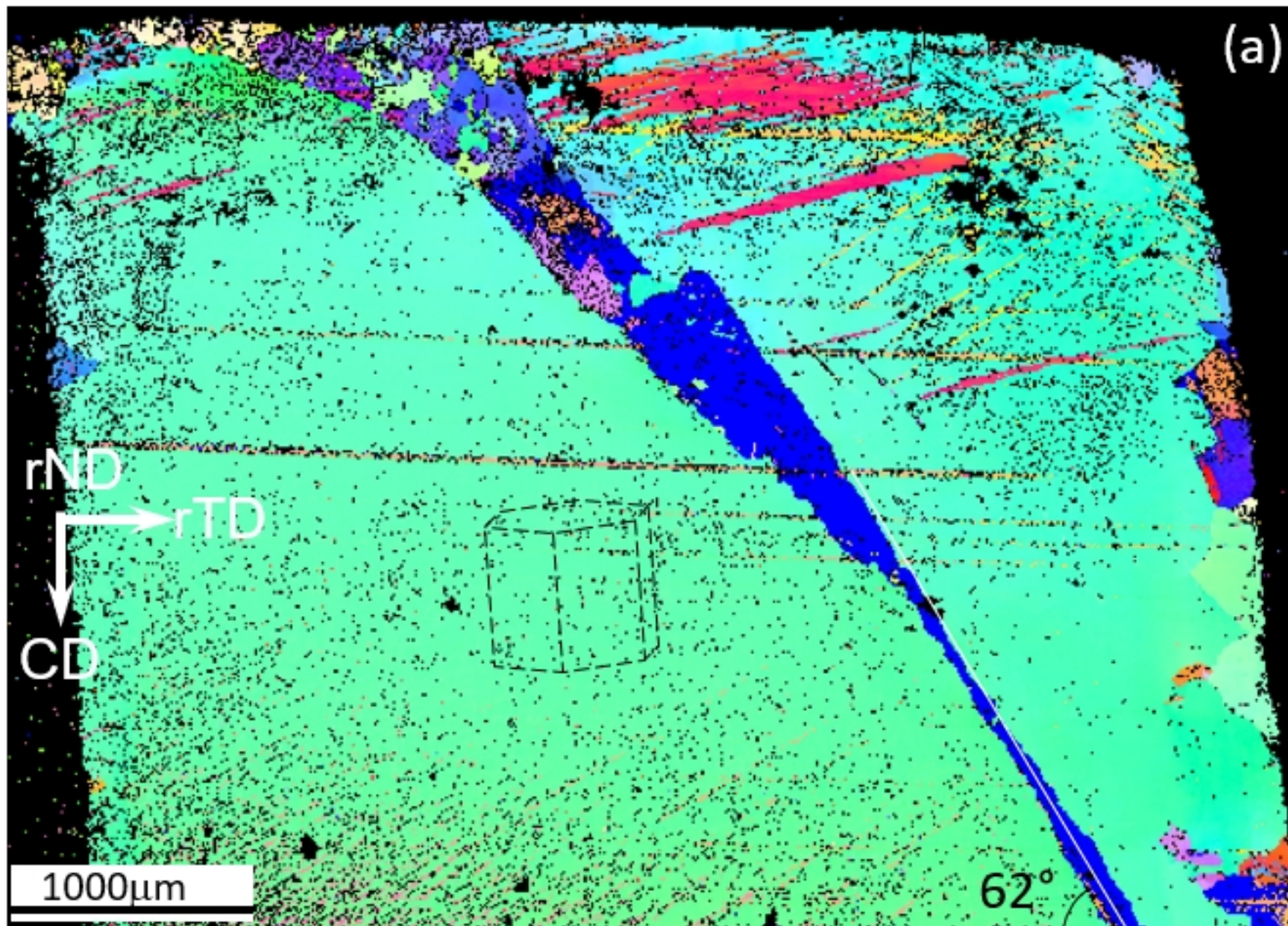








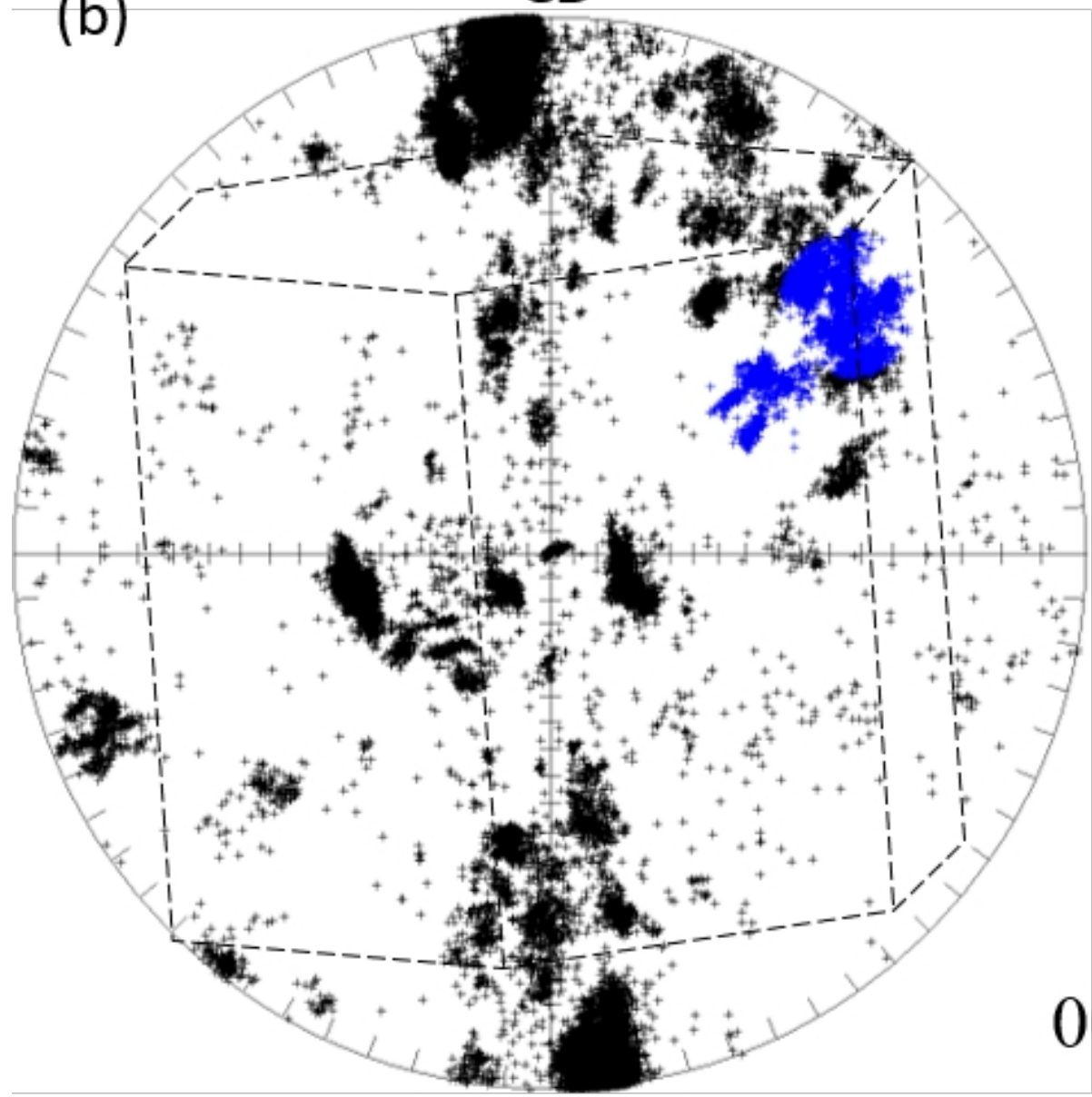






**CD**

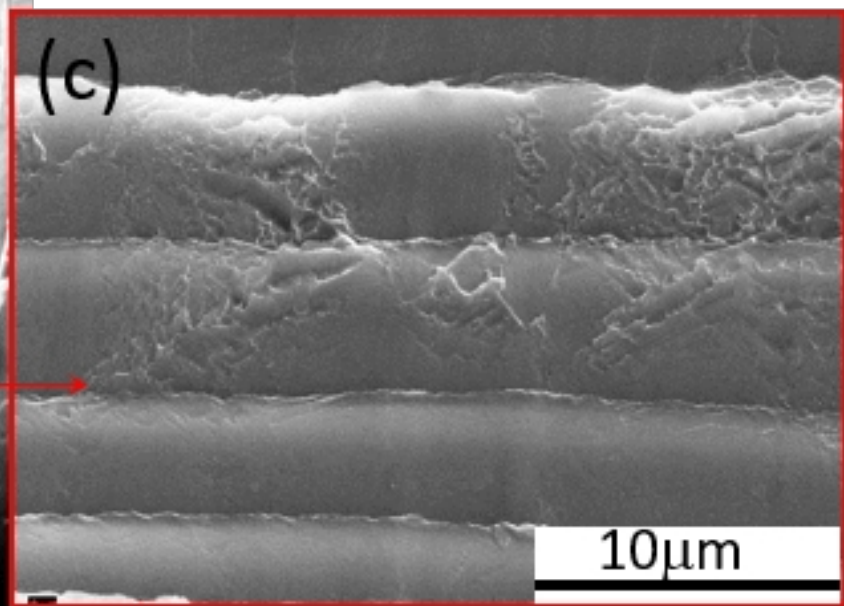
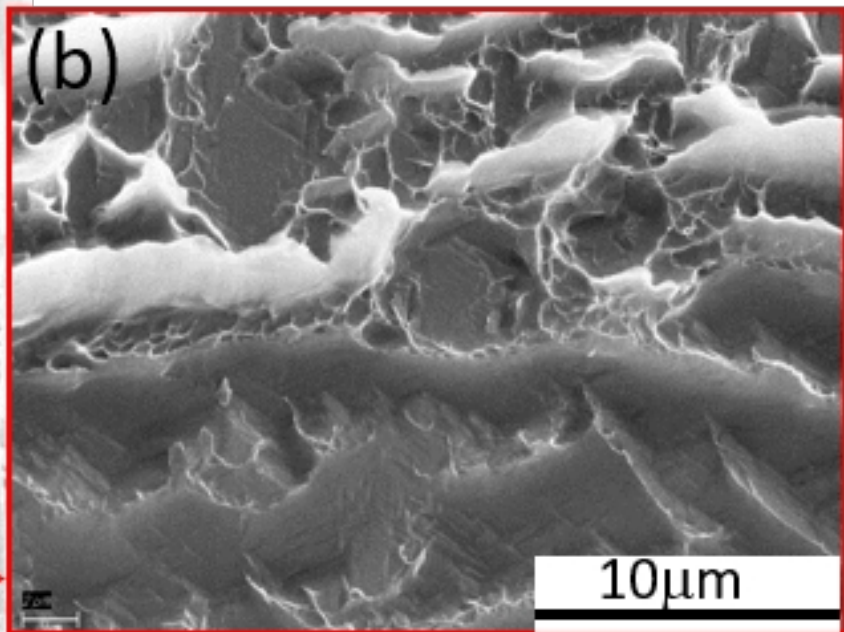
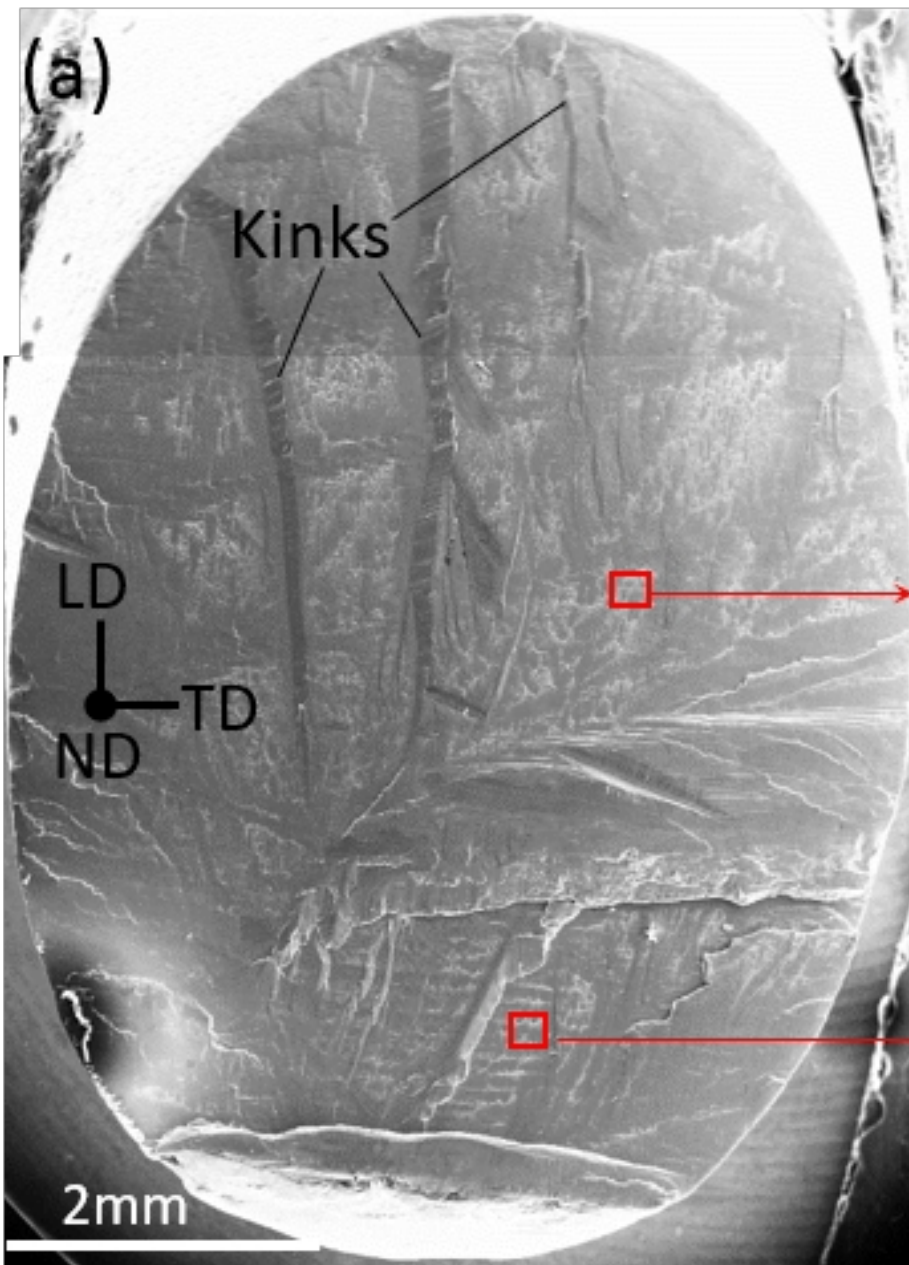
**(b)**

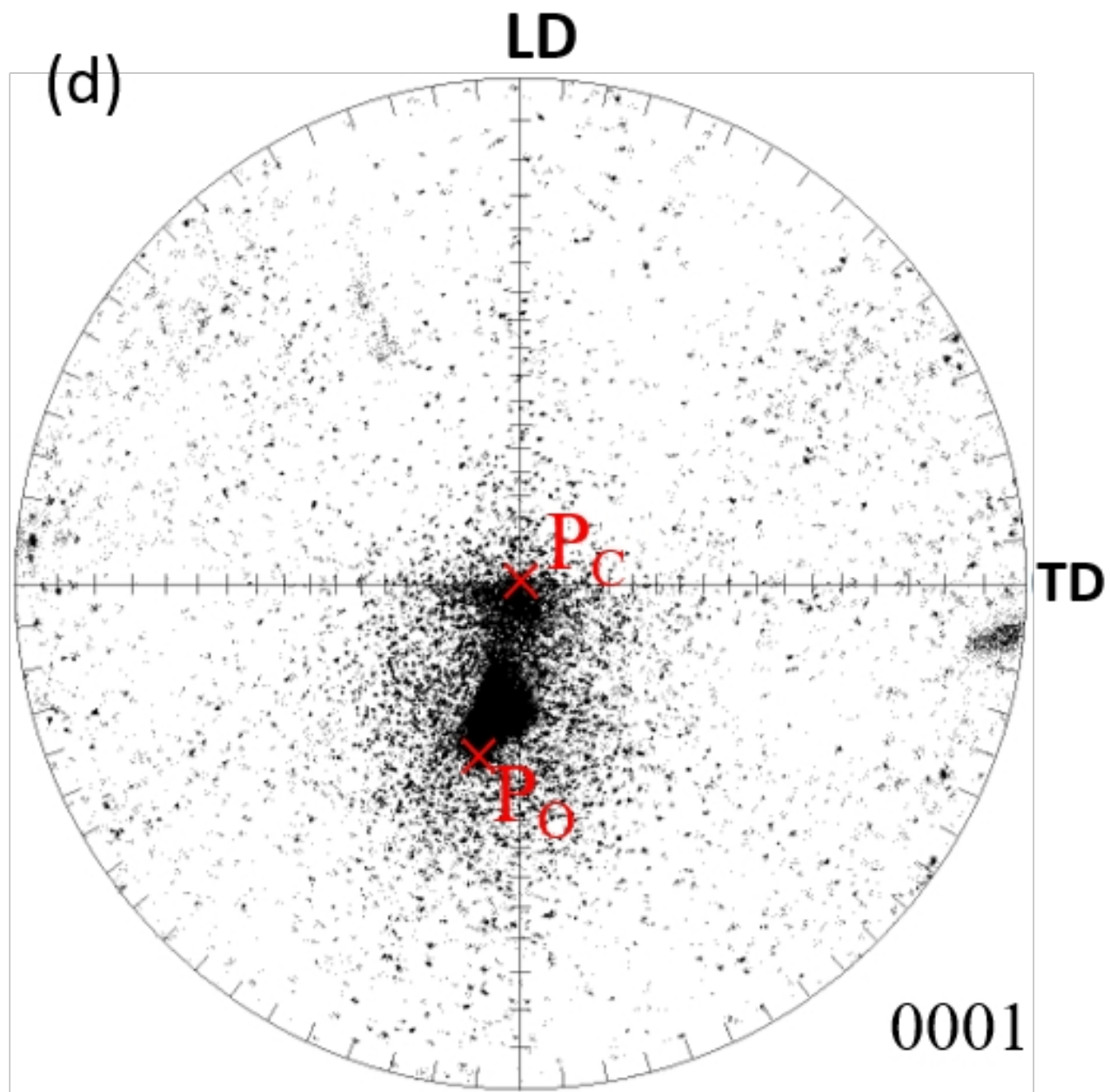


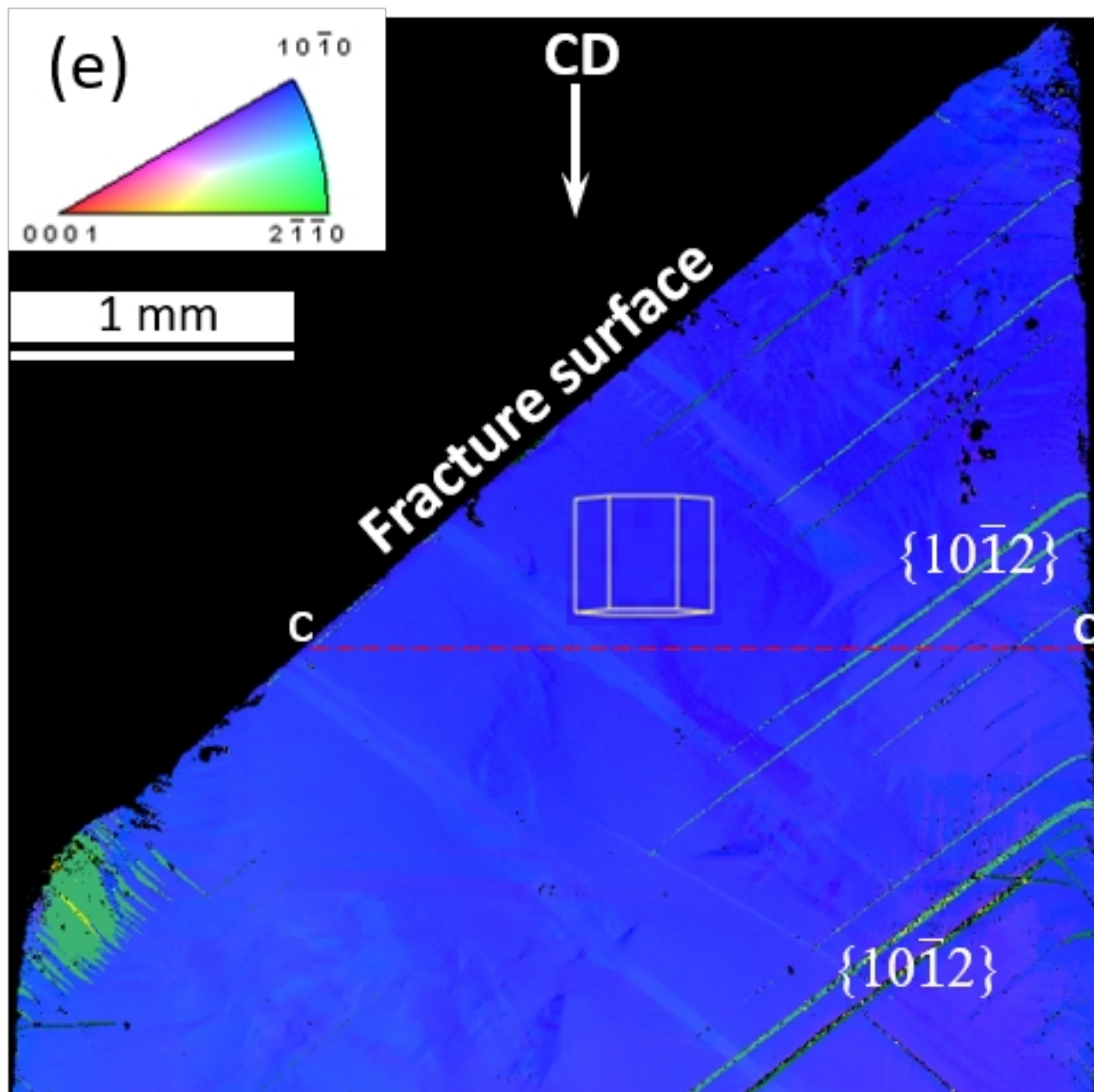
**rTD**

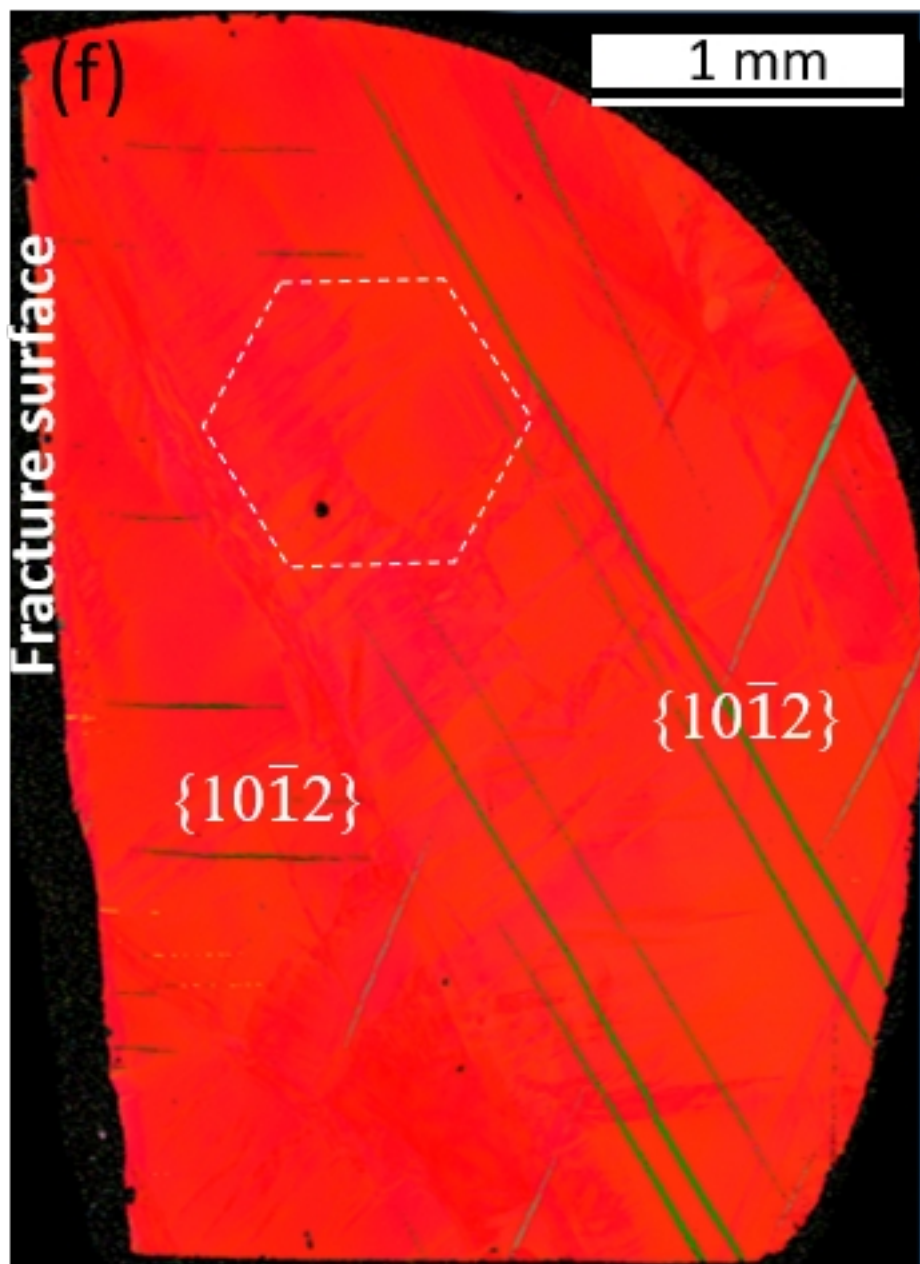
**0001**



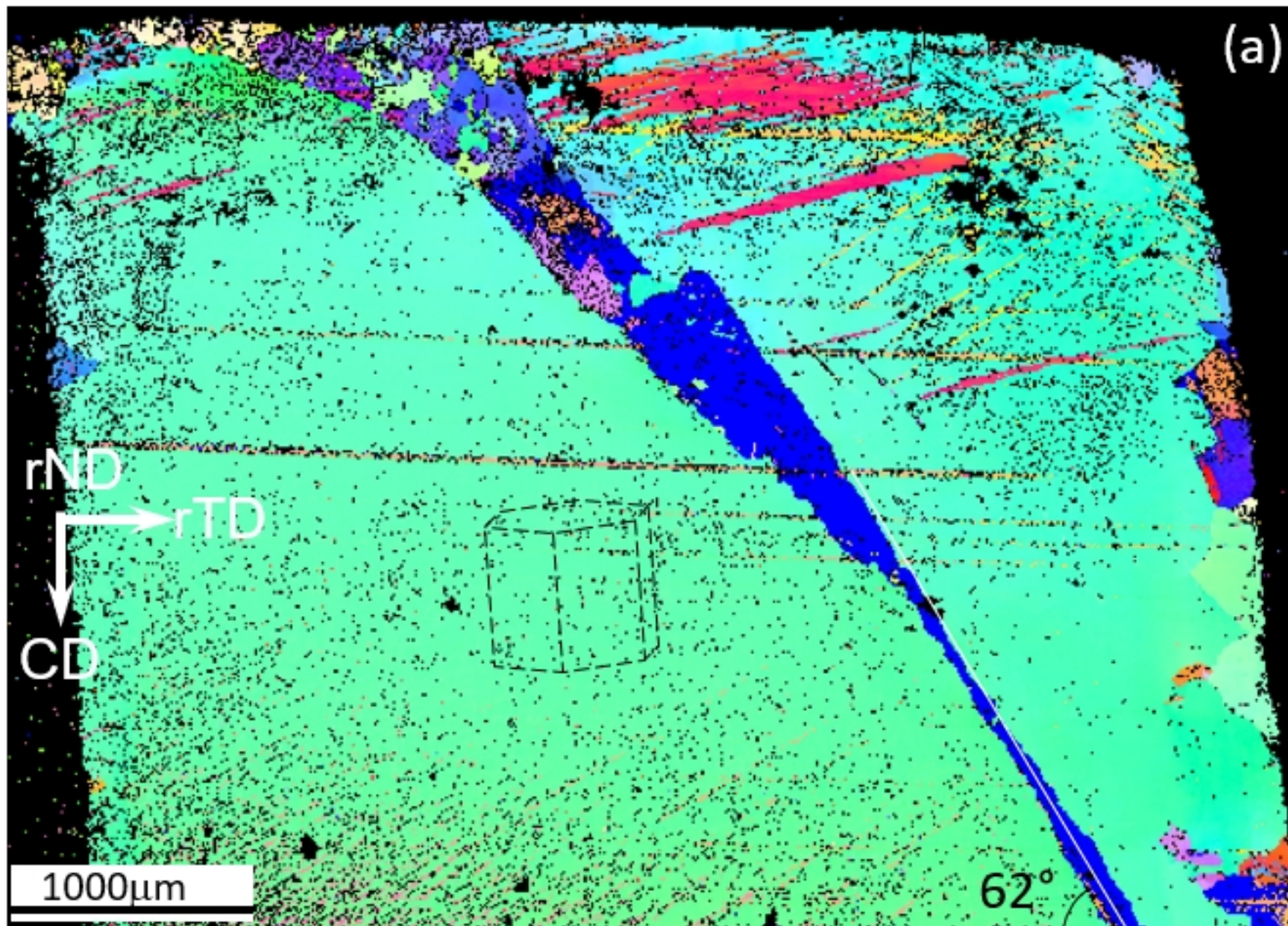








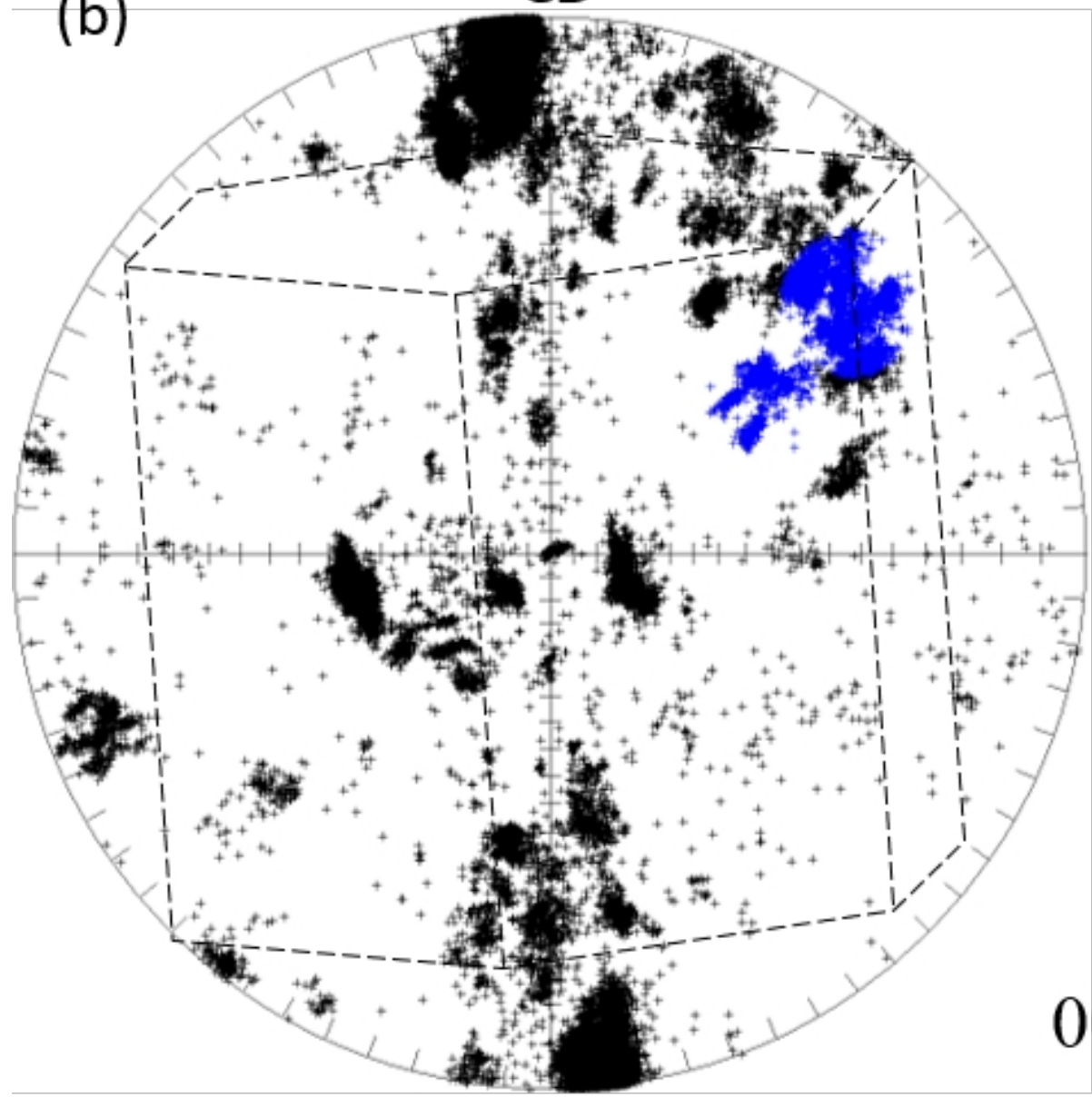






**CD**

**(b)**



**rTD**

**0001**

